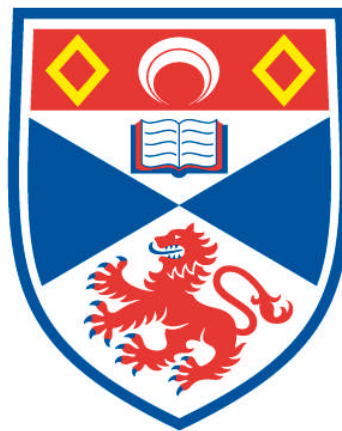


**ON GRAVITY:  
A STUDY OF ANALYTICAL AND COMPUTATIONAL APPROACHES  
TO PROBLEM SOLVING IN COLLISIONLESS SYSTEMS**

**Jeremy Andrew Barber**

**A Thesis Submitted for the Degree of PhD  
at the  
University of St Andrews**



**2014**

**Full metadata for this item is available in  
Research@StAndrews:FullText  
at:**

**<http://research-repository.st-andrews.ac.uk/>**

**Please use this identifier to cite or link to this item:**

**<http://hdl.handle.net/10023/6548>**

**This item is protected by original copyright**

**This item is licensed under a  
Creative Commons Licence**

# On Gravity

A study of analytical and computational approaches to problem solving in  
collisionless systems

*by*

**Jeremy Andrew Barber**

*No man should escape our universities without knowing how little he knows.*

*— J. Robert Oppenheimer*

*Submitted for the degree of Doctor of Philosophy in Astrophysics*

20<sup>th</sup> August 2014



University  
of  
St Andrews



# Declaration

I, Jeremy Andrew Barber, hereby certify that this thesis, which is approximately 42,000 words in length, has been written by me, and that it is the record of work carried out by me, or principally by myself in collaboration with others as acknowledged, and that it has not been submitted in any previous application for a higher degree.

Date

Signature of candidate

I was admitted as a research student in September 2010 and as a candidate for the degree of PhD in September 2010; the higher study of which this is a record was carried out in the University of St Andrews between 2010 and 2014.

Date

Signature of candidate

I hereby certify that the candidate has fulfilled the conditions of the Resolution and Regulations appropriate for the degree of PhD in the University of St Andrews and that the candidate is qualified to submit this thesis in application for that degree.

Date

Signature of supervisor



# Copyright Agreement

In submitting this thesis to the University of St Andrews we understand that we are giving permission for it to be made available for use in accordance with the regulations of the University Library for the time being in force, subject to any copyright vested in the work not being affected thereby. We also understand that the title and the abstract will be published, and that a copy of the work may be made and supplied to any bona fide library or research worker, that my thesis will be electronically accessible for personal or research use unless exempt by award of an embargo as requested below, and that the library has the right to migrate my thesis into new electronic forms as required to ensure continued access to the thesis. We have obtained any third-party copyright permissions that may be required in order to allow such access and migration, or have requested the appropriate embargo below.

The following is an agreed request by candidate and supervisor regarding the electronic publication of this thesis: Access to printed copy and electronic publication of thesis through the University of St Andrews.

Date

Signature of candidate

Date

Signature of supervisor



# Abstract

I present an overview of the tools and methods of gravitational dynamics motivated by a variety of dynamics problems. Particular focus will be given to the development of dynamic phase-space configurations as well as the and the distribution functions of collisionless systems.

Chapter 1 is a short review of the descriptions of a gravitational system examining Poisson's equations, the probability distribution of particles, and some of the most popular model groups before working through the challenges of introducing anisotropy into a model.

Chapter 2 covers the work of Barber & Zhao (2014) which looks at the relations between quantities in collisionless systems. Analytical methods are employed to describe a model that can violate the GDSAI, a well-known result connecting the density slope to the velocity anisotropy. We prove that this inequality cannot hold for non-separable systems and discuss the result in the context of stability theorems.

Chapter 3 discusses the background for theories of gravity beyond Newton and Einstein. It covers the 'dark sector' of modern astrophysics, motivates the development of MOND, and looks at some small examples of these MONDian theories in practice. Chapter 4 discusses how to perform detailed numerical simulations covering code methods for generating initial conditions and simulating them accurately in both Newtonian and MONDian approaches. The chapter ends with a quick look at the future of N-body codes.

Chapters 5 and 6 contain work from Barber et al. (2012) and Barber et al. (2014) which look at the recent discovery of an attractor in the phase-space of collisionless systems and present a variety of results to demonstrate the robustness of the feature. Attempts are then made to narrow down the necessary and sufficient conditions for the effect while possible mechanisms are discussed.

Finally, the epilogue is a short discussion on how best to communicate scientific ideas to others in a lecturing or small group setting. Particular focus is given to ideas of presentation and the relative importance of formality versus personality.



# Acknowledgements

I have a lot of people that I need to thank for their help and support over the last three-and-a-bit years.

First of all, special thanks to DD. Without you I'm not sure I'd have made it this far are at all. I owe a lot of this to you. Thank you.

Thanks to my good friends – you know who you are – for being there when I needed you the most. I owe you.

Thanks to my family for supporting me even when I didn't get to see them for a while.

Special thanks to Hongsheng. You have the patience of a saint and have taught me so much, especially in the final stretch. I hope you can be proud of the finished product.

Thanks go out to Steen for arranging all the visits and being such a lovely host. It has been a pleasure to work with you and I very much hope to do so again.

Thanks to Xufen for letting me pester her about codes and numerical work. Thanks also to Diana and Martin for their help when I was just starting out. It's been great to collaborate with you all.

Thanks to all my colleagues and friends in the department. I know I haven't been around so much lately, but it has been a pleasure to know you all. I wish you all the very best.

Thanks to STFC, St Andrews, and DARK. Without the funding from them I wouldn't be here in the first place.

And thanks to Thales and to all who came after for figuring out how to analyse the universe. It's an honour to help continue the journey.



# Contents

<b>Declaration</b>	<b>i</b>
<b>Copyright Agreement</b>	<b>iii</b>
<b>Abstract</b>	<b>v</b>
<b>Acknowledgements</b>	<b>vii</b>
<b>1 The foundations</b>	<b>1</b>
1.1 Potential density pairs in Newtonian gravity . . . . .	2
1.1.1 Solving Poisson’s equation for the Hernquist model . . . . .	4
1.2 Distribution Functions . . . . .	5
1.2.1 Deriving a DF with constant anisotropy . . . . .	8
1.2.2 Examining constant anisotropy models . . . . .	13
1.2.3 Osipkov-Merritt models and the Cuddeford generalisation . . . . .	16
1.2.4 Factors for DF positivity . . . . .	19
<b>2 The General Density-Slope Anisotropy Inequality in non-separable systems</b>	<b>23</b>
2.1 The inadequacy of a Jeans’ equation approach . . . . .	26
2.2 The Distribution Function approach . . . . .	31
2.2.1 Finding density . . . . .	32
2.2.2 Finding anisotropy . . . . .	33
2.2.3 Finding potential . . . . .	35
2.3 Understanding the system . . . . .	36
2.3.1 Characterising the density profile . . . . .	36
2.3.2 Characterising the anisotropy profile . . . . .	41
2.3.3 The inability to extend the GDSAI to this model . . . . .	42
2.4 System stability . . . . .	44

2.4.1	Radial Instability . . . . .	44
2.4.2	Hénon Instability . . . . .	44
2.4.3	Radial Orbit Instability . . . . .	46
2.4.4	Stability dependence on $L_{cut}^2$ . . . . .	47
2.5	Generalising the model . . . . .	50
2.6	Summary . . . . .	55
<b>3</b>	<b>The motivation for a new gravity</b>	<b>57</b>
3.1	Dark matter . . . . .	58
3.2	Dark energy . . . . .	59
3.3	Breakdowns of the current theory . . . . .	61
3.4	Modifications to Newtonian dynamics . . . . .	62
3.5	The difficulties of working in MOND . . . . .	64
3.6	Constructing MOND models . . . . .	69
3.6.1	Prolate spheroid densities . . . . .	70
3.6.2	Finding the velocity dispersion . . . . .	73
3.6.3	A simple model . . . . .	74
3.7	Relativistic approaches . . . . .	78
3.8	Working in conformal gravity . . . . .	79
<b>4</b>	<b>Numerical simulation</b>	<b>83</b>
4.1	Generating initial conditions . . . . .	84
4.2	GADGET-2: a Newtonian code . . . . .	86
4.2.1	Tree and TreePM force calculations . . . . .	87
4.2.2	Time-step determination . . . . .	89
4.3	NMODY: A MONDian code . . . . .	90
4.3.1	Force calculations and time-steps . . . . .	91
4.4	Hardware and next generation codes . . . . .	91
4.4.1	GRAPE . . . . .	91
4.4.2	CUDA . . . . .	92
4.4.3	Quantum processing . . . . .	95
<b>5</b>	<b>Attractors, radial orbits, and statistical side-effects</b>	<b>99</b>

5.1	Attractors in the Jeans' parameter space . . . . .	101
5.2	Initial conditions and numerical code . . . . .	103
5.2.1	Basic perturbation . . . . .	105
5.2.2	Analysis pipeline . . . . .	107
5.3	The basic results . . . . .	108
5.3.1	Effect of initial anisotropy profiles . . . . .	110
5.3.2	Effect of gravity theory . . . . .	113
5.3.3	Changing implicit coordinate system . . . . .	116
5.3.4	Random scale factors and flow time . . . . .	117
5.4	Impact of numerical resolution effects . . . . .	120
5.5	Condensing the method — bimodal perturbation . . . . .	124
5.6	Connection to radial orbit instability . . . . .	129
5.6.1	Universal anisotropy profiles . . . . .	129
5.6.2	Convergence of $\rho/\sigma^3$ . . . . .	131
5.6.3	$\beta - \gamma$ relation . . . . .	133
5.7	The story so far . . . . .	133
<b>6</b>	<b>Necessary and Sufficient Conditions</b>	<b>135</b>
6.1	Ruling out radial infall by adding energy . . . . .	137
6.1.1	Algorithm for avoiding infall . . . . .	138
6.2	The requirements for convergence . . . . .	140
6.2.1	Energy exchange — the anisotropy kick . . . . .	140
6.2.2	Energy exchange — the anisotropy contours . . . . .	145
6.2.3	Phase mixing in a fixed potential — the massless kick . . . . .	149
6.3	Impact of the attractor . . . . .	151
6.3.1	Density profiles . . . . .	154
6.3.2	Anisotropy profiles . . . . .	156
6.4	The path to convergence . . . . .	159
6.5	Summary . . . . .	160
<b>7</b>	<b>Epilogue – communication</b>	<b>163</b>
7.1	The power of analogy . . . . .	164
7.2	The need for confidence . . . . .	166

7.3 Informality versus accuracy . . . . .	168
<b>Online resources</b>	<b>169</b>
<b>Bibliography</b>	<b>171</b>

# List of Figures

1.1	DF of an anisotropic Plummer sphere . . . . .	13
1.2	Hernquist DFs for a set of anisotropies . . . . .	15
1.3	Comparison of anisotropy models . . . . .	18
1.4	Characteristic profiles of an anisotropic Plummer sphere . . . . .	20
2.1	Density of Jeans' model for GDSAI violation . . . . .	29
2.2	Demonstrating the negativity of the DF . . . . .	31
2.3	Numerical potential from our DF . . . . .	37
2.4	The components of the DF density profile . . . . .	38
2.5	The density profile of our DF . . . . .	39
2.6	Angular momentum of circular orbits in our DF . . . . .	40
2.7	Anisotropy profile of our DF . . . . .	41
2.8	Radial velocity profile of our DF . . . . .	43
2.9	Demonstrating GDSAI violation in our DF . . . . .	44
2.10	Hénon instability in our DF . . . . .	46
2.11	ROI as a function of angular momentum threshold . . . . .	47
2.12	GDSAI function of our system . . . . .	48
2.13	LOSVD through the centre of the system . . . . .	50
2.14	Energy functions in the generalised DF . . . . .	52
2.15	Density profiles of our generalised DF . . . . .	53
3.1	Iso-potential surfaces of a prolate system . . . . .	70
3.2	Iso-density contours for Newtonian and MOND gravity . . . . .	72
3.3	Iso-potential surfaces of a simple prolate system . . . . .	75
3.4	Iso-density contours for the simple Newtonian and MOND gravity . . . . .	76
3.5	Comparison between Newtonian and conformal gravity . . . . .	81

4.1	Schematic of the CUDA GPU architecture . . . . .	94
5.1	The form of the attractor . . . . .	103
5.2	3D projection of the density . . . . .	109
5.3	Basic attractor evolution in a model system . . . . .	111
5.4	Evolution in initially anisotropic systems . . . . .	112
5.5	Evolution in extreme anisotropy initial conditions . . . . .	112
5.6	Acceleration profile showing gravitational regimes . . . . .	113
5.7	Evolution in weak MOND in an isotropic system . . . . .	114
5.8	Evolution in weak MOND in a radially anisotropic system . . . . .	114
5.9	Evolution in deep MOND . . . . .	115
5.10	The collapse of deep MOND models . . . . .	116
5.11	Average anisotropy contours in a stable, unperturbed system . . . . .	118
5.12	Anisotropy contours in a perturbed system . . . . .	119
5.13	Demonstrating factors effecting convergence rate . . . . .	120
5.14	Attractor plot demonstrating negligible two-body interaction . . . . .	123
5.15	Demonstration of the possible statistical roots of the attractor . . . . .	126
5.16	Artificial distortion of the attractor through poor algorithm choice . . . . .	128
5.17	Anisotropy profiles of all models . . . . .	130
5.18	Phase-space density profiles of all models . . . . .	132
6.1	Attractor plot demonstrating no radial infall . . . . .	140
6.2	Schematic of the anisotropy kick . . . . .	142
6.3	Contour plot of an isotropising kick with kick artifacts included . . . . .	146
6.4	Attractor plot of the same information as Fig. 6.3 . . . . .	146
6.5	Contour plot of a stronger isotropising kick . . . . .	148
6.6	Contour plot demonstrating a tangentially orientated kick . . . . .	148
6.7	Attractor plot of the massless kick . . . . .	150
6.8	Virial ratio at the end of the flow periods . . . . .	151
6.9	Kinetic energy contours for the isotropic system . . . . .	153
6.10	Demonstrating the development of a dense nucleus and large radius envelope	155
6.11	Final density profiles compared to standard profiles . . . . .	155
6.12	Anisotropy profiles during perturbation . . . . .	156

6.13 Anisotropy profile of a radially anisotropic system during perturbation . . .	158
6.14 Time evolution of a single bin in phase space . . . . .	160
6.15 The attractor represented as a vector field in the system phase space . . . .	161



# 1

## The foundations

*“Gravity is a habit that is hard to shake off.”*

— *Terry Pratchett, Small Gods*

It is often noted in popular physics that, among the fundamental forces in our universe, gravity stands out as rather strange. Most obvious, perhaps, is its apparent weakness compared to its fellows — a toy bar magnet can exert a force on, say, a paper-clip that is many orders of magnitude more significant than the gravitational attraction of the entire Earth. So while it is perhaps unfair to single out differences between the forces – clearly differences *must* exist otherwise the forces wouldn’t be distinct from each other – the fact that gravity is a good  $10^{30}$  weaker than the other forces bears comment. It should be noted that there is nothing ‘clear’ about how the forces are distinct from each other or, indeed, if they even are. However that is a whole other story that will not be told in this thesis.

So, given gravity’s rather anaemic pull on matter it might be wondered, then, how gravity manages to accomplish much of anything, let alone build planets or stars. The

answer is what makes gravity so important. There is no such thing as negative mass. Electrostatic forces may be born of positive or negative charge, magnets, at least generally, have a north and a south pole, but there is no such thing as negative mass.

Why this is is a matter of debate. Nothing in fundamental physics explicitly forbids negative mass, although the properties of such material are rather counter-intuitive (Bondi, 1957). All that matters for our purposes is that the more matter that there is, the more gravity becomes dominant. And so it is that, at galactic scales and beyond, the dynamical behaviour and structure of the universe is governed almost exclusively by gravitational interactions, the other forces cancelling themselves, lacking the range of transmission, or being too specific in what they affect. Consequently, if you want to understand and describe how anything is born, moves, evolves, and, eventually, is destroyed, gravity is foundation of everything that you need to know.

However, this is easier said than done. Gravity can be surprisingly complex, often confusing, and sometimes completely intractable. Therefore it is vital to have an understanding of the wide variety of approaches, methods, and tools that astrophysicists have developed to solve any system that nature can conjure up (including a few that it can't, but are interesting anyway). On that note, let us start at the beginning and look at how gravitational fields are born.

## 1.1 Potential density pairs in Newtonian gravity

At its heart, a theory of gravity describes the coupling between a distribution of matter and an accompanying potential field. If one knows what the distribution of matter in a system is, then the theory can be applied to predict how the matter in the system will move. The limits on these predictions vary depending on the specifics of the theory, but examples in Newtonian gravity include the unpredictable evolution of systems containing more than two objects of similar mass and the degeneracy of predicted densities that can produce a given potential (Binney & Tremaine, 2008). Newtonian gravity is the most familiar paradigm alongside its adaption into Einstein's general relativity and between them these theories have an imposing list of successes, ranging from predictions of gravitational lensing to the successful launching of probes to the outer solar system.

Newtonian gravity can be summed up by a single, simple relationship; Poisson's equa-

tion:

$$\nabla^2\Phi = 4\pi G\rho \tag{1.1}$$

In brief, this relationship is a rather neat representation of a collection ideas. A distribution of matter  $\rho$  in some enclosed volume produces a vector field, a force  $\mathbf{g}$ , which can be described as the gradient of a potential  $\Phi$ . The fact that you can construct one-to-one pairings between the potentials and the densities that created them, a level of degeneracy aside, gives rise to the description of ‘potential-density pairs’. As powerful and as simple as Poisson’s equation can be when dealing with complex potentials or densities it can be difficult and time consuming to find a new solution for an unknown part of a potential density pair. Additionally, there are certain forms of system that appear far more frequently in nature than others, such as spheres, and having a set of well understood, generalised potential-density pairs speeds up many areas of analysis.

This motivates a need for densities that translate easily and tractably to potentials and vice versa but that are still accurate descriptions of physically interesting systems. One of the earliest families used were the polytropic models (Lane, 1870). These models were developed to describe the structure of hydrostatic, pressure supported spheres of gas and subsequently found use in the study of stellar interiors before the advent of complex hydrodynamic simulations. These models are a general prescription parameterised as:

$$\frac{1}{s^2} \frac{d}{ds} \left( s^2 \frac{d\psi}{ds} \right) = -3\psi^n; \psi > 0 \tag{1.2}$$

where  $s$  and  $\psi$  are the dimensionless radius and positive potential. Also, much like the Dehnen models we will encounter momentarily, these are important due to their well understood potential density pairs and relation to physical systems. One model which has found extensive use in the field of galactic modeling, and will be appearing frequently throughout the following chapters, is the  $n = 5$  polytrope, or Plummer Sphere (Plummer, 1911).

Today, many of the most commonly useful density models are drawn from a family of models called ‘two-power’ models after their characteristic profile of an inner power law and an outer power law. They are parameterised as follows:

$$\rho(r) = \frac{\rho_0}{\left(\frac{r}{a}\right)^\alpha \left(1 + \frac{r}{a}\right)^{\beta-\alpha}} \quad (1.3)$$

Models drawn from this family thus have two free parameters besides the slope of the power laws, a critical density,  $\rho_0$ , and a scale length,  $a$ . Generically they are known as ‘two-power density laws’ but the subgroup where  $\beta = 4$ , the aforementioned Dehnen models (Dehnen, 1993), contain several widely used models of interest most notably the Hernquist (Hernquist, 1990) and Jaffe (Jaffe, 1983) models having  $\alpha = 1$  and  $\alpha = 2$  respectively. To demonstrate the simple connection between the density and potential in these models we now solve Poisson’s equation for the Hernquist model.

### 1.1.1 Solving Poisson’s equation for the Hernquist model

Solving a potential to find a density involves differentiation which, in almost all cases, is an easier proposition than integration. Accordingly, we’ll do the reverse and find the potential from the density.

The Hernquist model density profile is:

$$\rho(r) = \frac{M a}{2\pi r} \frac{1}{(r + a)^3} \quad (1.4)$$

where  $a$  represents a characteristic length scale of the system and  $M$  is the total mass of the system. We can find the potential by first turning the density distribution into a cumulative mass distribution. Since the volume is spherical:

$$M(r) = \int_0^{2\pi} \int_{-\frac{\pi}{2}}^{\frac{\pi}{2}} \int_0^r \frac{M a}{2\pi r} \frac{1}{(r + a)^3} r^2 \sin \theta \, dr \, d\theta \, d\phi = \left[ \frac{-ar}{(r + a)^2} \right]_0^r - \left[ \frac{-a}{(r + a)} \right]_0^r \quad (1.5)$$

Notice that the equations produce infinities at  $r=0$ . This can be solved by recognising that:

$$\int_0^r = \int_0^\infty - \int_r^\infty \quad \text{and} \quad M = \int_V \rho(r) dV = 4\pi \int_0^\infty \rho(r) r^2 dr \quad (1.6)$$

This means we can re-write Eq. 1.5 in terms of the total mass and the new limits:

$$M(r) = M - \left[ \frac{-ar}{(r+a)^2} \right]_r^\infty - \left[ \frac{-a}{(r+a)} \right]_r^\infty = \frac{Mr^2}{(r+a)^2} \quad (1.7)$$

From here, we can simply use the fact that  $F = \nabla\Phi$  and thus integrate with respect to  $r$  to find the potential:

$$\Phi = \int_r^\infty \frac{-GM}{(r+a)^2} dr = \left[ \frac{GM}{r+a} \right]_r^\infty = \frac{-GM}{r+a} \quad (1.8)$$

As useful as this is it does not contain any information on particle movements beyond the general form of the potential. In general, dealing only with potential density pairs makes it difficult to assess the dynamical properties of the system. What we would prefer is a description of the system which contains information not only on particle positions, but also contains the distribution of energy and angular momenta. To be exact, we would like a function that describes the distribution of particles in phase-space; a ‘Distribution Function’, so to speak.

## 1.2 Distribution Functions

The distribution function (DF) is a representation of a system in a six-dimensional position-velocity phase space. At a given time the DF describes the probability of finding particles with three-dimensional position  $\mathbf{x}$  and three-dimensional velocity  $\mathbf{v}$ .

In order to understand the next chapter properly it is necessary to develop some of the tools associated with the assessment of a DF. Most quantities derived from the DF are found through integration and frequently require special solutions and inversions to be analytically soluble. In order to explain them, and also to motivate the next chapter, we will embark on a worked example of the use of a DF.

It should be noted, however, that while the DF is an incredibly simple and powerful description of a system it generally does not do the job of relating potential to density. The DF is just a distribution of energies and does not encode the coupling of gravitational force like the Poisson equation does.

We can start by defining a useful quantity which describes the probability per unit volume of finding a star at a given position but without caring what velocity it has:

$$\nu(\mathbf{x}) = \int f(\mathbf{x}, \mathbf{v}) d^3\mathbf{v} \quad (1.9)$$

where  $f(\mathbf{x}, \mathbf{v})$  is our DF. We can relate this to the real-space number density by multiplying by the number of stars in the system,  $N$ :

$$n(\mathbf{x}) = N\nu(\mathbf{x}) \quad (1.10)$$

This kind of description is particularly useful when considering how to construct numerical models as it provides a natural link between the smooth density and the number of particles used in a simulation. The DF can also immediately tell us the probability distribution of velocities at a given position:

$$P_{\mathbf{x}}(\mathbf{v}) = \frac{f(\mathbf{x}, \mathbf{v})}{\nu(\mathbf{x})} \quad (1.11)$$

where  $P_{\mathbf{x}}(\mathbf{v})$  is the probability distribution of velocities at the point  $\mathbf{x}$  and can be expressed as the probability of finding a star at  $\mathbf{x}$  with specific velocity  $\mathbf{v}$  over the probability of finding a star at  $\mathbf{x}$  with *any* velocity.

The velocity dispersion is characterised by both the changes in the mean velocity from point to point and also the local spread of velocities around the mean at those points so we need to find a way to describe those quantities. The mean velocity can be found by the standard formula for expectation values:

$$\bar{\mathbf{v}}(\mathbf{x}) = \int \mathbf{v} P_{\mathbf{x}}(\mathbf{v}) d^3\mathbf{v} \quad (1.12)$$

Using the expression in Eq. 1.11 we can write the mean velocity as:

$$\bar{\mathbf{v}}(\mathbf{x}) = \frac{1}{\nu(\mathbf{x})} \int \mathbf{v} f(\mathbf{x}, \mathbf{v}) d^3\mathbf{v} \quad (1.13)$$

Our velocity dispersion measure now has a description of the changes in mean velocity from point to point so now we just modify it so that the spread of velocities (the variance of  $\mathbf{v}$ ) is being used rather than specific values. This leads us to the velocity dispersion tensor:

$$\sigma^2 \equiv \frac{1}{\nu(\mathbf{x})} \int (\mathbf{v} - \bar{\mathbf{v}})^2 f(\mathbf{x}, \mathbf{v}) d^3\mathbf{v} \quad (1.14)$$

This is an analogue of the statistical measure of variance and can be expressed in a more familiar way:

$$\sigma^2 = \overline{v^2} - \bar{v}^2 \quad (1.15)$$

Notice that the dispersion is governed entirely by the form of the DF. This also allows us to define a very useful quantity which describes the ratio of energy contained within the various axes which is the velocity anisotropy parameter:

$$\beta = 1 - \frac{\sigma_\theta^2 + \sigma_\phi^2}{2\sigma_r^2} \quad (1.16)$$

In an isotropic system  $\beta = 0$  while a completely radial system gives  $\beta = 1$ . A completely circular system gives the rather strange behaviour  $\beta \rightarrow -\infty$ . The isotropic case is particularly important because of how it relates to the angular momentum behaviour of the DF.

If the distribution of particles in the system is governed only by energy then the Hamiltonian  $H = K+V$  completely describes the motion. Accordingly we can make the substitution that  $f(\mathbf{x}, \mathbf{v}) = v^2/2 + \Phi$  in Eq. 1.13 and describe a general mean velocity.

Since this expression is a function only of  $v^2$  it is implicit that equipartition of energy will be what dictates how energy is split between the different axes. This means that the energy will be spread evenly across all velocity components and thus all of the velocity dispersions will be the same. In other words *if a system has a DF that is a function only of energy then it is necessarily isotropic.*

It is easy to see why we can say that the dispersions will be equal rather than just the mean velocities. The integral of Eq. 1.13 is over all possible velocities but  $\mathbf{v}$  is odd while  $H$  is even. This implies that the overall integral is odd and will evaluate to 0. Consequently,  $\bar{v} \cdot \bar{v} = 0$  so Eq. 1.15 simplifies to  $\sigma^2 = \overline{v^2}$ . In other words, in this scenario the velocity dispersion and the mean squared velocity are equivalent.

Having covered some of the basics of the DF we can now try to use it to examine the properties of a system we are interested in.

### 1.2.1 Deriving a DF with constant anisotropy

The Plummer sphere Plummer (1911) is one of the more popular models in dynamics despite not being the most realistic thanks primarily to its considerable simplicity. Even in this thesis Plummer spheres comprise the majority of simulations in the latter chapters simply because of how easy they are to create with a desired anisotropy profile. Here and now, however, we use them because we desire a simple example to illustrate two things: how a DF can be used to create a complete system, and to show that  $\beta$  is not independent of density.

We will begin with a model whose anisotropy is not a function of radius. DFs of such systems have a simple enough parameterisation (Binney & Tremaine, 2008):

$$f(\mathcal{E}, L) = L^{-2\beta} f(\mathcal{E}) \quad (1.17)$$

where  $L$  is the angular momentum distribution.

Notice that our DF is in terms of different but equivalent variables. In practice it is not always optimal to construct a DF in terms of velocities as energies and momenta are more fundamental descriptions. We define the relevant energies as follows:

$$\mathcal{E} = - \left( \frac{1}{2} v^2 + \Phi \right) + \Phi_0 = \Psi - \frac{1}{2} v^2 \quad (1.18)$$

where  $\Phi_0$  is some constant potential and  $\Psi$  is the relative potential *i.e.* the positive equivalent of the potential  $\Phi$ .

So, we begin by finding the density of our model. Now obviously we know what this should be because it is a well known result, but actually reproducing it is not as simple as it might seem. Since we already know that the Plummer sphere is just the  $n=5$  polytrope we can save a little time and use the DF that we know leads to Plummer models. If we try to simply solve Eq. 1.9 directly we end up with:

$$\rho = C \int \frac{\mathcal{E}^{\frac{7}{2}}}{L^{2\beta}} \frac{\pi}{r^2} \left( \frac{L^2}{r^2} + \mathcal{E} - \Psi \right)^{-1} dL^2 d(-\mathcal{E}) \quad (1.19)$$

which is not conducive to analytic results. The much better way to solve this system is by posing the question in terms of specialised coordinates. The coordinates we choose are best at describing velocity vectors in a spherical polar system and are constructed thus:

$$v_r = v \cos \eta; v_\theta = v \sin \eta \cos \chi; v_\phi = v \sin \eta \sin \chi \quad (1.20)$$

The geometry of  $\eta$  and  $\chi$  is apparent from the consideration that for  $\eta = 0$ ,  $v_r = v$ .  $\eta$  is the angular difference between the velocity vector and the radial axis. Similarly,  $\chi$  is the angle made by the velocity vector and a circumferential ring. Using this description we can express Eq. 1.9 as:

$$\nu = \int f(\mathcal{E}, L^2) d^3\mathbf{v} = 2\pi \int_0^\pi \sin \eta d\eta \int_0^{\sqrt{2\psi}} v^2 f\left(\psi - \frac{1}{2}v^2, rv \sin \eta\right) dv \quad (1.21)$$

where we applied the standard spherical volume element to arrive at this. This expression is simple enough to integrate without further simplification to yield a general solution:

$$\nu = \frac{2^{-(\beta+7/2)} C \psi^{5-\beta} \Gamma\left[\frac{3}{2} - \beta\right]}{r^{2\beta} \Gamma[6 - \beta]} \quad (1.22)$$

$$C = 210\pi^2 \frac{(-\beta)!}{\left(\frac{1}{2} - \beta\right)!} \quad (1.23)$$

where the gamma function is defined as (Hazewinkel, 1994):

$$\Gamma[t] = \int_0^\infty x^{t-1} e^{-x} dx \quad (1.24)$$

This is a rather nasty equation but for this example we do not particularly care about the full range of its behaviour. Remember that we are just trying to find the density profile of our anisotropic Plummer sphere so we can just take a value for  $\beta$  which simplifies the system. The simplest system is obviously the isotropic case but as that is not terribly

interesting we examine the case of  $\beta = 1/2$  instead which yields:

$$\nu = \frac{D\psi^{9/2}}{r} \quad (1.25)$$

where  $D$  is some constant. We need to be able to solve the Poisson equation now which, upon substitution, takes the form:

$$\frac{1}{r^2} \frac{d}{dr} \left( r^2 \frac{d\psi}{dr} \right) + 4\pi G \frac{D}{r} \psi^{9/2} = 0 \quad (1.26)$$

If you think back to start of the chapter we talked briefly about how polytropes are derived from the Lane-Emden equation (LE) of Eq. 1.2. As you can perhaps see, Eq. 1.2 can be derived directly from Eq. 1.26 with only some small assumptions about the equations of state were it not for one problem.

The problem is that in this version there is an extra factor of  $r$  that is not normally present. Explicitly, if we had solved for an isotropic system rather than an anisotropic one then we would have arrived at the standard Plummer result:

$$\nu = F\psi^5 \quad (1.27)$$

which leads to the LE and is one of the rare analytical solutions to it given that  $F$  is just some constant

All of this highlights the essential problem with gravitational systems and why we place so much emphasis on potential-density pairs. It is extremely rare to find a system where everything is simple. You can start from a simple DF but be left with a non-analytic density or you can start from a simple potential-density pair but the DF is extremely complex. The isotropic Plummer model is one of the simplest models around but even that rapidly becomes obstructively complex when applying a basic anisotropy law.

The reason for the complexity is this. The anisotropy cannot be directly accounted for in the density profile or potential *i.e.* if presented with a standard Plummer density profile there is no way to tell what anisotropy behaviour it has without needing additional information. Because of this, the anisotropy is best introduced at the level of the DF as it is more naturally associated with the distribution of energies in the system.

However, as we have just seen, if we introduce anisotropy at the DF level we will not recover the same density profile as an isotropic DF would have done. This is because by changing the anisotropy at a given radius the available phase-space is smaller and thus the real-space density is also lower.

So, this leaves us in a quandary. If we want to build an anisotropic, analytic model we must start from the DF but then still guarantee the form of the resulting density. One of the better ways to try and arrive at an analytical solution for a general system is to perform an inversion.

If we go back to our general solution for the constant anisotropy model in Eq. 1.21 we can choose not to specify the DF we were using to instead arrive at:

$$\frac{(\frac{1}{2} - \beta)!}{\sqrt{\pi}(-\beta)!} \frac{2^{\beta-1/2}}{2\pi} r^{2\beta} \nu = \int_0^\psi \frac{f(\mathcal{E})}{(\psi - \mathcal{E})^{\beta-\frac{1}{2}}} d\mathcal{E} \quad (1.28)$$

where we have solved the integral over  $\eta$ . Now this may not seem like an improvement on our first attempt, but it is saved by a standard result called the Abel integral. The Abel integral is a useful inversion formula which we will see again later. The inversion is as follows:

$$f(x) = \int_0^x \frac{g(t)}{(x-t)^\alpha} dt \rightarrow g(t) = \frac{\sin(\pi\alpha)}{\pi} \left[ \int_0^t \frac{dx}{(t-x)^{1-\alpha}} \frac{df(x)}{dx} + \frac{f(0)}{t^{1-\alpha}} \right] \quad (1.29)$$

This particular integral is especially useful in the mathematics of DFs because of how often one ends up solving equations of the form:

$$\frac{d\nu}{d\Psi} = \int_0^\Psi \frac{f(\mathcal{E})}{\sqrt{\Psi - \mathcal{E}}} d\mathcal{E} \quad (1.30)$$

where it is known as Eddington's formula (Eddington, 1916). So, if we apply this to our current system then we can find the troublesome  $f(\mathcal{E})$  section of our DF. This still isn't simple or necessarily analytic but it is a good start. Let us once again take a case where we want to find  $\beta = 1/2$  as this is, once again, a particularly convenient solution. This assumption leads us to the following solution of Eq. 1.28:

$$f(\mathcal{E} = \psi) = \frac{1}{2\pi^2} \frac{d}{d\psi}(r\nu) \quad (1.31)$$

We can solve this directly into a function of radius because we can ‘cheat’ a little bit and simply use the Plummer potential density pair. We could solve the isotropic case to derive it ourselves if we really wanted to but we can save ourselves a little time instead. We know the Plummer potential-density pair is simply:

$$\psi = \frac{1}{\sqrt{1 + (r/a)^2}}; \nu = \frac{3}{4\pi a^3} \left(1 + \frac{r^2}{a^2}\right)^{-\frac{5}{2}} \quad (1.32)$$

where  $a \equiv r_a$ . We can rearrange these relations to solve Eq. 1.31 and with that we can arrive at our DF:

$$f(\mathcal{E}) = \frac{3}{8\pi^3 a^2} \mathcal{E}^3 \left(5\sqrt{1 - \mathcal{E}^2} - \frac{1}{\sqrt{1 - \mathcal{E}^2}}\right) \quad (1.33)$$

If we were to solve this DF again we would recover a standard Plummer model with an anisotropy  $\beta = 1/2$ . However, there is still a problem with the model and this time it is something more serious than just mathematical inconvenience. If we plot the form of the DF we see that it has two main regions with different behaviour. At smaller values of  $\mathcal{E}$ , corresponding to larger radii, we see that the DF is always positive and gradually increases up to some maximum value of  $f(\mathcal{E})$ . At smaller radii  $\mathcal{E} \rightarrow 1$  and what we see is that  $f(\mathcal{E})$  drops very rapidly as shown in Fig. 1.1.

Of critical importance is the fact that there is no way to avoid that as  $r \rightarrow 0$  the model always follows  $f(\mathcal{E}) \rightarrow -\infty$  which is disastrous. Remember, at its most basic the DF represents a probability distribution and so must globally obey  $f(\mathcal{E}) \geq 0$  in order to be consistent. If the DF is anywhere negative then the probability of finding a particle at that position in phase-space cannot be meaningfully assessed and the model breaks down. In short, global non-negativity is a primary measure of the success of a DF.

What we have found is that our model will fail in a manner that is not found in isotropic versions of the same system as the usefulness of the isotropic Plummer sphere is well established. Additionally we have shown that it is not possible to simply force a given model to obey a certain anisotropy profile and it is non-trivial to assess which models will

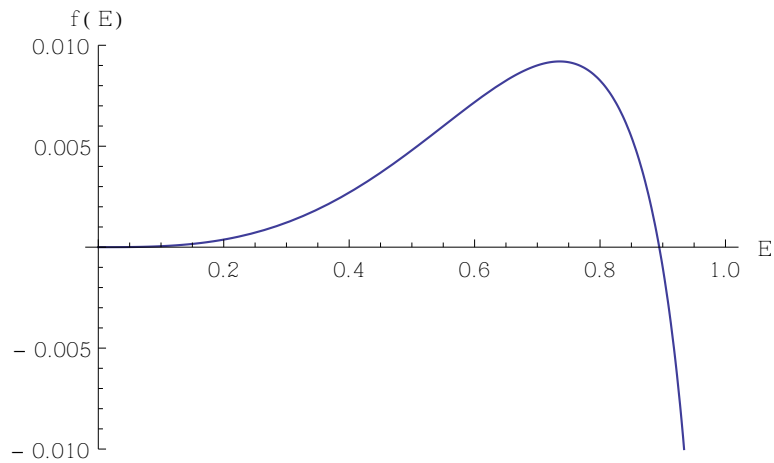


**Figure 1.1:** The energy function of a DF describing a Plummer sphere with a constant  $\beta = 1/2$ . Note the negativity of the DF, and hence the failure of the model, at small radii.

fail and which will succeed.

What we can take from this model is that the failure occurs at low radii around the region where a Plummer sphere is near to its constant density core. At large radii the density drops off as  $r^{-5}$  and the model seems to work. We may examine this relationship further if we examine a few more models and, along the way, discuss how to make a more realistic anisotropy description.

### 1.2.2 Examining constant anisotropy models

The methods of the previous section can be applied to a variety of models but there is no guarantee of whether the result will produce a viable system. Fortunately, finding solutions for these systems has been a major endeavour which has led to some measure of success. For example we can now move on to examine constant anisotropy Hernquist models.

Rather than solving the system ourselves, as we did for the Plummer model, we will instead use the results of Baes & Dejonghe (2002) from their exhaustive examination of the Hernquist model. They used a similar analysis routine to arrive at the DF for a constant anisotropy Hernquist model which they give as:

$$f(\mathcal{E}, L) = \frac{2^\beta}{(2\pi)^{5/2}} \frac{\Gamma[5 - 2\beta]}{\Gamma[1 - \beta]\Gamma[7/2 - \beta]} \times L^{-2\beta} \mathcal{E}^{5/2 - \beta} {}_2F_1\left(5 - 2\beta, 1 - 2\beta; \frac{7}{2} - \beta; \mathcal{E}\right) \quad (1.34)$$

where  ${}_2F_1$  is a hypergeometric series given by (Hazewinkel, 1994):

$${}_2F_1(a, b; c; z) = \sum_{n=0}^{\infty} \frac{(a)_n (b)_n}{(c)_n} \frac{z^n}{n!} \text{ where } (a)_n = a(a+1)(a+2)\dots(a+n-1) \quad (1.35)$$

This is an example of how simple DFs and simple potential-density pairs tend to be mutually exclusive. It's a little difficult to assess the complete behaviour of this system. However, all we really care about is the positivity of the system for a variety of anisotropies so we can make a few assumptions to simplify it.

First of all we know that the angular momentum will always be non-negative and so we can ignore factors of  $L$  for our analysis. Likewise, for bound particles we know that  $\mathcal{E}$  will always be positive as well and since the system is defined as bound we can ignore pre-factors of  $\mathcal{E}$  as well. Finally, we need to think about the various gamma functions.

From Eq. 1.24 we can see that none of our gamma functions will be negative for any value of  $\beta$  so we can equate the positivity of the DF with the behaviour of the hypergeometric series. If we plot our  $f(\mathcal{E})$  against the domain of  $\mathcal{E}$  we can check the positivity for a range of anisotropies.

As we can see from Fig. 1.2 we have three cases of interest. The DF is always positive for  $\beta \leq 1/2$  with the additional case that, as can be seen from the thick curve in Fig. 1.2,  $\beta = 1/2$  gives a constant value:

$$f(\mathcal{E}, L) = \frac{3}{4\pi^3} \frac{\mathcal{E}^2}{L} \quad (1.36)$$

This is also the last case that retains the property of global positivity. In every other case the DF will be negative for large values of  $\mathcal{E}$  which corresponds to small radii.

What we are seeing is that it is difficult to make a system with a large anisotropy when the density gradient is flatter. Specifically, in this instance we have a problem when we try

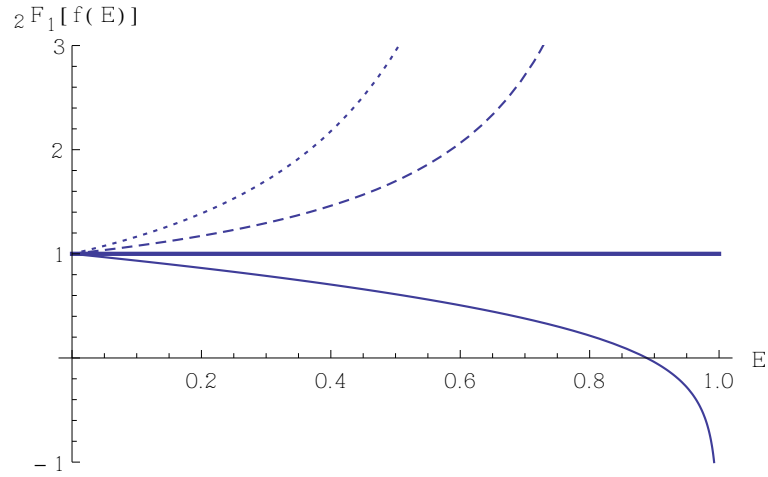


**Figure 1.2:** The hypergeometric series term for an anisotropic DF producing a Hernquist model as a function of  $\mathcal{E}$  for a variety of anisotropies. The different curves for  $\beta = \{0, 0.25, 0.50, 0.75\}$  are the dotted, dashed, thick, and thin lines respectively.

to set an anisotropy that is greater than half the magnitude of the density slope.

The Plummer sphere we developed actually didn't have a globally positive solution that generated anisotropy in the constant density core. In the Hernquist profile, which has a central cusp of  $r^{-1}$ , we cannot generate an anisotropy of more than  $\beta = 1/2$ . In fact, this result holds for all of the Dehnen models. A general DF for Dehnen models with  $\beta = 1/2$  is given by Buyle et al. (2007):

$$f(E, L, \gamma) = \frac{3 - \gamma}{8\pi^3 L} \left(1 - (1 - (2 - \gamma)E)^{1/(2-\gamma)}\right)^2 \left(4 - \gamma + \frac{\gamma - 1}{(1 - (2 - \gamma)E)^{1/(2-\gamma)}}\right) \quad (1.37)$$

where the parameter  $\gamma$  chooses the slope of central cusp according to Eq. 1.3. Again, we see that the last term in this DF will force the function to be negative if  $\gamma < 1$ . In other words, it would appear as if the density slope and the anisotropy are bound by the requirement that the former be at least twice as big as the latter.

To examine this in some detail we need to look at something more than just the simple cases of constant anisotropy and to do *that* we need a more powerful method.

It should be noted that the assumption of constant anisotropy is not without its uses. For instance the analysis of Ma & He (2008) used a simple  $\beta = 1/2$  model to generate

anisotropic DFs for dark matter halos using NFW and Moore profiles. However, it must still be acknowledged that real systems tend to have more complex anisotropy profiles and one must be cautious when extending the results from simpler models.

### 1.2.3 Osipkov-Merritt models and the Cuddeford generalisation

If you want to try and construct an analytical DF for a particular potential density pair then your options are rather limited. One of the few ways to do this reliably is by using the method of Osipkov (1979) and Merritt (1985) which is essentially an extension of the methods that we have used so far.

In the Osipkov-Merritt formalism the energy dependence of the system is expanded to include an angular momentum term:

$$f(\mathcal{E}, L) = f(Q) = f\left(\mathcal{E} - \frac{L^2}{2r_a^2}\right) \quad (1.38)$$

where the term  $r_a$  is a radius which determines the shape of the anisotropy profile.

If we make the substitution into the polar coordinate space that we used back in Eq. 1.20 then we can recover the following form of Eq. 1.21:

$$\nu(r) = 2\pi \int_0^\pi \sin \eta \, d\eta \int_0^\psi f(Q) \frac{\sqrt{2(\psi - Q)}}{(1 + (r/r_a)^2 \sin^2 \eta)^{3/2}} \, dQ \quad (1.39)$$

which inverts into a rather familiar equation:

$$f(Q) = \frac{1}{\sqrt{8\pi^2}} \left[ \int_0^Q \frac{d\psi}{\sqrt{Q - \psi}} \frac{d^2\nu_Q}{d\psi^2} + \frac{1}{\sqrt{Q}} \left( \frac{d\nu_Q}{d\psi} \right)_{\psi=0} \right] \quad (1.40)$$

thanks to the striking similarity to the Abel integrals we have already been dealing with back in Eq. 1.29. This construction has a number of nice features that spring from the familiarity of this result not least of which is the simple relationship between the density of these models and the isotropic model:

$$\nu_Q(r) = \left(1 + \frac{r^2}{r_a^2}\right) \nu(r) \quad (1.41)$$

We can also use the results from the velocity dispersions of these systems to find a

general result for the anisotropy profile:

$$\beta(r) = \frac{1}{1 + r_a^2/r^2} \quad (1.42)$$

This is the problem, at least for us, with Osipkov-Merritt models. The system is always anisotropic at  $r = 0$  and will be nearly isotropic for all  $r \ll r_a$  before smoothly becoming more radially anisotropic for  $r \gg r_a$ . This is very good for most systems, but we are wanting to discuss models with a central anisotropy  $\beta_0 > 0$ . For that we need a different formalism such as the one provided by Cuddeford (1991).

In this system the Osipkov-Merritt model is extended according to:

$$f(\mathcal{E}, L) = f_0(Q) L^{-2\beta} \quad (1.43)$$

This minor alteration gives us a similar density profile:

$$\nu_Q(r) = r^{-2\beta} \left(1 + \frac{r^2}{r_a^2}\right)^{\beta_0-1} \nu(r) \quad (1.44)$$

but, importantly, yields a much more flexible anisotropy profile:

$$\beta(r) = \frac{1 + \beta_0 r_a^2/r^2}{1 + r_a^2/r^2} \quad (1.45)$$

This reduces to the Osipkov-Merritt profile for the case of  $\beta_0 = 0$  and a comparison of the two profile shapes is given in Fig. 1.3. In particular we note that the Cuddeford models allow the central anisotropy to be specified with the rest of the model describing the increasing radial anisotropy.

So now we can yet again go through the process of inverting the expression for density into one for the DF through the Abel integral to produce a generalised expression for Cuddeford models. It is more difficult than in our simple example but with suitable choice of variables and differentials an analogous form can be found. The principle difficulty comes from the requirement for repeated differentiations depending on what anisotropy is desired (Cuddeford, 1991). The general solution is:

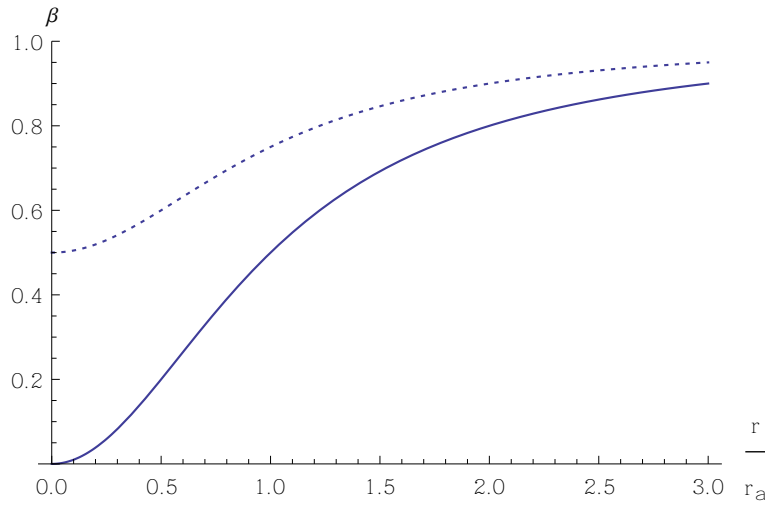


**Figure 1.3:** A comparison of the anisotropy profiles created by Osipkov-Merritt (solid) and Cuddeford (dotted) models. The Cuddeford model uses  $\beta_0 = 1/2$ .

$$f(\mathcal{E}, L) = \frac{2^{\beta_0}}{(2\pi)^{3/2}} \frac{L^{-2\beta_0}}{\Gamma[1 - \beta_0]\Gamma[1 - m]} \frac{d}{dQ} \int_0^Q \frac{d^n f(\mathcal{E}, L)}{d\psi^n} \frac{d\psi}{(Q - \psi)^m} \quad (1.46)$$

where we need to define a few terms to deal with the unusual amount of differentiation:

$$n = 1 + \left\lceil \frac{1}{2} - \beta_0 \right\rceil; m = \left( \frac{1}{2} - \beta_0 \right) - \left\lceil \frac{1}{2} - \beta_0 \right\rceil \quad (1.47)$$

where  $\lceil x \rceil$  is the ceiling function (Hazewinkel, 1994).

As you can perhaps appreciate this DF is very difficult to evaluate for generic values of  $\beta_0$  and most treatments limit themselves to the simpler solutions for integer or half integer values as these cases are the only ones with analytical solutions. This is a slight problem for us here as we are interested in analytical solutions where  $\beta_0 > 1/2$  but none exist.  $\beta_0 = 1$  is technically such a case but since the inversion is only valid for  $\beta_0 < 1$  (Cuddeford, 1991) we cannot use that case either.

However, an examination of the system can still give us some insights. If the anisotropy radius is allowed to tend towards infinity then we will recover a system with constant anisotropy which we already have tested. Additionally, allowing the anisotropy radius to decrease will only cause the anisotropy to increase at a given radius. In other words if a constant anisotropy system would fail to have a globally positive DF due to a high anisotropy then a Cuddeford model of the same system would never be an improvement.

This means that the results for our constant anisotropy Hernquist model still stand for the Cuddeford model (Baes & Dejonghe, 2002).

#### 1.2.4 Factors for DF positivity

The final point we will cover for this chapter is to mention that the relationship between anisotropy and the DF is far from the be-all and end-all of DF positivity. We will discuss this extensively in the next chapter but what we have been uncovering is an established result stating that the anisotropy can never exceed half the logarithm of the density slope. This relationship is outlined in Ciotti & Morganti (2010b) and is known as the general density-slope anisotropy inequality.

That will be the focus of the next chapter but for now we will just prove that a DF can be negative without this being due exclusively to the anisotropy. Thinking back to the constant anisotropy Plummer model we found that, due to the constant density core, the model cannot be radially anisotropic at small radii. Armed with only this fact and the inequality of Ciotti & Morganti (2010b) we might perhaps expect that we can predict the positivity of the DF.

We could, for example, assume that any Cuddeford models with  $\beta_0 > 0$  would have negative DFs which, for the Plummer model at least, is accurate. However, we might suppose that Osipkov-Merritt models would be allowed due their behaviour that  $\beta_0 = 0$  at the centre of the system.

This has been examined in Dejonghe (1987) although with a more flexible anisotropy profile than the Osipkov-Merritt model allows. In that paper an analytical set of solutions was found which produced Plummer spheres with an anisotropy given by a parameter  $q$ :

$$\beta = \frac{q}{2} \frac{r^2}{1 + r^2} \quad (1.48)$$

This generalisation is different to that of Cuddeford (1991) as the anisotropy at the core is always zero like an Osipkov-Merritt model but the anisotropy radius is implicit rather than explicit. Incidentally, the generalisation recovers an Osipkov-Merritt type anisotropy profile for  $q = 2$ .

Once again the DF is found by setting up a specific form of the density that is amenable

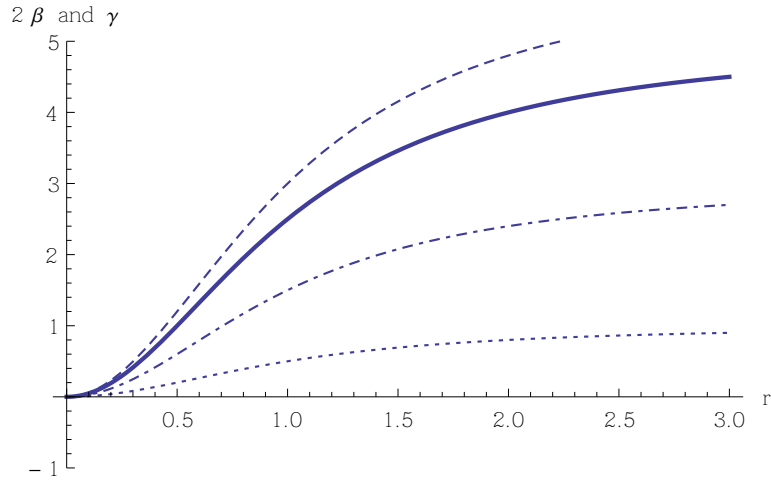


**Figure 1.4:** A comparison of  $2\beta$  against the logarithmic density slope. The slope of the density profile is the thick curve while anisotropy profiles for  $q=1, 3, 6$  are the dotted, dot-dashed, and dashed curves respectively. Note that the anisotropy curves are  $2\beta$  rather than  $\beta$  for direct comparison. Curves above the density slope profile are expected to cause a negative DF.

to inversion. We have gone over the mechanics of these inversions in detail so we shall just state the result of Dejonghe (1987). The DF to generate anisotropic Plummer spheres is:

$$f(\mathcal{E}, L) = \frac{3\Gamma[6-q]}{2(2\pi)^{5/2}\Gamma[9/2-q]} \mathcal{E}^{7/2-q} {}_2F_1\left(p/2, q-7/2; 1; \frac{L^2}{2\mathcal{E}}\right) \quad (1.49)$$

We should note that the full function is larger but we have simplified it here as we are only interested in a very specific case. As with previous models the fact that we are only interested in the positivity of the DF means we can neglect a large amount of the DF since the positivity is once again entirely dependent on the behaviour of only one component. Accordingly, as before, if we understand the positivity of the hypergeometric series then we will understand the positivity of the DF.

But first, we can make a prediction based on our experiences of the anisotropy relation. It is simple to plot twice the anisotropy profile against the power law of the density slope to produce Fig. 1.4.

We can actually examine the relationship between the anisotropy and the density slope directly since we have analytical expressions for both of them:

$$2\beta = \frac{qr^2}{1+r^2}; \frac{d \log \rho}{d \log r} = \frac{d \log}{d \log r} \left( \frac{3}{4\pi(1+r^2)^{5/2}} \right) = \frac{5r^2}{1+r^2} \quad (1.50)$$

If we set these two terms equal to each other then we can solve for the value of  $q$  at which we would expect the change from a positive to a negative DF to occur. Doing so gives us the simple result of  $q = 5$ . This is a rather interesting result as we should immediately notice that a value that large will very quickly produce an anisotropy that is physically impossible; a system that is more than twice as radial as a completely radial system. We could take this to reasonably mean that we can set any value for the anisotropy of these models and as long as it is physically meaningful then it will never lead to a negative DF.

This is a very neat result and makes this system of modelling very useful for producing Plummer spheres, but we are interested in this because of what it implies about the positivity. If the anisotropy cannot meaningfully go above  $\beta = 1$  then any system that claims to do so must be non-physical. If it is non-physical then it must necessarily have a negative DF so that the model cannot be produced. To achieve an anisotropy of  $\beta = 1$  at large radii we require  $q = 2$  which means that this value for  $q$  must be the real limit on the DF positivity.

In other words, what we have proved is that the rule where the anisotropy cannot exceed half the logarithmic density slope is not a necessary condition for a positive DF. It is sufficient but there are other factors which may be of greater importance.

Now we have a robust understanding of the background to the DF formalism and have introduced a little of the results from Ciotti & Morganti (2010b) we may now embark on a much more detailed examination.



# 2

## The General Density-Slope Anisotropy Inequality in non-separable systems

*“Everyone has an equal right to inequality.”*

— *John Ralston Saul*

In the last chapter we covered a lot of material to do with the business of finding DFs and solving models in order to use or plot them. In this chapter we are going to expand on this a little more by looking at one problem in much greater detail. Throughout the latter half of chapter 1 we ran into an apparent relationship between the density slope and the anisotropy profile and it is that that we are going to investigate. This will obviously use a large amount of the material that we discussed in the previous chapter so, to summarise, the key points are as follows.

It is often difficult to derive the anisotropy of a system from observational data as the lack of 3D velocity information makes it difficult to arrive at an unambiguous result. It is

thus extremely useful to find constraints and relationships that allow the anisotropy to be known as a function of more easily observed variables such as density.

Usually a particular potential or density profile will be chosen to model a particular system of interest. The most effective and powerful presentation of such a system is the phase-space distribution function (DF) which is connected to observable, real-space quantities of a system via various integral relations. Because the DF is a probability distribution that describes the phase-space of a system there are some fundamental requirements for a DF that produces a viable system. The most basic constraint is the positivity of the DF over the entire permitted domain of the system as while a system with a positive DF may not be stable, but a system with a negative DF cannot even be created.

The relationship between a density profile and a DF is complicated and is not even one-to-one (Dejonghe, 1987). Since the DF describes the full six-dimensional shape of the system there are multiple possible DFs that can produce the same density profile which only differ through, for example, their anisotropy profiles. Accordingly, it is very important to be able to derive unambiguous analytical expressions for a system of interest so that the positivity can be known precisely.

The main problem here is that the process of finding an expression for the DF of an arbitrary system is highly non-trivial and can usually not be done analytically. The most reliable method of finding a DF is through Eddington's formula (Eddington, 1916) which inverts the integral relationship between the density and the DF, however even this is only analytic for a selection of density profiles and parameters.

So in general, while specific models and schemes to produce analytical DFs for a given density do exist, there is a pressing need for simple, fundamental relationships between the quantities of a system that can constrain the positivity of a DF. A way to look at a particular model and know, without having to work through the inversions, whether or not the DF is likely to be positive would be ideal.

One particularly important result was that of Ciotti & Pellegrini (1992) who found a simple criteria for the consistency of models using an Osipkov-Merritt anisotropy scheme. This paved the way for a dramatic expansion in the scope of relations between DF positivity and anisotropy profiles, which would eventually lead to the birth of the result we will be examining. The first major step towards a completely general analytical constraint was

---

made by Hansen (2004) in the form of hard constraints on the conditions in the centre of a dark halo under reasonable assumptions of spherical symmetry, a power law phase-space density (Taylor & Navarro, 2001), and the requirement for physical solutions to the Jeans Equations (which we will be discussing shortly). They found that any system with an inner density profile  $\rho \propto r^{-\gamma}$  would obey  $1 + \beta \leq \gamma \leq 3$  where  $\beta$  is the velocity anisotropy parameter.

This was subsequently improved until the relation could constrain a non-negative DF (An & Evans, 2006) in multi-component systems (Ciotti & Morganti, 2009) and Cuddeford models (Cuddeford, 1991; Ciotti & Morganti, 2010a) which contain the Osipkov-Merritt models as a special case. After the discovery that the constraints held even for systems outside these model groups (Ciotti & Morganti, 2010c) there was an effort made to define exactly how universal such constraints could be. This led to the significant result of Ciotti & Morganti (2010b) where it was proven that a large class of models obey the relation:

$$\gamma \geq 2\beta \tag{2.1}$$

This relationship was termed the Global Density Slope-Anisotropy Inequality (GDSAI) and was shown to be strongly connected to the positivity of the DF in this broad class of multi-component models Cuddeford models as well as in a variety of other anisotropic systems. Specifically, the work of Van Hese et al. (2011) showed that obeying the GDSAI is a necessary condition for DF positivity in models where the central anisotropy was  $\beta_0 \leq 0$  but did demonstrate counter-examples for larger anisotropies.

All the systems that had been investigated and had a proven relationship to the GDSAI fall into the category of models with separable augmented density. An augmented density is one that can be described only in terms of a potential as a function of radius and the radius itself. A separable model of this kind can be described thusly:

$$\rho(r) = \rho_{aug}(\psi(r), r) = f(\psi)g(r) \quad 0 \leq \psi \leq \psi_0 \tag{2.2}$$

where we alter the usual notation for the augmented density to avoid later confusion with our dimensionless variables. Here, the density profile is given by  $\rho$  and  $\psi$  is the positive, relative potential. To be clear, when we speak of the requirement for separability we

are referring to the density profile and are requiring the density to be expressed in two separate functions of radius and potential. This is distinctly different from the DF being separable and we are not interested in the separability of the DF, only the separability of the augmented density.

Since the GDSAI has been proved for all separable augmented systems with  $\beta_0 \leq 1/2$  and is understood in such systems with  $\beta_0 > 1/2$ , we will investigate the behaviour of augmented systems which are non-separable. We accomplish this by using mono-energy DFs that produce non-separable density profiles which, while highly artificial, are also comparatively easy to understand and analyse.

We present a simple spherical model that significantly violates the GDSAI over a range of radii, produces systems with  $\beta_0 = 0$ , and has a globally positive DF. The DF is a mono-energy halo that is separable in  $E$  and  $L^2$  and produces a non-separable augmented density profile. We suggest that this is evidence that the GDSAI cannot be extended to all non-separable systems and cannot be used to constrain the positivity of their DFs. We instead suggest that, since our DF is not guaranteed to be dynamically stable, system stability is still the principle measure that can confirm whether such non-separable systems can be created and kept in equilibrium.

So, in §2.1 we briefly confirm the inadequacies of a purely Jeans Equation-based approach, §2.2 shows our construction of a simple system that does not follow the inequality, §2.3 examines the practical implications of the system, §2.4 examines the stability of the system, §2.5 describes possible generalisations of our model, and §2.6 concludes.

## **2.1 The inadequacy of a Jeans' equation approach**

It is already known that the criteria provided by the Jeans' equations are not as stringent as testing for the positivity of the distribution function. However, there are mathematical difficulties associated with calculating properties of most general DFs which mean the Jeans' equations are still relevant. We will demonstrate why apparently simple violations of the GDSAI which rely on the Jeans' equations are insufficient to disprove it, as noted in Ciotti & Morganti (2010b). This is done by creating a density profile from two simple, superimposed models which, together, should apparently break the GDSAI according to the Jeans' equation. We will then show why the model fails to achieve this by being

unphysical in a way that the Jeans' equations cannot indicate.

First we examine the derivation of the Jeans' equations. The Jeans' equations are a useful tool which can relate the observable quantities of a system which can be derived from the DF by treating the movement of stars like the motion of a fluid. We begin from a description of fluid flow where the change in mass contained within a surface is equated to the flux of matter through the surface. This yields the continuity equation:

$$\frac{\partial \rho}{\partial t} + \nabla \cdot (\rho \dot{\mathbf{x}}) = 0 \quad (2.3)$$

This describes the conservation of matter but can also express a conservation of probability by using the full coordinate space and the DF:

$$\frac{\partial f}{\partial t} + \nabla \cdot (f [\dot{\mathbf{x}}, \dot{\mathbf{v}}]) = 0 \quad (2.4)$$

Expanding this gives us the first step towards the Jeans' equation:

$$f \sum_{i=1}^3 \left[ \frac{\partial v_i}{\partial x_i} + \frac{\partial \dot{v}_i}{\partial v_i} \right] + \sum_{i=1}^3 \left[ v_i \frac{\partial f}{\partial x_i} + \dot{v}_i \frac{\partial f}{\partial v_i} \right] = 0 \quad (2.5)$$

We can eliminate some of the terms of this equation immediately. All terms of the form  $\partial v_i / \partial x_i$  can be removed as we know that  $x_i$  and  $v_i$  are independent coordinates. We also know that  $\partial \dot{v}_i / \partial v_i$  can be removed as the acceleration is a function of  $\partial \Phi / \partial x_i$  not  $v_i$ . The result is known as the collisionless Boltzmann equation (CBE).

If we use the spherical Hamiltonian of the system we can cast our result into spherical coordinates. Using spherical coordinates allows us to simplify the system by using symmetry arguments to remove angular differentials. We can also assume that the system is time-independent which removes differentials in time. The resulting spherical CBE can then be constructed in terms of momenta,  $p_i$ , and is given by:

$$p_r \frac{\partial f}{\partial r} + \frac{p_\theta}{r^2} \frac{\partial f}{\partial \theta} - \left( \frac{\partial \Phi}{\partial r} - \frac{p_\theta^2}{r^3} - \frac{p_\phi^2}{r^3 \sin^2 \theta} \right) \frac{\partial f}{\partial p_r} - \frac{p_\theta^2 \cos \theta}{r^2 \sin^3 \theta} \frac{\partial f}{\partial p_\theta} = 0 \quad (2.6)$$

In order to solve this further we need to find a useful substitution for our DF. First we should redefine our momenta in terms of the spherical coordinates used by our system:

$$p_r = \dot{r} = v_r; p_\theta = r^2 \dot{\theta}; p_\phi = r^2 \sin^2 \theta \dot{\phi} = r \sin \theta v_\phi \quad (2.7)$$

which allows us to redefine the DF in terms of velocities:

$$\int dp_r dp_\theta dp_\phi f = r^2 \sin \theta \int dv_r dv_\theta dv_\phi f = r^2 \sin \theta \nu \quad (2.8)$$

To arrive at the Jeans' equation from this we must multiply by a factor of  $p_r dp_r dp_\theta dp_\phi$  and integrate. This eventually reduces to the Jeans' equation as follows:

$$\frac{d(\nu \bar{v}^2)}{dr} + 2 \frac{\beta}{r} \nu \bar{v}^2 = -\nu \frac{d\phi}{dr} \quad (2.9)$$

The principle is that any system that violates this expression will be time-dependent and thus the phase-space density will not be static. This implies that the system is evolving and is not stable in its current configuration. This is useful for determining some of the general properties of a system but is less descriptive than the DF.

So, the system we construct is created by overlaying a large cusped model from the Zhao (1996) family of models onto a smaller, cored, Hernquist model (Hernquist, 1990) to create a structure with the density profile shown in Fig. 2.1 described by:

$$\rho = \frac{1}{r(1+r)^3} + \frac{5 \times 10^5}{(7+r)^4} \quad (2.10)$$

$$\phi = -\frac{2\pi(7000147 + 8500042r + 1500003r^2)}{3r(1+r)(7+r)^2} \quad (2.11)$$

The smaller model has a cusp with  $\rho \propto r^{-1}$  in the centre transitioning to  $\rho \propto r^{-4}$  while the larger of the two models is cored. This means the constant density core extends past the point where the smaller model has declined to  $r^{-4}$ . This creates a region in between the  $r^{-1}$  cusp and the  $r^{-4}$  halo where the Hernquist profile starts to dominate leading to a flattening of the density profile. In this region the density slope is very close to zero, so

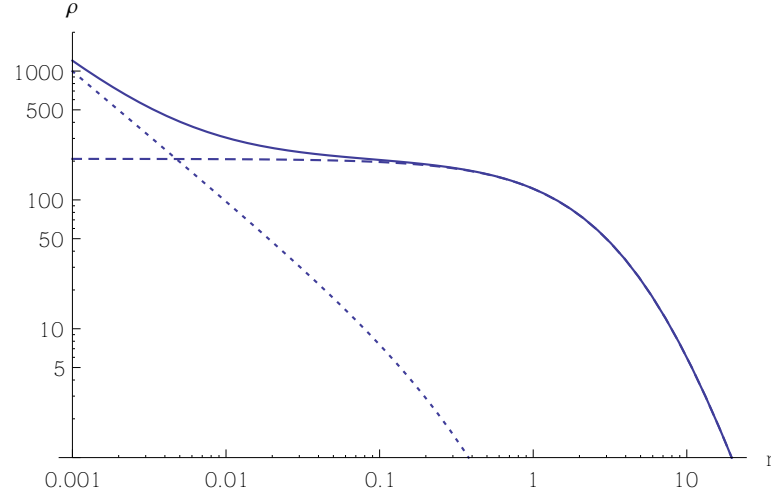


**Figure 2.1:** Density profiles of a simple composite model designed to violate the GDSAI. The dashed and dotted lines are the  $1/r(1+r)^3$  cusped and  $5 \times 10^5/(7+r^4)$  cored subsidiary models while the solid line is the sum of the two profiles.

if we state that our system has an anisotropy of  $\beta = 1/2$  everywhere then the system will not follow the inequality.

So, we then attempt to solve the Jeans' equation for the system:

$$-\frac{d(\rho\sigma_r^2)}{\rho dr} - \frac{2\beta\sigma_r^2}{r} = \frac{d\phi}{dr} \quad (2.12)$$

We want to solve this for  $\sigma_r^2$  so we can express this as follows assuming constant  $\beta$ :

$$\rho r^{2\beta} \sigma_r^2 = \int_r^\infty \rho r^{2\beta} \frac{d\phi}{dr} dr \quad (2.13)$$

By definition, we can replace  $\frac{d\phi}{dr}$  with terms of density instead:

$$\rho r^{2\beta} \sigma_r^2 = \int_r^\infty \rho r^{2\beta} \frac{G}{r^2} \left[ \int_0^r 4\pi r^2 \rho dr \right] dr \quad (2.14)$$

A full, rigorous treatment of this integral can be performed, however the density function is sufficiently complex that the analytical result is too large to be worth reproduction here. The result is a collection of hypergeometric series which depend, in part, upon  $\beta$ .

The problem is that the result for  $\sigma_r^2$  is not defined for all values of  $\beta$ . If  $\beta$  is such that

$\beta \geq 1/2$  then our expression will include instances of evaluating  $1/0$  which is undefined. In other words, we cannot evaluate  $\sigma_r^2$  for  $\beta \geq 1/2$  meaning that any attempt to force an anisotropy which violates the GDSAI results in an unphysical solution.

The problem is that it is difficult to predict this failure in advance of solving a specific instance of the Jeans' equation. The separate components of the model are both independently stable, so nothing immediately seems to be wrong with the system that we attempted to create. Rather than working through large numbers of possible models to find combinations of parameters that work, it is easier to work directly with distribution functions.

For instance, with the benefit of a little *a priori* knowledge, we could have known this system would not be physical. In a system such as this we can assume that the distribution function follows the form (Cuddeford, 1991):

$$f(E, L) = L^{-2\beta} F(E); F(E)|_{E=\phi} = -\frac{d(r\rho)}{d\phi} \quad (2.15)$$

where we assumed the form of the function  $F(E)$  according to An & Evans (2006) assuming that  $\beta = 1/2$ . The problem is that the angular momentum term will always be positive but if we look at the energy term there is one region where  $F(E)$  is locally negative. We can see this more clearly by breaking down the expression for the energy function:

$$F(E) = -\frac{d(r\rho)}{d\phi} = -\frac{d(r\rho)}{dr} \frac{d\phi}{dr} \quad (2.16)$$

To be clear, given that we need the entire energy term to be non-negative and non-zero everywhere, we require  $\frac{d(r\rho)}{dr} \frac{d\phi}{dr} < 0$ . However, the term  $\frac{d\phi}{dr}$  is always going to be positive as  $\frac{d\phi}{dr} \equiv \frac{GM(<r)}{r^2}$  and clearly neither the radius nor the contained mass will be able to become negative. The problem comes from the other term,  $\frac{d(r\rho)}{dr}$ , i.e. the requirement that  $\rho$  must fall steeper than  $r^{-1}$ .

The problem is highlighted in Fig. 2.2 where we see that  $r\rho$  rises for all small radii, meaning the gradient is positive. This is the region that we are interested as it contains the transition between the two components of our model and the region in which we were investigating the inequality. However, since the gradient is positive here, our energy

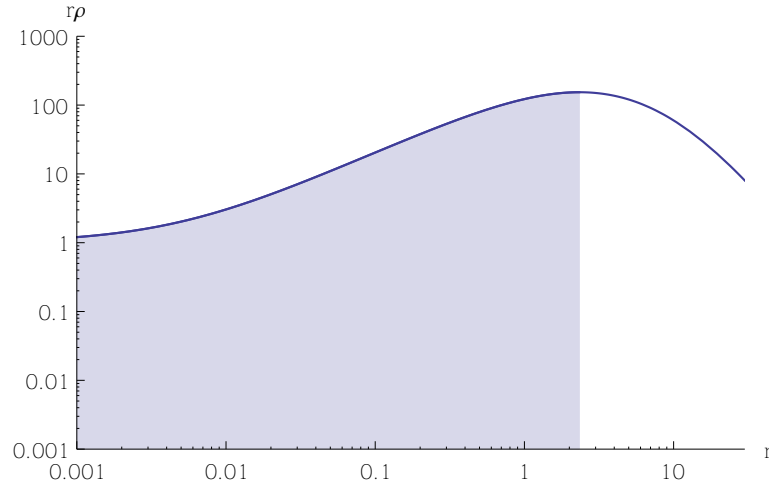


**Figure 2.2:** Plot of  $r\rho$ , the differential of which comprises half of the energy function of Eq. 2.16. As discussed, we require this function to have a negative gradient everywhere in order for the DF to be non-negative. This figure shows that everywhere where the model could potentially fail to follow the GDSAI has a positive gradient, indicated by the shaded areas, strongly suggesting the model is unphysical.

function Eq. 2.16 will be negative. This has the unfortunate implication that there is a significant section of our system for which the DF is negative overall; *the system is unphysical*.

In other words, the one region where we might see violation of the inequality is unphysical by definition. If we are to investigate the GDSAI we are going to have to start with the DF and work up, rather than the other way around.

## 2.2 The Distribution Function approach

We set up a system where the DF is defined as:

$$f(E, L) = A\delta(E - E_0)H(L_{cut}^2 - L^2) \quad (2.17)$$

where the constant  $A$  is for dimensional consistency. This represents a system where all allowed orbits have exactly energy  $E_0$  and must have angular momentum  $L^2$  under  $L_{cut}^2$  as defined by a delta function and a Heaviside function:

$$H(L_{cut}^2 - L^2) = \begin{cases} 1 & \text{if } L^2 < L_{cut}^2 \\ 0 & \text{if } L^2 > L_{cut}^2 \end{cases} \quad (2.18)$$

This system is actually a type of polytropic model developed by Polyachenko et al. (2013) to study radial orbit instability. The model we use is equivalent to their  $q=-1$  mono-energy model and is interesting to us for its non-monotonic density profile. Given that the DF is potentially of interest, we wish to extract density and anisotropy profiles from it to examine in detail.

### 2.2.1 Finding density

As we showed in chapter 1 the density is defined as the integral of the DF over all velocity space:

$$\rho(r) = \int f(E, L) dv_x dv_y dv_z = \int f(E, L) dv_r dv_\theta dv_\phi \quad (2.19)$$

To ease the subsequent integration we express the integration variables in terms of E and L which we do by solving only for a constant radius, r. We use the following relationships between the velocity components:

$$v_\theta^2 + v_\phi^2 = \frac{L^2}{r^2} \quad (2.20)$$

$$v_r = \sqrt{2} \sqrt{E - \Phi(r) - \frac{L^2}{2r^2}} \quad (2.21)$$

which we then use to rewrite our integration variables:

$$dv_r dv_\theta dv_\phi = \frac{dE}{v_r} \frac{\pi}{r^2} dL^2 \quad (2.22)$$

We first integrate with respect to E. This is simple as there is only one function of E, namely  $v_r$ , and the delta function makes the integration trivial. We are then just left with the integration of  $L^2$ :

$$\rho = \frac{A\pi}{r^2} \int_0^{L_{cut}^2} \left[ 2 \left( E_0 - \Phi - \frac{L^2}{2r^2} \right) \right]^{-\frac{1}{2}} dL^2 \quad (2.23)$$

where a similar trick was employed to deal with the Heaviside function as it has the property of constraining the limits of integration. We thus end up with an expression for the density:

$$\rho = 4A\sqrt{2\pi} \left( \sqrt{E_0 - \Phi} - \sqrt{E_0 - \Phi - \frac{L_{cut}^2}{2r^2}} \right) \quad (2.24)$$

The second square root term can become imaginary for small values of  $r$  or particularly large values of  $L_{cut}^2$ . This represents parts of the system where all real orbits of the system lie under the angular momentum threshold. Consequently the only excluded orbits, which are those represented by the second term, are those which do not correspond to real possible states of the system. We avoid mathematical inconsistency in such cases by only taking the real component of the result *i.e.* 0.

### 2.2.2 Finding anisotropy

Next we find an expression for the anisotropy profile. We start from the definition:

$$1 - \beta(r) = \frac{\sigma_\theta^2 + \sigma_\phi^2}{2\sigma_r^2} \quad (2.25)$$

We now use the fact that  $v^2\rho$  gives us the pressure along a given axis and combine it with our definition from Eq. 2.19. This allows the velocity dispersion to be written as:

$$\sigma_r^2 = \frac{\int v_r^2 f(E, L) d^3v}{\rho(r)} \quad (2.26)$$

and likewise for  $\sigma_\theta^2 = \sigma_\phi^2$ . We can apply this to Eq. 2.25 and cancel the factors of  $\rho(r)$  because symmetry tells us they are equivalent. After changing variables we are left with the following:

$$1 - \beta(r) = \frac{\int \left( \frac{L^2}{r^2} \right) f(E, L) \left( 2 \left[ E - \Phi(r) - \frac{L^2}{2r^2} \right] \right)^{-\frac{1}{2}} dL^2 dE}{\int (2v_r^2) f(E, L) dE dL^2} \quad (2.27)$$

As before we easily perform the integration over  $E$  and use the Heaviside functions to place limits on the integration over  $L^2$  but the resulting expression is more complicated:

$$1 - \beta(r) = \frac{\frac{1}{\sqrt{2}} \int_0^{L_{cut}^2} \left(\frac{L^2}{r^2}\right) \left(E_0 - \Phi(r) - \frac{L^2}{2r^2}\right)^{\frac{-1}{2}} dL^2}{2\sqrt{2} \int_0^{L_{cut}^2} \left(E_0 - \Phi(r) - \frac{L^2}{2r^2}\right)^{\frac{1}{2}} dL^2} = \frac{1}{4} \frac{\mathbb{I}_1}{\mathbb{I}_2} \quad (2.28)$$

For clarity we will solve each integral individually as they require substitutions to be easily soluble. We consider the numerator first and make a substitution of  $Y = L^2/L_{cut}^2$  to make the problem dimensionless:

$$\begin{aligned} \mathbb{I}_1 &= \int_0^{L_{cut}^2} \frac{L^2}{r^2 \sqrt{E_0 - \Phi(r) - \frac{L^2}{2r^2}}} dL^2 \\ &= \frac{L_{cut}^4 \sqrt{2}}{r \sqrt{L_{cut}^2}} \int_0^1 \frac{Y}{\sqrt{\frac{2r^2}{L_{cut}^2} [E_0 - \Phi(r)] - Y}} dY \end{aligned} \quad (2.29)$$

Similarly for the denominator we make the same substitution:

$$\begin{aligned} \mathbb{I}_2 &= 2\sqrt{2} \int_0^{L_{cut}^2} \sqrt{E_0 - \Phi(r) - \frac{L^2}{2r^2}} dL^2 \\ &= \frac{2L_{cut}^3}{r} \int_0^1 \sqrt{\frac{2r^2}{L_{cut}^2} [E_0 - \Phi(r)] - Y} dY \end{aligned} \quad (2.30)$$

These integrals can be solved analytically and the result for  $\beta$  expressed as:

$$\beta = \frac{\sqrt{1-x} \left(\frac{3x}{2}\right)}{1 - (1-x)^{\frac{3}{2}}} \text{ where } x = \frac{L_{cut}^2}{2r^2 (E_0 - \Phi)} = \frac{L_{cut}^2}{r^2 v_{esc}^2} \quad (2.31)$$

where  $v_{esc}$  is the escape velocity required for a particle to escape to the boundary of the system as opposed to escaping to  $r \rightarrow \infty$ .

As with the density profile the anisotropy profile can produce imaginary results if  $x > 1$  in regions where  $\frac{L_{cut}^2}{r^2} > \frac{L_{max}^2}{r^2}$ . This, again, corresponds to regions of the system where all real orbits lie below the angular momentum threshold. Since we know that this case

is not physical we resolve it by enforcing a maximum value such that  $\forall x > 1, x = 1$ . This constrains the angular momentum threshold to be locally no greater than the largest possible angular momentum at radii where the imaginary numbers would otherwise be produced. This does not change the physical implications of the formula and just ensures mathematical consistency.

We can calculate  $\sigma_r^2$  by using Eq. 2.26 and following a similar line of reasoning as for the anisotropy. Using the parameterisation from Eq. 2.31 yields:

$$\sigma_r^2 = \frac{2(E_0 - \Phi) \left[ 1 - (1 - x)^{\frac{3}{2}} \right]}{9(1 - \sqrt{1 - x})} \quad (2.32)$$

The tangential dispersions can either be found similarly or by combining the radial dispersion with the anisotropy. They won't be reproduced here as they are not used in our analysis.

### 2.2.3 Finding potential

We can use Poisson's equation to find the potential by integrating the following second order ordinary differential equation:

$$\frac{d^2(r\Phi)}{4\pi G r dr^2} = 4\sqrt{2}\pi A \left( \sqrt{E_0 - \Phi} - \sqrt{E_0 - \Phi - \frac{L_{cut}^2}{2r^2}} \right) \quad (2.33)$$

where, to be rigorous, we have included the dimensional pre-factor  $A$  from our DF of Eq. 2.17. This can be cast into a dimensionless form by the following scaling:

$$r = B\tilde{r}; \Phi = E_0 - C\tilde{\Psi} \rightarrow \frac{d(E_0 - \tilde{\Psi})}{d\tilde{r}} \equiv -\frac{d\tilde{\Psi}}{d\tilde{r}}; L^2 = B^2 C \tilde{L}^2 \quad (2.34)$$

where we require that  $C = (AB^2G)^2$  for consistency. This gives us the following dimensionless expression that requires solving:

$$-\frac{1}{4\pi\tilde{r}^2} \frac{d}{d\tilde{r}} \left( \tilde{r}^2 \frac{d\tilde{\Psi}}{d\tilde{r}} \right) = 4\sqrt{2}\pi \left( \sqrt{\tilde{\Psi}} - \sqrt{\tilde{\Psi} - \frac{\tilde{L}_{cut}^2}{2\tilde{r}^2}} \right) = 4\sqrt{2}\pi\tilde{\rho}(\tilde{r}) \quad (2.35)$$

As before we have a non-physical case for small  $r$  and large  $L_{cut}^2$  which we resolve by

taking only the real part of the root. To solve the ODE we apply standard initial conditions that:

$$\tilde{\Psi}(\tilde{r} = 0) = (4\pi)^2; \frac{d\tilde{\Psi}(\tilde{r} = 0)}{d\tilde{r}} = 0 \quad (2.36)$$

where the choice of the constant  $(4\pi)^2$  is arbitrary and has been chosen here to make the radius of the system of order unity. Regrettably this equation must be solved numerically and the resulting  $\tilde{\Psi}(r)$  is shown in Fig. 2.3.

## 2.3 Understanding the system

We have arrived at an analytically self-consistent system which should avoid the problems from §2.1. We can summarise the system by collating our results so far:

$$\begin{aligned} \rho &= 4\sqrt{2}\pi A \left( \sqrt{\Psi} - \sqrt{\Psi - \frac{L_{cut}^2}{2r^2}} \right) \\ \sigma_r^2 &= \frac{2\Psi \left[ 1 - (1-x)^{\frac{3}{2}} \right]}{9(1 - \sqrt{1-x})} \\ \beta &= \frac{\sqrt{1-x} \left( \frac{3x}{2} \right)}{1 - (1-x)^{\frac{3}{2}}} \text{ where } x = \frac{L_{cut}^2}{2r^2\Psi} \end{aligned}$$

### 2.3.1 Characterising the density profile

We first of all note that, for a particular value of  $L_{cut}$  our density profile is an augmented density profile *i.e.* our density can be expressed only in terms of  $\Psi$  and  $r$ . However, unlike the augmented density functions examined in Ciotti & Morganti (2010b) and Van Hese et al. (2011), ours is not separable in terms of those variables. This means that our model falls outside the set of models for which the GDSAI has been studied. However, our model is also highly unusual and possesses profiles that are distinctly artificial so we will spend this section characterising and explaining the model before drawing any conclusions.

The density at a given point can be thought of as the amount of orbits which require a particle to pass through that radius. As we established, our DF from Eq. 2.17 means that we are only allowing orbits with angular momentum  $0 < L^2 < L_{cut}^2$  and energy  $E = E_0$ .

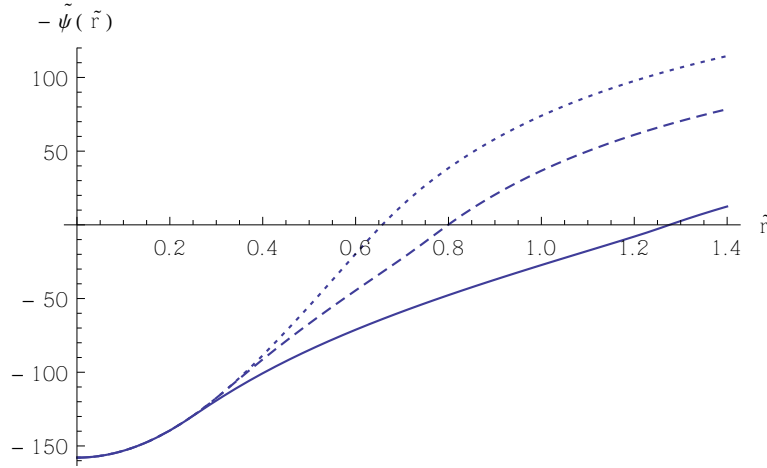


**Figure 2.3:** The numerically derived potential for our distribution function. The potential becomes positive at the point where  $\tilde{\rho} = 0$ . The potential is plotted for three models corresponding to  $\xi = \{1, 1.5, 2\}$  (see Eq. 2.37) for the solid, dashed, and dotted lines respectively. Although  $\tilde{\Psi}$  is decreasing faster than  $\tilde{r}$  in the outer regions, it will behave like a Kepler potential at radii larger than the size of the system as the system is truncated at finite radius.

It is convenient to think of the density as being *the sum of all possible, physical orbits of energy  $E_0$  minus all orbits of energy  $E_0$  and  $L^2 > L_{cut}^2$  that pass through a certain radius*. We can see this interpretation directly in Eq. 2.24 where the density is the difference between two terms which, as we will now discuss, correspond to the description above.

The first term,  $\sqrt{E_0 - \Phi}$ , represents all physical orbits of energy  $E_0$ . As we can see from Fig. 2.3, the potential of the system is a monotonically increasing function.

The second term,  $\sqrt{E_0 - \Phi - \frac{L_{cut}^2}{2r^2}}$ , is more complex due to the addition of an angular momentum term. This represents all orbits of energy  $E_0$  and an angular momentum of at least  $L_{cut}^2$ .

In Fig. 2.3, and in most subsequent figures, we plot a handful of models with different values of  $\tilde{L}_{cut}^2$  as this is key parameter which determines the behaviour of the model. The models are generated by:

$$\tilde{L}_{cut}^2 = 14.37\xi \quad (2.37)$$

where  $\xi$  is a free parameter and useful index for a particular model. The constant 14.37 was chosen to give an arbitrary but convenient value for  $\tilde{L}_{cut}^2(\xi = 1)$  and is related to

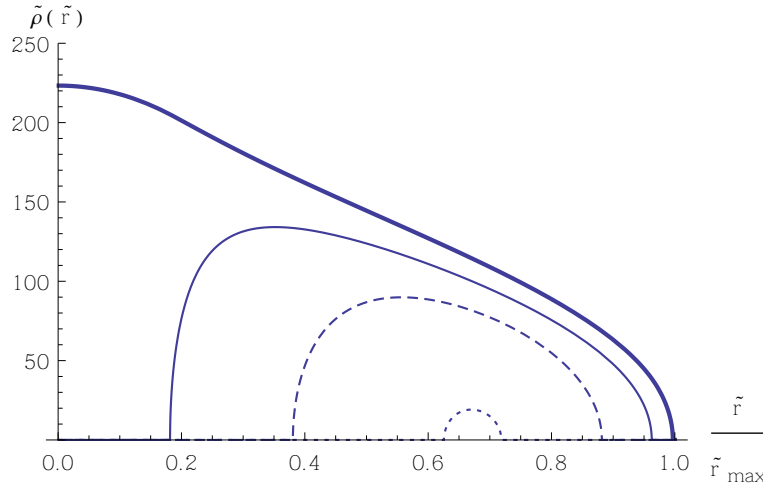


**Figure 2.4:** Both components of the density in our example model. The area under the largest curve (thick, solid line) contains all physical orbits in the system while the smaller curves (solid, dashed, and dotted) contain all allowed orbits that have  $L^2$  greater than  $L_{cut}^2$  for  $\xi = \{1, 1.5, 2\}$  (see Eq. 2.37).

$\tilde{\Psi}(\tilde{r} = 0)$ . As we can see from Fig. 2.3, increasing  $\tilde{L}_{cut}^2$  will decrease the radius of the system. To allow for better comparison of models we normalise the radius of each model to 1 in subsequent figures.

As we see from Fig. 2.4 each term in the density can itself describe a meaningful density and we have arranged them such that the number of allowed orbits is proportional to the area under the curve. The area under the largest curve contains all orbits given by  $\sqrt{E_0 - \Phi}$  and any physically permitted angular momentum. The area under the smaller curve is given by  $\sqrt{E_0 - \Phi - \frac{L_{cut}^2}{2r^2}}$  which only contains orbits with angular momentum greater than  $L_{cut}^2$  for several different values of the threshold.

We recall that our overall density is the difference between these two components which produces Fig. 2.5. The immediate feature of note is the sharp peak towards the outer edge which is the feature that makes this system so useful.

Now that we understand how this profile is formed we explain why these features arise. It must be borne in mind that this is a mono-energy system and that all orbits have total energy of exactly  $E_0$ .

At small radii, our angular momentum constraint has minimal impact. The small value of  $r$  means that even a highly tangential orbit will have an angular momentum that is

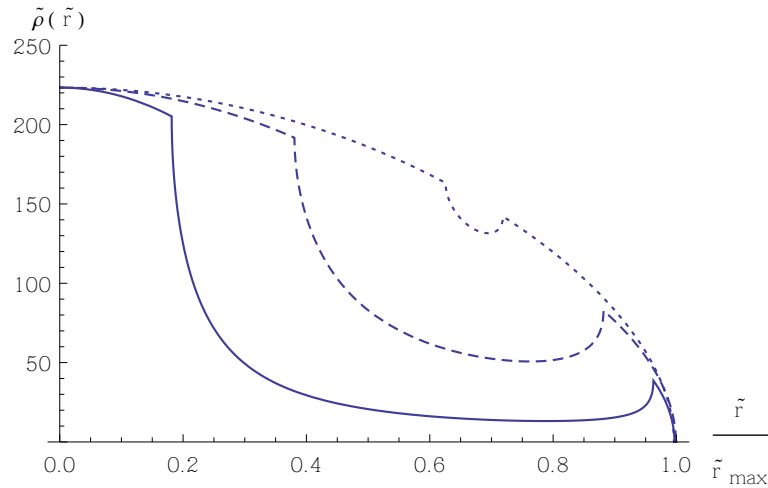


**Figure 2.5:** The full density profile for our distribution function. The density is plotted for three models corresponding to  $\xi = \{1, 1.5, 2\}$  (see Eq. 2.37) for the solid, dashed, and dotted lines respectively. Significant violation of the GDSAI is expected to occur in the sharp peak at large radii.

under the  $L_{cut}^2$  threshold. We thus find there are a large number of possible orbits and the density is high.

As we move further out an orbit of given circularity will have higher angular momentum so allowed orbits will be progressively more radially anisotropic in order to fit under the angular momentum limit. Accordingly, fewer allowed orbits exist at these radii and the density is lower than expected.

Finally, in the outermost regions the angular momentum limit no longer has any impact. Although the radius is large, the angular momentum of a highly tangential section of an orbit here is very low as the majority of a particle's energy is used to overcome the potential. This means that little is left for kinetic energy and thus the tangential velocity is extremely small. Even a completely circular orbit at this radius will have an angular momentum below the threshold. Using the same logic as for small radii this means that the density will be proportionally higher as all the possible orbits are permitted by the threshold. This can be seen in Fig. 2.6.

The last feature to understand is the sharp rise in the density at large radii. This is difficult to discuss analytically due to the lack of an analytical solution to the potential. For example, if we try to understand how angular momentum changes with radius we

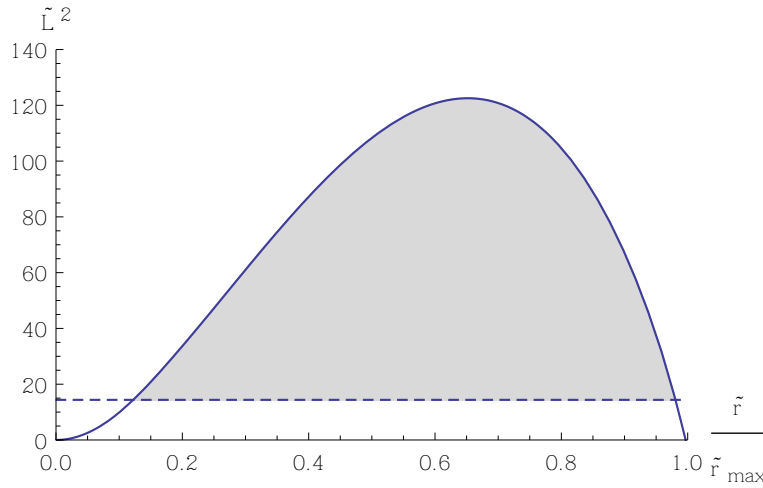


**Figure 2.6:** Variation of the maximum possible angular momentum,  $\tilde{L}_{max}^2(\tilde{r})$ , with radius showing that at large and small radii it is impossible for a particle of energy  $E_0$  to surpass the angular momentum cutoff. The cutoff  $\tilde{L}_{cut}^2(\xi = 1)$  is indicated by the horizontal line with the shaded region representing otherwise permissible orbits that will fail the angular momentum cut.  $\tilde{L}_{max}^2$  was found by using Eq. 2.38.

could look at the angular momentum of an orbit whose apocentre is at a given radius. If the particle is at its apocentre then we know that  $v_r = 0$  at that point and that the angular momentum will, from Eq. 2.20, be:

$$L_{max}^2 = 2r^2\Psi(r) \quad (2.38)$$

Since we do not know the dependence of  $\Psi$  on  $r$  we cannot construct analytical expressions for the slope. Thus, to explain the reason for the increase in density we must rely on the figures and numerical results to support the explanation.

At the point where the density rises we can see from Fig. 2.6 that  $L_{max}^2$  is decreasing rapidly. This means that, as the radius increases, a particle can eventually have an increasingly large tangential velocity at apocentre and still be under the angular momentum threshold. In other words, a particle is allowed to make a larger angle between the radial axis and its velocity vector the further it is from the centre. This also means that the amount of orbits possible at these radii, *i.e.* the density, is increasing in proportion.

In the absence of an angular momentum limit then, as seen in Fig. 2.4, the density naturally decreases monotonically as the negative potential increases towards the edge

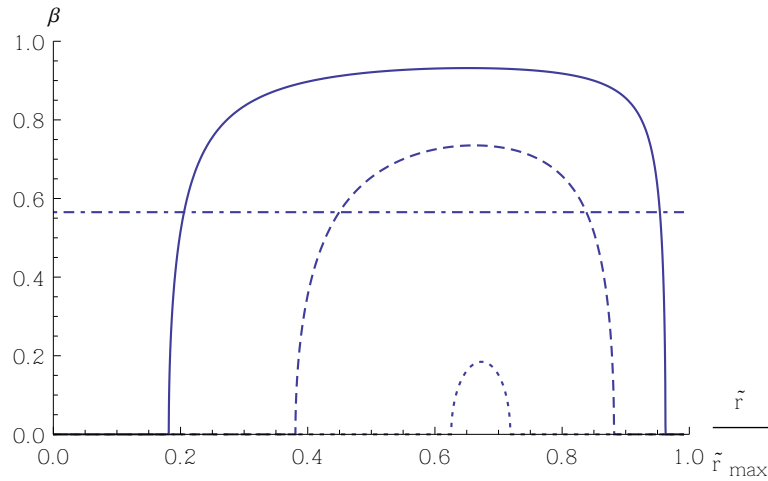


**Figure 2.7:** The anisotropy profile for our system demonstrating the isotropic core and edge regions for the three models  $\xi = \{1, 1.5, 2\}$  (the solid, dashed, and dotted curves). The dot-dashed line represents the anisotropy corresponding to the nominal radial orbit instability threshold of  $2\bar{T}_r/\bar{T}_t \approx 2.3$  (Merritt & Aguilar, 1985). This will become useful during later discussions on stability in §2.4

of the system. However, comparing these two figures shows that the rate of *decline* in phase-space density due to the potential is *lower* than the rate of *increase* due to the range of allowed angles for velocity vectors. In other words, the increase in density due to the lessening impact of  $L_{cut}$  overpowers the natural decline in phase-space density due to the potential.

This means that over a small range of radii the density actually increases until all orbits fall under the angular momentum threshold again. At this point the system has no orbits left to be added to the density as the radius increases because none are being excluded and the decline in density resumes until the edge of the system.

### 2.3.2 Characterising the anisotropy profile

One key feature of this model is that it has very low central anisotropy. The examination of Van Hese et al. (2011) proved the GDSAI held for all separable systems with  $\beta_0 \leq 1/2$  which makes an investigation into non-separable models with  $\beta_0 = 0$  of particular interest. In fact our models are isotropic at both small and large radii and only become radially anisotropic for a set of intermediate radii as shown in Fig. 2.7.

As discussed in our consideration of the density profile, the angular momentum thresh-

old removes no orbits from the core of the system or the outskirts. This is because even particles at apocentre at these radii have low angular momentum due to either the small radius of the orbit or the low tangential velocity of the particle. At these radii the angular momentum function of our DF is fixed at  $H(L_{cut}^2 - L^2) = 1$  for all orbits and thus the total DF is a function only of energy. This means that all energy is necessarily split evenly between velocity components and that region is isotropic (Binney & Tremaine, 2008).

In the regions where the angular momentum limit is removing orbits, the change in anisotropy can be thought of as follows. Imagine trying to construct a particle on an orbit that tries to maximise its angular momentum by minimising its radial velocity component, as we did when constructing Eq. 2.38. Since this orbit must have a certain amount of energy it has a very predictable angular momentum which will put the particle over the  $L_{cut}^2$  threshold. This means that this orbit, and all highly tangential ones, are removed, leaving only the more radial ones. Given that the system would be isotropic if not for this process, we can say that any radii at which the angular momentum cut removes orbits is guaranteed to be radially anisotropic.

This behaviour is shown directly by looking again at Fig. 2.6. The shaded orbits above the angular momentum threshold  $\tilde{L}_{cut}^2$  are excluded which implies that any radii at which a portion of the area under the curve is shaded will be radially anisotropic. The amount of anisotropy will grow with the size of the shaded area.

Because the transition between the isotropic regions and the anisotropic regions is a sharp one we find discontinuities in the gradient of individual velocity dispersions. Fig. 2.8 shows how the slow decrease of energy in the radial velocity component is sharply reversed upon reaching the anisotropic regions of the system. A smaller discontinuity is also present upon reaching the isotropic regions at large radii. These correspond exactly to the two discontinuities in the slope of the density profile.

### 2.3.3 The inability to extend the GDSAI to this model

We can now confirm that our system does not obey a GDSAI-like relation at certain radii. We have proved that our system is radially anisotropic in the regions where the angular momentum threshold is removing orbits. We have also demonstrated that our system's density profile is either flat or rising in those same regions due to the exclusion of a region

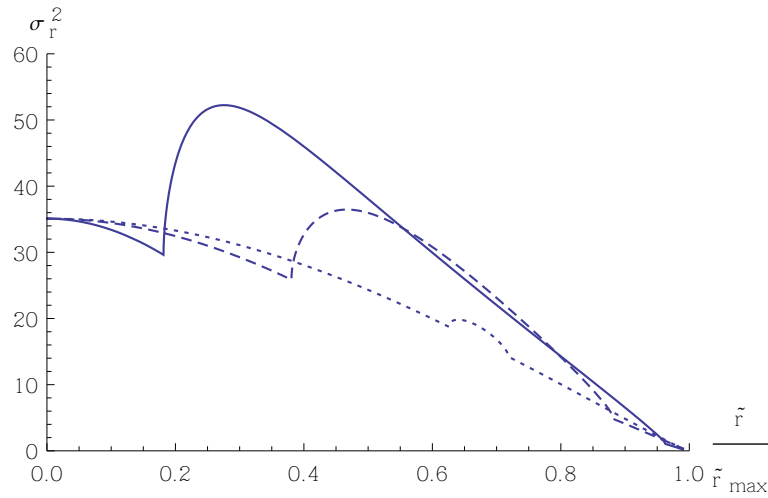


**Figure 2.8:** The radial velocity dispersion profile of our system for the three models  $\xi = \{1, 1.5, 2\}$  (the solid, dashed, and dotted curves). Upon entering or leaving regions of the model where the angular momentum cut is removing orbits there is a discontinuity as there is a abrupt decrease in the amount of energy that can be used in tangential motion.

of phase-space. From this we can see that there are two regions where we would expect to find that  $\gamma < 2\beta$  which runs counter to an attempt to extend the GDSAI.

At the radii immediately prior to the density peak we are guaranteed not to recover a relationship that follows the GDSAI as the density is *rising* sharply with radius and so  $\gamma < 0$ . However, we also fail to find the relation at a large range of intermediate radii where the density profile is approximately flat and thus  $\gamma \approx 0$ . Since the anisotropy here is high, the system can be configured such that  $\gamma < 2\beta$  at these radii as well.

The degree to which our system fails to follow the same inequality as the GDSAI and the regions in which this occurs are plotted in Fig. 2.9 where we show curves of  $\gamma$  and  $2\beta$  for the model  $\xi = 1$ . Any radius where  $\gamma < 2\beta$  demonstrates that the GDSAI could not be extended to include this model. We can see that approximately 2/3 of radii in this model display such behaviour, corresponding to 16% of the model's mass. Accordingly, we suggest that the GDSAI cannot be extended to guarantee the existence or non-existence of phase-space consistency in a non-separable DF of this kind.

Having demonstrated the theoretical interest of our system we will now discuss the stability of the equilibrium solution found for our DF.

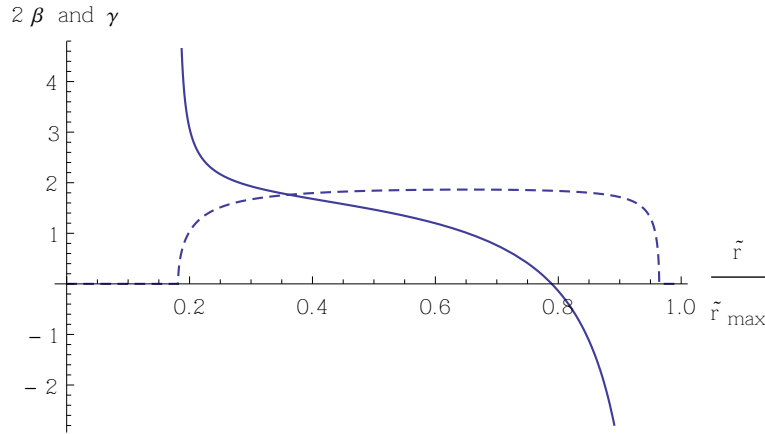


**Figure 2.9:** Showing both  $\gamma$  (solid) and  $2\beta$  (dotted) as functions of radius for the model  $\xi = 1$ . The point where the lines cross represents the beginning of the regions that fail to obey a GDSAI-like relation.

## 2.4 System stability

### 2.4.1 Radial Instability

A fundamental measure of radial stability is the anisotropic extension of the Doremus-Feix-Baumann theorem (Doremus et al., 1971, 1973; Gillon et al., 1976; Binney & Tremaine, 2008) which states that a stable system must satisfy  $df_0/dH_0 < 0$ . In other words, the equilibrium DF must be a monotonically decreasing function of the equilibrium Hamiltonian. For our DF this requires that  $df(E)/dE < 0$  which is problematic because  $f(E) = \delta(E_0 - E)$  and, due to the peculiarities of the Dirac delta, its derivative is formally undefined. However, since this is also a necessary criteria for the emergence of the Hénon Instability (Barnes et al., 1986; Merritt, 1999) we can use the Hénon criteria as an indicator of potential radial instability.

### 2.4.2 Hénon Instability

Perhaps the most similar system to ours to undergo extensive stability testing is the  $n = 1/2$  polytrope. The testing of Hénon (1973) and Barnes et al. (1986) demonstrated that the oscillatory stability of the polytrope was due a uneven radial velocity distribution that was termed the ‘Hénon Instability’. It is interesting to note that the systems of Van Hese et al. (2011) which demonstrated that the GDSAI lacked predictive power for separable systems of  $\beta_0 > 1/2$  were unstable according to the Hénon criteria.

The Hénon instability will appear in our systems if they possess two or more distinct peaks in the radial velocity distribution  $P(v_r)$  where:

$$\begin{aligned} P(v_r) &= \iint_{-\infty}^{+\infty} \delta(E - E_0) H(L_{cut}^2 - L^2) dv_\theta dv_\phi \\ &= H\left(\frac{1}{2}v_r^2 - \Psi(r) + \frac{L_{cut}^2}{2r^2}\right) - H\left(\frac{1}{2}v_r^2 - \Psi(r)\right) \end{aligned} \quad (2.39)$$

In practice, the Hénon instability can be thought of as having a region or regions in a system where material is flowing radially outwards and inwards but very little is actually staying in almost circular orbits at that radius. This means that any radially orientated perturbation can disrupt the equilibrium of these counter-balanced flows of material and cause the system to evolve. Neither of the major studies of this instability passed comment on what such systems evolve into but it would seem likely that the system would expand.

Anyway, this distribution will, after being normalised, give us a probability density that is constant over a narrow range of radial velocities:

$$P(v_r) \neq 0 \text{ where } \frac{-L_{cut}^2}{2r^2} < \frac{1}{2}v_r^2 - \Psi(r) < 0 \quad (2.40)$$

Between this and our understanding about the allowed orbits we can explain the distribution seen for a selection of radii for the model  $\xi = 1$  in Fig. 2.10.

At small radii,  $\frac{-\tilde{L}_{cut}^2}{2\tilde{r}^2} \ll 0$  so the only constraint on  $v_r$  is energy conservation. Thus we expect a range of velocities out to some maximum value.

At intermediate radii a particle is not allowed to have negligible radial velocity. If a particle here has  $v_r \approx 0$  then the mono-energy constraint would demand that it compensate with significant  $v_t$  which, at these radii, would put it over the  $\tilde{L}_{cut}^2$  threshold. Accordingly, the radial velocity distribution at these radii will be two sharp peaks with a gap around  $v_r = 0$ . The width of the peaks is determined by  $\tilde{L}_{cut}^2$  and the radius.

Finally, at the outer edge of the system the angular momentum threshold no longer removes orbits and so particles with  $v_r \approx 0$  are allowed once again. The two peaks reform into a single peak centred around  $v_r = 0$  like at small radii but with a smaller width due

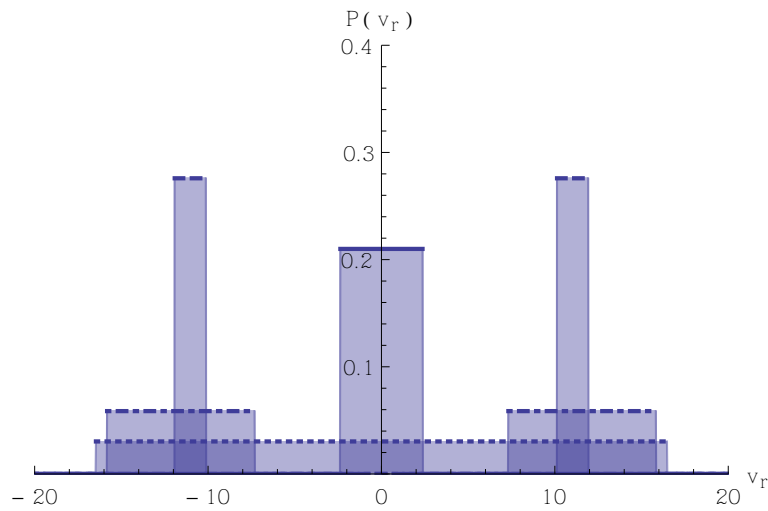


**Figure 2.10:** A probability distribution bar plot showing the normalised probability of finding a particle with a given radial velocity at certain radii. Bars topped with a dotted, dot-dashed, dashed, and solid line represent the probabilities at  $\tilde{r} = \{0.22, 0.27, 0.6, 1.25\}$  respectively.

to the smaller amount of kinetic energy available at these radii.

Since our models clearly possess two very sharp and well-defined peaks at most radii we conclude that this model may be susceptible to the Hénon instability.

### 2.4.3 Radial Orbit Instability

The stability of our system to non-radial modes is easier to assess as in the case of the radial orbit instability (ROI). ROI occurs when a system is has a large proportion of particles on highly radial orbits. Under such circumstances each particle can be thought of being a low density bar or rod that pivots around the centre of mass of the system as it precesses and has ends at the apocentres of the orbit.

If the system is subjected to a non-radial perturbation such as a small, non-uniform torque then that can accelerate the precession of some of the bars and bring them closer together. This slight over-density in the distribution of the bars will cause other bars to experience a slight gravitational acceleration towards it which will, over time, cause a runaway clustering effect. Eventually all the bars in the system will have clustered around the over-density to create a preferred, rotating axis. In short, this turns a previously uniform, smooth system into one that has developed a pronounced bar structure or, at the

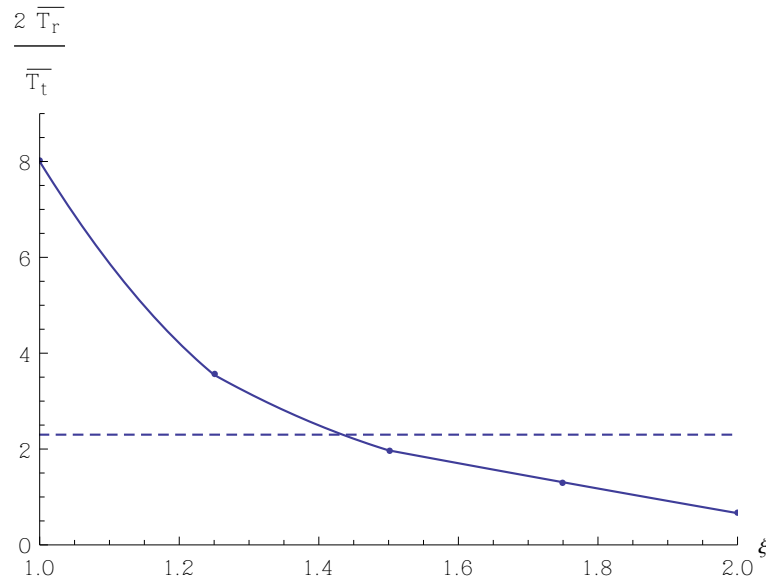


**Figure 2.11:** The dependence of  $2\bar{T}_r/\bar{T}_t$  against the  $\xi$  of the model. The radial orbit instability criteria of  $2\bar{T}_r/\bar{T}_t \approx 2.3$  is marked with a dashed line for clarity. The stability of the model depends on  $\xi$  with larger values producing more stable systems.

very least, has developed significant triaxiality.

We use a simple stability measure constructed from the ratio of kinetic energies along different axes  $2\bar{T}_r/\bar{T}_t = 2.3$  which has been the subject of much debate (Merritt, 1999). Looking back at Fig. 2.7 we see that the model  $\xi = 1$  is over the limit throughout most of the system. However, models with a higher angular momentum threshold can consistently have low enough anisotropy to avoid the instability.

This is shown in Fig. 2.11 where the radial orbit instability criteria is plotted against the angular momentum threshold. Models with  $\xi \approx 1.45$  and above appear to be stable. So, it appears that the stability of the system is a function of the parameter  $\xi$ .

#### 2.4.4 Stability dependence on $L_{cut}^2$

We have seen how our system has the potential to suffer from a variety of stability problems. However, there is reason to believe that the degree of instability can be controlled if not mitigated entirely.

We begin by once again noting that in regions where  $L_{cut}^2$  is higher than the largest possible angular momentum (see Fig. 2.6) our system behaves as if the DF is exclusively

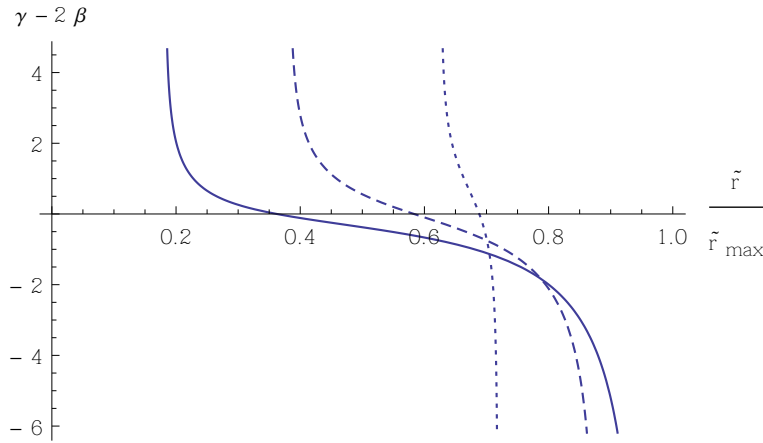


**Figure 2.12:** The GDSAI function plotted as  $\gamma - 2\beta$  for the three models  $\xi = \{1, 1.5, 2\}$  (the solid, dashed, and dotted curves). Where this function is positive the inequality is obeyed and where it is negative the inequality is not obeyed. Models with small  $\xi$  will never fail to meet the GDSAI criteria everywhere, only across a larger range of radii. In our models  $\gamma - 2\beta > 0$  is always true at  $r = 0$ .

a function of energy and is thus always isotropic. Additionally, we consider that  $L_{cut}^2$  is a tunable parameter through Eq. 2.37.

In Fig. 2.12 we can see that if we raise  $L_{cut}^2$  then it affects less of the system which, in turn, will become increasingly isotropic. Importantly, both the Hénon and radial orbit instabilities are diagnosed by considering the ratio or allowed domain of velocity components. Therefore, if our system is isotropic then it is guaranteed to be stable to both of these effects. This is what we see in Fig. 2.11.

Accordingly, it is the case that the higher  $L_{cut}^2$  is set the greater the proportion of the system that will be isotropic and the larger the volume of the system that will pass those stability criteria. This implies that *the stability of the system is exclusively dependent on the value of the freely tunable parameter  $L_{cut}^2$* . The only limits are the cases of an exactly radial system of infinitesimal density and a completely isotropic system *i.e.*  $0 < L_{cut}^2 \leq \text{Max}[L_{max}^2(r)]$ .

Thus, one can construct a system using this DF that does not obey the relation of the GDSAI to a specific degree over a specific set of radii by choosing a large enough value for  $L_{cut}^2$ . It thus follows that a system could be constructed which produces a small degree of violation over such a small range of radii that it would only be susceptible to the Hénon and radial orbit instabilities to a vanishingly small degree. It is thus true to say that the

stability implications become negligible as  $L_{cut}^2 \rightarrow \text{Max} [L_{max}^2(r)]$ .

This is particularly true for the Radial Orbit Instability criteria as the susceptibility is averaged over the entire system. Additionally, the Hénon criteria is only necessary, not sufficient, for instability (Merritt, 1999) and it is thus difficult to claim that small, highly local violations of the criteria represent chronic instability in the model.

This is seen clearly if the GDSAI function is plotted for a selection of our models. In Fig. 2.12 we can see the impact of changing  $\xi$  on our models. Regions where the function is negative indicates that system is not following the criteria of the GDSAI. In particular, we have shown that the model we have been investigating where  $\xi = 2$  is stable against radial orbit instability and also fails to follow the same criteria as the GDSAI over a range of radii. In particular, the difference at large radii is significant.

The DF of the model is positive, the majority of the system is isotropic, and the system fails to adhere to any similar relationship to the GDSAI. The only problem with the system is that its stability cannot be rigorously guaranteed. We believe that this proves that the slope-anisotropy inequality cannot be extended to include all non-separable systems in addition to its current areas of success. We obviously cannot speak specifically for each and every non-separable model, but we can demonstrate that DFs of this form with non-trivial values for  $L_{cut}$  do not obey such a relationship. We find that stability criteria are the principle measure of the success of our system and correlate to regions of the system which fail to obey a GDSAI-like relation.

This dependence extends to the observables of the system. For example, by integrating the velocity distribution from Eq. 2.4.2 over radius we can find the line-of-sight velocity distribution (LOSVD) for a line-of-sight passing through the centre of the system.

In Fig. 2.13 we plot the LOSVD for a variety of models. In most cases the double peak structure is very clearly seen although it diminishes in strength as  $L_{cut}^2$  rises. This is because, as discussed earlier, the double peak only appears at certain radii depending on the value of  $L_{cut}^2$ . For large values of  $L_{cut}^2$  the double peak will only appear at a very small range of radii and will be insignificant compared to the isotropy at other radii. Consequently, when integrated over the line-of-sight, the feature is lost and the system appears single peaked.

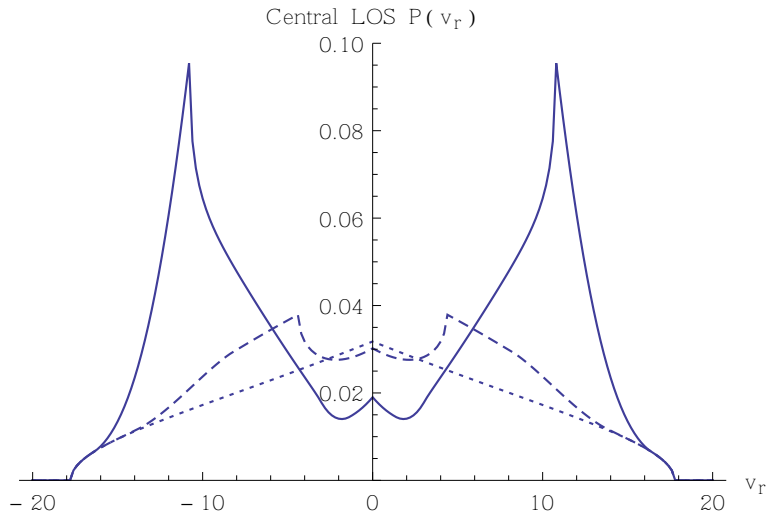


**Figure 2.13:** The LOSVD through the centre of our system is plotted for three models corresponding to  $\xi = \{1, 1.5, 2\}$  for the solid, dashed, and dotted lines respectively. The double peak feature is retained in the majority of models although is not apparent in models with a high  $L_{cut}^2$ . In such models the double peak appears only at a very small range of radii and is not significant enough to stand out against the background.

## 2.5 Generalising the model

We now aim to generalise our DF so as to examine a wider variety of non-separable systems. Additionally we would like to identify a non-separable system that does not follow a GDSAI-like relation whilst also retaining the quality of dynamical stability.

The problems with instability cannot be resolved by using a mono-energy DF. Remember that we established that our systems do not obey anything similar to the GDSAI by excluding high angular momentum orbits to create a density plateau and radial anisotropy. Given that is the case we can generally describe our DF as a mono-energy halo of energy  $E_1$ :

$$f(E, L) = \delta(E_1 - E)F(L^2) \quad (2.41)$$

where we require that  $F(L^2)$  decreases as  $L^2$  rises which is how we specify that the model will favour low angular momentum orbits. We can then use this DF to find a general expression for the probability distribution of radial velocities as required for an analysis of the Hénon instability (see §2.4.2):

$$P(v_r, r) = 2\pi \int \delta \left( E_1 - \Phi(r) - \frac{v_r^2}{2} - \frac{v_t^2}{2} \right) F(v_t^2 r^2) d \left( \frac{v_t^2}{2} \right) \quad (2.42)$$

This then gives a general solution:

$$\begin{aligned} P(v_r, r) &= F(v_t^2 r^2) \Big|_{\frac{v_t^2}{2} = E_1 - \Phi(r) - \frac{v_r^2}{2}} \\ &= F \left( (2E_1 - 2\Phi - v_r^2) r^2 \right) \end{aligned} \quad (2.43)$$

Now, we specified that  $F(L^2)$  is a function which decreases as its argument increases. This means that for a fixed radius  $r$ ,  $F \left( (2E_1 - 2\Phi - v_r^2) r^2 \right)$  is an increasing function of  $v_r$ . This has the unfortunate implication that  $F(L^2)|_{v_r=0} < F(L^2)|_{v_r>0}$ .

In other words the velocity distribution will always have a trough at  $v_r = 0$  and two peaks at  $v_r = \pm\sqrt{2E_1 - 2\Phi}$  meaning the Hénon instability is always going to cause problems for models of this kind.

To try and avoid this we must generalise the model further by weakening the condition that it is mono-energy. Our generalised DF is of the form:

$$f(E, L) = [H(E - E_1) - H(E - E_2)] H(L_{cut}^2 - L^2) g(E) \quad (2.44)$$

where  $g(E)$  is a function of energy which we assume, for illustrative purposes, is given by  $g(E) = e^{-bE}$ . We define  $E_1 < E_2 \leq 0$  as constant values for energy. With this DF we allow orbits in the system that have angular momentum  $L^2 < L_{cut}^2$ , energies of  $E_1 < E < E_2$  and the function  $g(E)$  is left free. We can see that the DF of Eq. 2.17 can be approximated by the special cases where  $E_1 \rightarrow E_2$  and  $g(E)$  is constant.

The corresponding density function for this illustrative model is:

$$\begin{aligned} \rho &= \left\{ 4\pi\sqrt{2}b^{-1.5} \right. \\ &\quad \left[ e^{-b\Phi} [\Gamma(1.5, b(E_1 - \Phi)) - \Gamma(1.5, b(E_2 - \Phi))] \right. \\ &\quad \left. \left. - e^{-b\phi} [\Gamma(1.5, b(E_1 - \phi)) - \Gamma(1.5, b(E_2 - \phi))] \right] \right\} \end{aligned} \quad (2.45)$$

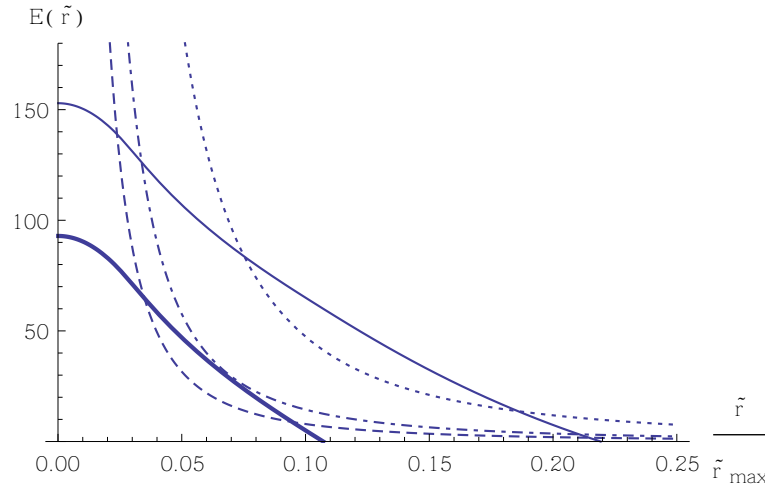


**Figure 2.14:** Plots of important energies for a particular case of the illustrative model of Eq. 2.45 where  $E_1 = -70$ ,  $E_2 = -10$ ,  $b = 0.0005$ , and  $\tilde{\Psi}(\tilde{r} = 0) = (4\pi)^2$ . The solid and thicker solid curves are  $E_1 - \Phi$  and  $E_2 - \Phi$ . Other curves are  $L_{cut}^2/2r^2$  for different values of  $L_{cut}^2$ . The dashed line is for a harsh cut of  $L_{cut}^2 = 0.012566$ . The dot-dashed line is  $L_{cut}^2 = 0.022934$  which only touches  $E_1 - \Phi$ . The dotted curve is  $L_{cut}^2 = 0.075398$  which only excludes a very small amount of orbits.

where  $\phi = \Phi + \frac{L_{cut}^2}{2r^2}$ ,  $b$  is a constant, and  $\Gamma(a, x)$  is the incomplete Gamma function which is defined as  $\Gamma(a, x) = \int_x^\infty t^{a-1} e^{-t} dt$ .

The corresponding potential is numerically derived and the other system characteristics are computed using the same methods as in §2.2. The analytical formulae are not given here as they are prohibitively large and the model is only for illustration.

This generalised DF is non-separable and still demonstrates behaviour that is not in agreement with an extended GDSAI. For example, recall how in the density peak of Fig. 2.5 we had a transition domain where  $\gamma \ll 0$  while the anisotropy profile was making a transition from strongly radial anisotropy to isotropy as was discussed in detail in §2.3.

This behaviour remains unchanged in the generalised DF as the angular momentum limit can be set so that it removes *all* particles whose orbits are highly tangential at intermediate radii, making the system under-dense and anisotropic. Again, since this cut *only* removes highly tangential orbits it can *only* make the system more radially anisotropic at these radii. Thus the failure to obey a relation similar to the GDSAI is still seen in our generalised system in the region where the density peak is produced as the system moves out of the under-dense domain and towards isotropy.

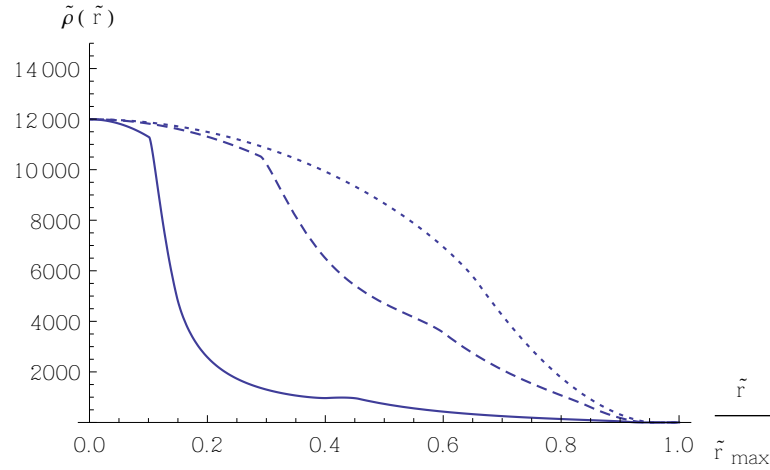


**Figure 2.15:** The density models of the systems in Fig. 2.14. The systems are all  $E_1 = -70$ ,  $E_2 = -10$ ,  $b = 0.0005$ , and  $\tilde{\Psi}(\tilde{r} = 0) = (4\pi)^2$  where the solid line is  $L_{cut}^2 = 0.012566$ , the dashed line is  $L_{cut}^2 = 0.022934$ , and the dotted curve is  $L_{cut}^2 = 0.075398$ . Note the bump at intermediate radii rather than the sharp peaks seen in previous models as well as the difficulty in getting a positive gradient.

Accordingly, behaviour different to that described by the GDSAI in this region can be caused by simply setting  $L_{cut}^2 \leq 2R^2(E_1 - \Phi)$  where  $R$  is some chosen intermediate radius at which the angular momentum of a completely tangentially moving particle in the system is maximised. This causes the angular momentum cut to exclude all orbits which are highly tangential around this radius down to the ones of lowest allowed energy as shown in Fig. 2.14. Note that, as demonstrated in Fig. 2.12, the difference from the GDSAI will actually begin at smaller radii due to the gradual flattening of the density profile occurring alongside the rise in anisotropy. However, the exact point at which this takes place will be very model dependent.

The problem remains that, as discussed in §2.4.2, removing all highly tangential particles implies that  $P(v_r \approx 0) = 0$  which leads to the sharply double-peaked velocity distributions that are indicative of the Hénon instability. So, if we set a harsh angular momentum limit then we can remove a large amount of tangential energy and create our peak and anisotropy which will not follow the GDSAI at the cost of stability. Conversely, if we remove the limit entirely then the system becomes isotropic and smooth but fails to produce any interesting behaviour relating to the inequality. However, while these were the only options for the original DF, the new DF allows intermediate cases which can give us some

insight as shown in Figs. 2.15 and 2.14.

We examine the case where  $L_{cut}^2 = 2r^2(E_1 - \Phi)$  has a single solution compared to the usual two as shown in Fig. 2.14. In this instance the angular momentum limit only excludes orbits down to the orbit of lowest energy which has the highest angular momentum. In other words, if the limit was raised infinitesimally then it would just be possible to have an orbit with kinetic energy of exactly  $E_1 - \Phi(R)$  whose apocentre was at a radius  $R$  which maximised that orbit's angular momentum.

What we see in Fig. 2.15 is that already the model is not excluding enough orbits to force a local  $\gamma < 0$ , which is the feature in our models which always guarantees behaviour that can demonstrate disagreement with a GDSAI-like relation. This is not encouraging as this the earliest case where  $P(v_r = 0) \neq 0$  for all energies which means that that this case is still significantly unstable by the Hénon criteria because  $P(v_r = 0) \ll P(v_r > 0)$ . However, it is *already* unlikely to produce behaviour different to the GDSAI due to  $\gamma > 0$  and an anisotropy that will not be as high as in models with harsher angular momentum cuts.

This is true of every model where  $2r^2(E_1 - \Phi) \ll L_{cut}^2 < 2r^2(E_2 - \Phi)$ . As the number of high angular momentum orbits allowed increases, it follows that  $\gamma$  must rise,  $\beta$  must tend towards 0, and  $P(v_r = 0)$  will also rise. However the probability of very low  $v_r$  *will still be reduced compared to a system where no orbits are removed*. In other words, the instability will be present to some degree over some range of radii if the angular momentum threshold excludes any orbits at all.

Between these cases we see that the behaviour of our generalised model is comparable to that of our simpler, more specific DF. Depending on the choice of parameters the system can demonstrate behaviour over a range of radii that is in disagreement with a potential extension of the GDSAI, however causing such behaviour decreases the chance of finding particles with low  $v_r$ . Cutting a large amount of orbits can guarantee this behaviour at the cost of severe instabilities where  $P(v_r \approx 0) = 0$ , while weaker cuts causes milder instability where  $P(v_r \approx 0) \neq 0$  and may fail to demonstrate inconsistency with an extended GDSAI.

This line of reasoning leads us to the conclusion that while any suitable combination of parameters can create systems that do not follow a GDSAI-like relationship the mechanism

of removing high angular momentum orbits is never going to produce a model that passes the Hénon criteria.

## 2.6 Summary

We have managed to construct a non-separable, equilibrium system with  $\beta_0 < 1/2$  using a globally positive DF which demonstrates behaviours inconsistent with an application of the GDSAI. The magnitude of the departure from the GDSAI is dependent on the value of the angular momentum threshold  $L_{cut}^2$ , which is also the parameter that controls the stability of the model. It is possible to pick values of this parameter where the majority of the system fails to agree with an extension of the GDSAI but is also unstable, or where the failure is highly local and the instability is negligible. This is a significant expansion on previous work proving the efficacy of the GDSAI in separable systems (Ciotti & Morganti, 2010b; Van Hese et al., 2011) and is suggestive that the GDSAI may not be applicable to models with non-separable augmented densities.

We conclude this shows that whether or not a non-separable system obeys the GDSAI does not constitute proof of the positivity or otherwise of the system's DF. We do, however, note that there is a non-trivial relationship between disagreement with an extended GDSAI and the stability of the system. We suggest that GDSAI may not imply phase-space consistency in such systems but may be able to make some predictions of model stability.

Exploring generalisations of the simple system have shown that this approach will not be able to yield a system that is stable under the Hénon criteria. Future work will therefore focus on mechanisms beyond the removal of high angular momentum orbits. In conclusion, we feel that while the GDSAI remains a useful guide for non-separable systems, it should not be considered a definitive criterion in discussions of DF positivity in such systems.



# 3

## The motivation for a new gravity

*“The more important fundamental laws and facts of physical science have all been discovered, and these are now so firmly established that the possibility of their ever being supplanted in consequence of new discoveries is exceedingly remote.”*

— *Albert A. Michelson*

Despite the extraordinary success of the Newton/Einstein paradigm in the solar system, serious problems were uncovered with the advent of detailed measurements of cosmological and galactic behaviour. Over the next few sections we'll examine some of these issues and have a look at some of the solutions that have been proposed. The problems can be broadly split into two big groups: dark matter on the galactic scale and dark energy on the cosmological scale.

### 3.1 Dark matter

The existence of dark matter is one of the older problems with our understanding of gravity and it has taken a long time for the scale of the problem to be well understood. Dark matter is a generic term for the systematic mismatch between the amount of luminous matter observed in galactic-scale structures and the gravitational potential required to make them dynamically stable. Specifically, using Doppler measurements it is possible to plot how the circular speed of a structure varies with distance from the centre of mass which reveals material at the outer edges is moving sufficiently quickly that it should no longer be gravitationally bound.

The original discovery of this problem was made in the 1930s by Fritz Zwicky. In Zwicky (1933) he noted that the kinematics of the Coma cluster were inconsistent with observations of the luminous material but not too much was made of this as the missing material was thought to be awaiting discovery in as-yet unexplored regions of the electromagnetic spectrum. The problem rested for a while, resurfacing in papers such as Ostriker et al. (1974) as cosmological parameters became more precisely known, but it was not until the past couple of decades that the problem became a matter for serious concern.

Not only had the missing material failed to turn up, but the problem had spread to almost every large scale structure that was examined. The underprediction of mass-to-light ratios (Flynn et al., 2006) and the problems with velocity profiles (Salucci et al., 2007) remained, but were now joined by a host of other problems. Non-luminous matter was now required by virial analyses (Lokas & Mamon, 2003) and X-ray emission studies (Lewis et al., 2002; Horne, 2006) of galactic clusters including the Local Group (Chernin et al., 2009), the kinematics of merging galaxies (Clowe et al., 2006), and in cosmological lensing studies of structure at the largest scales (Massey et al., 2007; Parker et al., 2007; Scoville et al., 2007). Dark matter had even been found in the power spectrum of the microwave background (Komatsu et al., 2009) and it had been suggested that it was in fact impossible to build structures of any kind in a universe consisting only of known species of baryonic matter (Roos, 2010).

One suggestion is that the laws of gravity simply do not behave the way we would expect at the acceleration scales relevant for galactic dynamics. In this framework, the discrepancy is simply a systematic error caused by using Newtonian gravitational laws to

describe a domain in which they do not strictly apply. The solution, known as ‘MODified Newtonian Dynamics’ or ‘MOND’, involves adding an extra, acceleration-dependant factor to the coupling between gravity and matter. This attempt to rewrite one of the fundamental forces has drawn criticism, however, and currently is seen as the minority view. We shall discuss it in more detail later in this chapter.

By far the most popular solution is to invoke a new species of non-baryonic, weakly interacting, collisionless matter which populates a large, isotropic halo inside of which a galaxy sits like the thread of colour inside a marble. This solution is probably the simplest as it makes only a comparatively small adjustment to the current paradigm, especially since a variety of hypothetical particles are known which could fill the role. This, however, is not the main focus of the thesis and so a detailed discussion of axions, neutralinos, and all the other myriad of options is not going to appear here.

What does bear mentioning is that the road towards a consistent description of dark matter is not a smooth one. Dark matter has a variety of problems such as its failure to reproduce the Tully-Fisher and Fundamental Plane relations (McGaugh & De Blok, 1998; Gnedin et al., 2007; Spekkens et al., 2008; Dutton et al., 2010), the observation of cored, isothermal halos rather than cuspy, two-power law ones (Moore et al., 1999; De Blok & Bosma, 2002; Gentile et al., 2004; Kamionkowski, 2007), and its failure to produce simulations of cosmological structure formation in agreement with observation (Kauffmann et al., 1993; Spergel & Steinhardt, 2000; Kamionkowski, 2007; González et al., 2009).

Nonetheless, these problems are seen as comparatively minor next to the problems caused by completely altering the structure of the laws of gravity. Altogether this dark matter-based cosmology came to be called ‘ $\Lambda$ CDM’ where ‘CDM’ stands for ‘cold dark matter’ and the ‘ $\Lambda$ ’ refers to the cosmological constant. Speaking of which . . .

## 3.2 Dark energy

Arguably the biggest failure – certainly by order of magnitude – of the current cosmological paradigm is the effort to explain the observed acceleration in the expansion of the universe. Evidence for the acceleration first came to light from a variety of sources but was initially only suspected from calculations suggesting that the universe would be too dense to form stars without an accelerating expansion (Peebles & Ratra, 2003).

It was not until the late 90s that redshift measurements of type Ia supernovae provided direct observational support for an accelerating expansion (Riess et al., 1998; Perlmutter et al., 1998, 1999; Efstathiou et al., 1999) along with high resolution measurements of the microwave background demonstrating that the universe was likely flat (Kamionkowski et al., 1994; De Bernardis et al., 2000) and with a non-zero cosmological constant (Klapdor & Grotz, 1986; Zehavi & Dekel, 1999; Caldwell & Kamionkowski, 2009). The effect was also found to be directly observable at the galactic cluster scale when conducting detailed virial analyses (Chernin et al., 2009).

Originally added to counterbalance the inevitable gravitational collapse of an infinite, static universe (Binney & Tremaine, 2008), the cosmological constant was brought into modern cosmology as a placeholder for an apparent pressure associated with the vacuum which causes the expansion of spacetime to accelerate. The trouble with the current model of this pressure – where it is caused by quantum vacuum fluctuations granting the vacuum a non-zero energy – is the fact that it overpredicts the observed value of this pressure,  $\sim 10^{-47}\text{GeV}^4$ , by around 120 orders of magnitude,  $\sim 10^{71}\text{GeV}^4$  (Weinberg, 1989).

There are various methods by which the problem may be fixed ranging from the application of string theory to non-standard cosmologies where our vantage point is not representative (Sarkar, 2008) to the addition of new fields and particles. However, this ties back in to one of the main arguments in favour of the modification of gravity as opposed to the other options, namely that of simplicity. While alternatives require the invocation of new hypothetical fields (Armendariz-Picon et al., 2000; Cai et al., 2010) and dimensions (Wang et al., 2004), it is arguably logically favourable to require none of these. Instead, by making alterations only to our current theory of gravity we may allow dark energy effects to arise naturally in such a manner as the attempts of Carroll et al. (2004).

A complete analysis of the successes and failures of all the proposed solutions to the dark energy problem is, again, beyond the scope of this thesis and I would recommend the excellent review of Copeland et al. (2006) if one wishes to know more. However, there is one idea in particular that I wish to draw attention to. There have been a surprising number of publications in recent years that have brought up idea of using the anthropic principle to explain the value of the cosmological constant (Weinberg, 1987; Efstathiou, 1995; Hogan, 2000; Kallosh & Linde, 2003; Huang & Li, 2005; Wang & Yang, 2008; Shaw

& Barrow, 2011). Certainly the anthropic principle can supply *some* limits on the constant's value as most of these papers aim to narrow down the vacuum energies prescribed in the  $10^{500}$  solutions of string theory to ones not actively hostile to the formation of matter.

The problem arises when one tries to determine what limits the creation of 'observers' as there is an understandable temptation to limit that definition to only human-like and otherwise familiar forms of life. Equally, the more open minded one becomes about the conditions required for 'observers', the broader and less useful the accompanying prediction of the cosmological constant becomes. As arguments about the utility of the anthropic principle as a scientific tool border on philosophy I shall close with a quote which I feel phrases the issue rather neatly.

[On performing a proper analysis on  $10^{500}$  vacuum solutions]

“... And even if we succeeded in this herculean task we would be left with the conclusion that the detailed numerical values of low energy parameters were a statistical accident with no hope of scientific explanation. It is a very bleak picture of the future of physics.”

— Banks et al. (2001)

### **3.3 Breakdowns of the current theory**

Aside from these observational problems there are also a few stand-alone points of interest where current theories of gravity break down. The first is a variety of instances where strong gravitational fields create singularities. While this is a well-documented feature and these singularities are usually interpreted physically as 'black holes' it should be remembered that singularities in a field are more usually associated with a failure of the theory.

One possible route towards removing singularities from strong gravitational fields and the potentials of point masses is the application of quantum field theory (QFT). QFT has proved itself useful in generating powerful and consistent theories for electromagnetic fields, but extending QFT to produce a theory of gravity has proved very difficult. One of the major difficulties is that there is no quantum theory that can describe Einsteinian gravity while also being renormalisable 'on the mass shell' (DeWitt, 1967; Deo et al., 2009;

Sotiriou & Faraoni, 2010; Lu & Pope, 2011). We will take a minute to explain what that means.

Remember that relativity is based around a set of terms called ‘invariants’ which are measured quantities that the theory conserves independently of the frame in which the measurements are made. For example, the invariant mass is one of the more useful ones for particle physics as it describes the allowed region of a free particle in energy-momentum space:

$$E^2 - p^2c^2 = m^2c^4 \quad (3.1)$$

which describes a hyperbola known as the ‘mass shell’. Particles that are on the hyperbola will conserve the invariant mass and are said to be ‘on the mass shell’. These ‘on-shell’ states correspond to real particle states and can be described comparatively easily. The problem comes when trying to describe states which do not conserve the invariant mass and are thus ‘off the mass shell’. Such states are not real particles but are still important as they describe possible states for the virtual particles that transmit forces in a QFT.

QFT is based around solving path integrals over every possible route that particles can take between initial and final states, including the routes available to populations of virtual particles. The problem is that virtual particles have an infinity of possible states and so trying to solve a QFT to describe gravity produces integrals which are divergent. A technique known as renormalisation can cancel out unwanted infinities under certain circumstances however no way of successfully applying this to gravity is known.

### 3.4 Modifications to Newtonian dynamics

One solution to all the problems outlined above is to find a way to alter the equations of gravity so that the new problems are resolved while the old, established results are left intact. There are a wealth of theories available ranging from those that resurrect the aether (Zlosnik et al., 2007) to adding higher order terms into general relativity, an approach known as  $f(R)$  gravity (Capozziello, 2002; Capozziello et al., 2006; Sotiriou & Faraoni, 2010). In the next couple of sections we will concentrate on one method in particular.

The first reasonably successful attempt at this was an empirical theory developed in Milgrom (1983) which modifies Newtonian gravity by adding an acceleration threshold,  $a_0$ , below which the Poisson equation is augmented by a factor:

$$\mu\left(\frac{|\vec{a}|}{a_0}\right)\vec{a} = -\nabla\Phi_N \quad (3.2)$$

Unfortunately this form of MOND has several significant shortcomings, such as its failure to obey conservation laws (Romero, 2006), which stem from its empirical derivation. This means that the theory is unusable as anything more than a toy model. In order to build conservation laws into the foundation of the theory attempts were made to reformulate the basic MOND idea using a more formalised, Lagrangian approach. This produced a theory called AQUAL (Bekenstein & Milgrom, 1984):

$$\nabla \cdot \left[ \mu\left(\frac{|\nabla\phi(r)|}{a_0}\right) \nabla\phi(r) \right] = 4\pi G\rho(r); \quad a_0 \approx 1.2 \times 10^{-10} \text{ m s}^{-2} \quad (3.3)$$

where  $\mu(x)$  is some function describing what happens to gravity in the MONDian regime. The function  $\mu(x)$  is what dictates the strength of the MONDian modification to the straightforward Newtonian case. There are a variety of different functions that can be used, but all have the same simple, monotonic power-law description that is not determined *a priori* by theory and the same asymptotic behaviour. A standard, simple form is:

$$\mu(x) = \frac{x}{1+x} \rightarrow \begin{cases} x & x \ll 1 \\ 1 & x \gg 1 \end{cases} \quad (3.4)$$

From this we see that in the limit of a strong gravitational field the MOND effect is purely perturbative (Bekenstein & Magueijo, 2006) and the system behaves in a Newtonian manner. We also have what we shall call the ‘deep MOND’ or ‘weak field’ regime where  $|\nabla\Phi| \ll a_0$  (Zhao, 2005) and MOND effects dominate. This can be used to generate acceleration profiles by relating the Newtonian acceleration to the MONDian acceleration:

$$\frac{g_N}{g} = \mu\left(\frac{g}{a_0}\right) \text{ therefore } \frac{g}{g_N} = \frac{1}{\mu\left(\frac{g}{a_0}\right)} = \nu\left(\frac{g_N}{a_0}\right) = \frac{1}{2} + \sqrt{\frac{1}{4} + \frac{a_0}{g_N}} \quad (3.5)$$

Thus, any Newtonian acceleration profile can be related to a MONDian one through  $g = g_N \nu(y)$  where  $\nu$  is defined as above. In the case of the deep MOND systems this simple relationship is not detailed enough and the relationship between density and potential is found by solving the Poisson equation as we have done before in chapter 1:

$$\nabla \cdot [|\nabla\phi|\nabla\phi] = 4\pi G a_0 \rho(r) \quad (3.6)$$

$$\nabla\phi = \sqrt{\frac{GM(< r)a_0}{r^2}} \quad (3.7)$$

Theories to come from this approach include BIMOND (Milgrom, 2009) and its extension QMOND (Milgrom, 2010b). Both theories are so-called ‘bi-metric’ theories which posit another spacetime metric with its own forces and matter components that is coupled to our more familiar one (Milgrom, 2010a). These new theories are quite young and have not been studied very extensively but they are not without their problems.

BIMOND type theories do show successes in fitting rotation curves in so far as they reproduce the simple MOND behaviour that has already found considerable success (Beegman et al., 1991; Sanders & McGaugh, 2002; McGaugh, 2011). However, they now invoke a new metric as well as a new species of matter to couple to it, arguably invalidating a significant point in favour of MOND type approaches, namely their simplicity.

We will continue to look at some of the relativistic modifications to MOND later on, but for now we will try and apply some of the non-relativistic methods and theories that we have discussed.

### 3.5 The difficulties of working in MOND

While Eq. 3.3 may not seem like a significant alteration from Poisson’s equation, the problems of working in MOND can be demonstrated by attempting to solve the following problem in galactic dynamics while generalising to allow for MOND effects.

The derivative  $dM/dE$  represents the amount of mass that occupies a given infinitesimal energy range in a system, in this case the system under consideration is the distribution of stars in a galaxy. Since a real galaxy has a finite bound mass the distribution

of particles will have an abrupt cut-off at the escape energy of the system. However, this cut-off was decided *a posteriori* after the galaxy formed via gravitational collapse.

Before the material condensed into a galaxy it is reasonable to assume that the primordial distribution of particle energies was smooth and continuous. Eventually the galaxy reached an equilibrium and the binding potential became fixed but the distribution of particle energies should still be smooth and should extend past this cut-off as some particles will be unbound. The problem is that many models give the energy gradient at this point as  $dM/dE = 0$  which is rather suspicious as it implies that the primordial function  $M(E)$  flattened off at exactly the point where the future binding energy would be. If there is no link between the local shape of  $M(E)$  and the equilibrium potential then you would not expect this to be true.

We can investigate this behaviour in the two power models we met back at the start of chapter 1 as they have the flattening behaviour needed and are widely used. In order to examine the problem analytically we need to define a quantity called the density of states. The density of states, or  $g(E)$ , describes the volume of the phase-space that occupies a particular energy. Accordingly, the mass of stars of a given binding energy is the product of the volume of phase-space occupying a given energy state and the mass occupying a given phase-space volume given as a function of energy. In other words we can write:

$$\frac{dM}{dE} = g(E)f(E) \quad (3.8)$$

where  $g(E)$  is the density of states and  $f(E)$  is the distribution function in terms of energy.

Let's begin by clarifying some of our terms. We will be dealing in energies and potentials in a system with a single-valued radial potential relative to some background potential  $\Phi_0$ . Much of this description is very similar to that from the first chapter so we shall not spend too long retreading familiar ground. We define the fundamental parameters of the system as follows:

$$H = \frac{1}{2}v^2 + \Phi(\mathbf{x}); E = H + \Phi_0 = \Phi - \frac{1}{2}\mathbf{v}^2 \quad (3.9)$$

First we find the density of states which is given by (Binney & Tremaine, 2008):

$$g(E) = \int \delta(H - E) d^3\mathbf{x} d^3\mathbf{v} \quad (3.10)$$

This integral is then evaluated over both ranges up to some value  $E$  or rather the radius and velocity that correspond to  $E$ . The second integral, being a delta function, can only be evaluated at the point where  $E = \Phi$ . This means that the integral is now:

$$g(E) = (4\pi)^2 \int_0^{r(\Phi=E)} r^2 \sqrt{2(E - \Phi)} dr \quad (3.11)$$

To solve this we need to make another change of variable. Currently, we are integrating between the centre of the system and a radius at which  $\Phi = E$ . We can express this instead in terms of another parameter we shall call  $X$  which we derive from the Hernquist potential:

$$r = \frac{-GM}{\Phi} - a; \text{ let } X \text{ be } \frac{-GM}{a\Phi} \rightarrow r(\Phi = E) = \frac{-GM}{E} - a = aX - a \quad (3.12)$$

Substituting in  $r = aX - a$  gives us the integral we will be evaluating:

$$g(E) = (4\pi)^2 a^3 \sqrt{2E} \int_1^A (X - 1)^2 \sqrt{\left(\frac{A}{X} - 1\right)} dX \quad (3.13)$$

where:

$$A = \frac{GM}{a|E|} \quad (3.14)$$

Finally, this solves to give us our density of states:

$$g(E) = (4\pi)^2 a^3 \sqrt{2E} \left[ \sqrt{A - 1} \left( \frac{A^2}{8} - \frac{5A}{12} - \frac{1}{3} \right) + \frac{A}{8} (A^2 - 4A + 8) \cos^{-1} \left( \frac{1}{\sqrt{A}} \right) \right] \quad (3.15)$$

For the DF we can use the result from Hernquist (1990) to state that  $f(E)$  can be written using the Abel integrals from chapter 1:

$$f(E) = \frac{1}{\sqrt{8\pi^2}} \int_0^E \frac{d\Psi}{\sqrt{E-\Psi}} \frac{d^2\nu}{d\Psi^2} + \frac{1}{\sqrt{E}} \frac{d\nu}{d\Psi} \Big|_{\Psi=0} \quad (3.16)$$

where it should be noted that we are using  $\nu$  here to refer to the particle probability density not the inverse MOND  $\mu$  function.

At this point we need to know  $\nu(\Psi)$  which depends on the type of gravity being assumed. We shall come back to this point in a moment. We can now combine Eqs. 3.15 and 3.16 to state that what we are trying to solve is:

$$\frac{dM}{d\mathcal{E}} \Big|_{\mathcal{E}=0} = \sqrt{2} \left[ \int_0^{r(\Psi=\mathcal{E})} r^2 \sqrt{2(\Psi-\mathcal{E})} dr \right] \times \left[ \int_0^{\mathcal{E}} \frac{d\Psi}{\sqrt{\mathcal{E}-\Psi}} \frac{d^2\nu}{d\Psi^2} + \frac{1}{\sqrt{\mathcal{E}}} \frac{d\nu}{d\Psi} \Big|_{\Psi=0} \right] \neq 0 \quad (3.17)$$

where we find it convenient to treat each integral as a separate entity and simply require each to be non-zero. Additionally, it is also convenient to write this in terms of the relative energy and relative potentials for similarity to the work of chapter 1. In order to evaluate these two integrals we need to know  $\Psi(r)$  and  $\rho(\Psi)$  making this a good example of another instance where model families with well-known potential-density pairs are important.

We wish to solve this in a very generalised context as we would like our solution to be independent of assumptions about MOND or dark matter and so we will use a more flexible definition of MOND than Eq. 3.3 and allow an extra degree of freedom in the system,  $n$ , as follows:

$$\nabla^2\Phi(r) \rightarrow \nabla \cdot (\mu \nabla\Phi(r)) = \nabla \cdot \frac{(\nabla\Phi(r))^{n+1}}{(a_0)^n} = 4\pi G\rho(r) \quad (3.18)$$

where the new parameter allows us to tune the modification factor,  $\mu = \left| \frac{\nabla\Phi}{a_0} \right|^n$ , as we wish. Newtonian gravity is recovered in the case where  $n=0$ .

So, we can see that solving this problem is entirely dependent on the expression for  $\Psi(r)$  which we must find using the MONDian form of the Poisson equation. We have already said we would prefer to use a model from the two-power law group of models so we can say that:

$$\nabla \cdot \frac{(\nabla\Phi(r))^{n+1}}{(a_0)^n} \equiv \frac{1}{r^2} \frac{\partial}{\partial r} \left( r^2 \left[ \frac{\partial\Phi}{\partial r} \right]^{n+1} \right) = 4\pi G \frac{\rho_o}{r^\alpha (r+a)^\beta} \quad (3.19)$$

which simplifies to:

$$\left[ \frac{\partial\Phi}{\partial r} \right]^{n+1} \propto \frac{1}{r^2} \int_0^r \frac{1}{r^{\alpha-2} (r+a)^\beta} dr \quad (3.20)$$

and subsequently integrates to:

$$\frac{1}{r^2} \int_0^r \frac{1}{r^{\alpha-2} (r+a)^\beta} dr = \frac{(r^{1-a})}{3-\alpha} (a+r)^{-\beta} \left( \frac{a+r}{a} \right)^\beta {}_2F_1 \left( 3-\alpha, \beta; 4-\alpha; -\frac{r}{a} \right) \quad (3.21)$$

Now we must define  ${}_2F_1(a, b; c; z)$ , a hypergeometric series, and subsequently  $(a)_n$ , the ‘rising factorial’ or Pochhammer symbol. We have met hypergeometric series before in the previous chapters but it is important here so we will just refresh ourselves on the definition (Hazewinkel, 1994):

$${}_2F_1(a, b; c; z) = \sum_{n=0}^{\infty} \frac{(a)_n (b)_n}{(c)_n} \frac{z^n}{n!} \text{ where } (a)_n = a(a+1)(a+2)\dots(a+n-1) \quad (3.22)$$

Thanks to a convenient similarity between  $a$  and  $c$  in our hypergeometric series and the fact that  $\alpha$  and  $\beta$  are integers in our models we can make things a little simpler:

$$\frac{(3-\alpha)_m}{(4-\alpha)_m} = \frac{(3-\alpha)(4-\alpha)\dots(3-\alpha+m-1)}{(4-\alpha)(5-\alpha)\dots(4-\alpha+m-1)} = \frac{(3-\alpha)}{(4-\alpha+m-1)} = \frac{(3-\alpha)}{(3-\alpha+m)} \quad (3.23)$$

So now we must solve the following:

$$\nabla\Phi(r) \propto \left[ \frac{(r^{1-a})}{3-\alpha} a^{-\beta} \sum_{m=0}^{\infty} \frac{3-\alpha}{3-\alpha+m} (-1)^m \left( \frac{r}{a} \right)^m \left( \frac{(\beta)_m}{m!} \right) \right]^{\frac{1}{n+1}} \quad (3.24)$$

Now we see the problem that often arises when trying to solve the MONDian Poisson equation with any generality. In order to proceed we need to integrate Eq. 3.24. We begin

by moving all  $r$  terms inside the sum as follows:

$$\nabla\Phi(r) \propto \left[ \frac{(a^{1-a})}{3-\alpha} a^{-\beta} \sum_{m=0}^{\infty} \frac{3-\alpha}{3-\alpha+m} (-1)^m \left(\frac{r}{a}\right)^{m+1-a} \left(\frac{(\beta)_m}{m!}\right) \right]^{\frac{1}{n+1}} \quad (3.25)$$

which would be tractable were it not for the need to take the  $(n+1)^{th}$  root of the entire right hand side. There is no analytical solution to this and it cannot even be simplified by examining limiting cases for the series. The series term for  $m=0$  is trivial and subsequent terms are divergent, as the Pochhammer symbol increases faster than the pre-factor of  $1/m$ , and oscillatory, due to the factor of  $(-1)^m$ . This means that it is not possible to analytically evaluate the root and then solve the integral.

The key point is that if we set  $n=0$  then we recover Newtonian gravity and the problem is still complicated, but is at least tractable. So now we see the problem of trying to solve the MOND Poisson equation and why we need to do so in order to use MOND to solve problems. In fact, the problem outlined here remains one of active interest in the field of modified gravity and has so far only been solved for certain models and limiting cases (Zhao, 1996). Currently, no way of obtaining a generalised solution, as we attempted to do here, is known.

### 3.6 Constructing MOND models

Having demonstrated an example where the MOND Poisson equation makes a problem intractable we shall now balance things out by presenting a circumstance where it does not. The next section will cover an example of using MOND to successfully describe a system of interest. We shall construct a fully analytic potential density pair and then prove that the velocity dispersions of the system will be analytic as well. The following is currently being developed in collaboration with Hongsheng Zhao.

Due to the scale of the MONDian solutions and the ongoing nature of the work we do not aim to present a complete solution here. For now we will be brief and merely show that an analytical MOND solution for the general system exists and then find results for a special case of this system using a simple MOND  $\mu$  function.

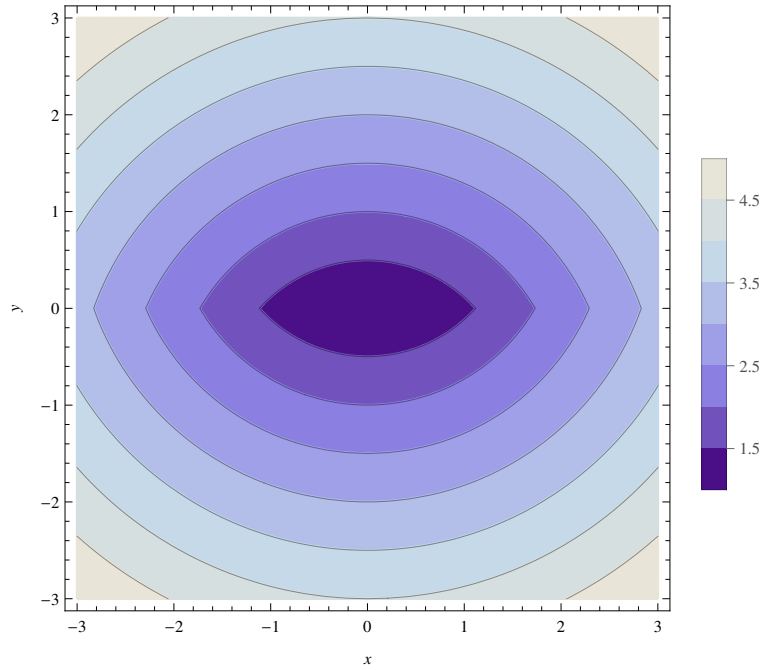


**Figure 3.1:** Example iso-potential contours of the potential described by Eq. 3.26 at a cross-section through  $z=0$ . The system is defined by  $A=\alpha=b=1$ .

### 3.6.1 Prolate spheroid densities

We examine the behaviour of closed orbits in a set of generalised potentials described by a surface  $S$ :

$$\phi = \frac{A}{\alpha} S^\alpha; S = \sqrt{x^2 + (b + R)^2}; R = \sqrt{y^2 + z^2} \quad (3.26)$$

where  $A$  and  $\alpha$  are constants and  $b$  is a factor that describes the departure from sphericity. Accordingly this describes a series of iso-potential surfaces which form a prolate spheroid whose symmetry axis is aligned with the  $x$ -axis. This potential can be created by different density distributions depending on the gravity law that is assumed. Fig. 3.1 shows a generic example of the iso-potential surfaces.

To derive the various velocity dispersions that we will need for later on we use the hydrodynamical equations for an axisymmetric, steady-state, collisionless, self-gravitating system given in Satoh (1980). In order to construct these equations it was assumed that the velocity distribution of the system's DF depends only on energy and  $x$ -axis angular momentum. This assumption is needed to constrain the complexity of the equations as

the implied symmetry removes cross-terms requires the last of the following three formula.

Note also that since we define our potential differently to Satoh (1980) our formulae differ in sign:

$$\frac{\partial}{\partial R} (\rho \langle v_R^2 \rangle) + \frac{1}{R} [\rho \langle v_R^2 \rangle - \rho \langle v_\theta^2 \rangle] = -\rho \frac{\partial}{\partial R} \phi \quad (3.27)$$

$$\frac{\partial}{\partial x} (\rho \langle v_x^2 \rangle) = -\rho \frac{\partial}{\partial x} \phi \quad (3.28)$$

$$\langle v_R^2 \rangle = \langle v_x^2 \rangle \quad (3.29)$$

where the latter is required by our assumptions about the form of the DF as stated previously. Next we find density by using the MOND Poisson equation:

$$\nabla \cdot [\mu(x) \nabla \phi(r)] = 4\pi G \rho \quad (3.30)$$

If we set  $\mu = 1$  then we will describe a Newtonian system and recover the density thus:

$$4\pi G \rho_N = A S^{\alpha-2} \left( \alpha + 1 + \frac{b}{R} \right) \quad (3.31)$$

The contours of this density profile are shown in Fig. 3.2. However, we can also choose a variety of alternative  $\mu$  functions to find other densities. The primary obstacle here is the size and complexity of the resulting expressions.

For instance, if we assume that the entire system is in the deep MOND regime then we can set  $\mu = \frac{|\nabla \phi(r)|}{a_0}$ . Since  $\phi$  is a separable function of  $x$ ,  $y$  and  $z$  this can be solved analytically and we thus arrive at the MONDian density:

$$4\pi G \rho_{Deep} = \frac{A^2 S^{3\alpha-6}}{a_0} \mathbf{P}_1 \quad (3.32)$$

where  $\mathbf{P}_1$  is a polynomial expression thus:

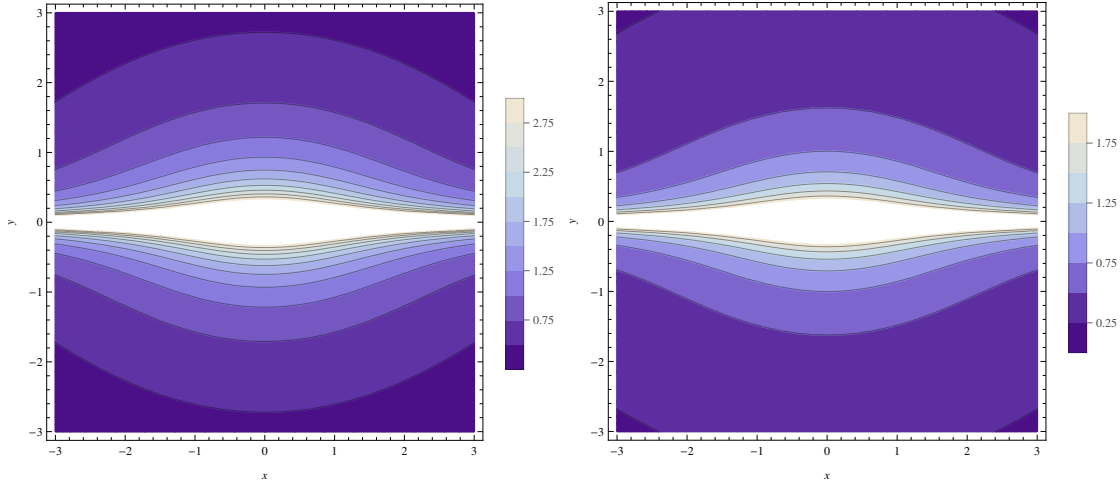


**Figure 3.2:** Iso-density contours of the Newtonian (left) and MONDian (right) solutions to the potential of Eq. 3.26. The system is defined by  $A=\alpha=b=1$ . We additionally define  $a_0$  to be of order unity such that the MOND density is noticeably different to the Newtonian one. Notice that the Newtonian density is greater than the MONDian as the colour ranges of the two plots is different.

$$\mathbf{P}_1 = \frac{b^5}{R} + 2b^4(2 + \alpha) + 2b^3R \left( \frac{x^2}{R^2} + 3 + 4\alpha \right) + 4b^2 (x^2(1 - \alpha) + R^2(1 - 3\alpha)) + \frac{b}{R} (x^2 + R^2) (x^2 + R(1 + 8\alpha)) + 2\alpha (x^2 + R^2)^2 \quad (3.33)$$

The contours of the density distribution are shown in Fig. 3.2. The shapes of the density contours are similar although the MOND model requires a lower density to produce the same potential.

This is a rather overly specific choice of  $\mu$  function and more usually we use the form from Eq. 3.4. However, this gives us an even more complex density distribution:

$$4\pi G\rho_M = \frac{A^2 S^{3\alpha-6}}{(a_0 + A S^{\alpha-1})^2} \mathbf{P}_2 \quad (3.34)$$

where  $\mathbf{P}_2$  is another polynomial expression thus:

$$\mathbf{P}_2 = \frac{A}{R} (b^3 + b^2 R(3 + \alpha) + b(x^2 + R^2(3 + 2\alpha)) + R(x^2 + R^2)(1 - \alpha)) + a_0 S^{-(\alpha+1)} \mathbf{P}_1 \quad (3.35)$$

This expression gives an analytic density distribution which displays the full range of MOND behaviour including a description of the transition between the Newtonian and MONDian regimes. Having demonstrated that MOND potential-density pairs do exist we would like to complete the model by finding analytical expressions for the velocity dispersions. Our three densities differ only in the number of terms and the values of coefficients and indices. Therefore, if one density produces fully analytic results for the following simple integrals then there is no reason to suspect the others would fail.

Accordingly we choose, for this section, to demonstrate that our models are fully analytical by finding solutions for only one model. We choose the Newtonian model as it is the simplest and this section is meant only as a proof of concept. The simplicity of the Newtonian density is useful because, as we will see, even it produces complex results for the velocity dispersions.

### 3.6.2 Finding the velocity dispersion

The first component to find is  $v_x$  through Eq. 3.27. Note that the x-axis is the symmetry axis of our systems:

$$\frac{\partial}{\partial x} (\rho \langle v_x^2 \rangle) = \rho A x \sqrt{(x^2 + (b + R)^2)}^{(\alpha-2)} = \rho A x S^{(\alpha-2)} \quad (3.36)$$

This can be solved by integration along the symmetry axis thus:

$$\rho \langle v_x^2 \rangle = A \int \rho x S^{(\alpha-2)} dx = \frac{-A^2 G \pi S^{2(\alpha-1)} (1 + \alpha + \frac{b}{R})}{8(\alpha - 1)} \quad (3.37)$$

This gives us our first dispersion component:

$$\langle v_x^2 \rangle = \frac{A S^\alpha}{2(1 - \alpha)} \quad (3.38)$$

We use our assumption about the symmetry of our velocity distribution equations to

state that  $\langle v_x^2 \rangle = \langle v_R^2 \rangle = \sigma^2$  and then return to the final part of Eq. 3.27 for the last component:

$$\frac{\partial}{\partial R} (\rho\sigma^2) + \frac{1}{R} [\rho\sigma^2 - \rho\langle v_\theta^2 \rangle] = -\rho \frac{\partial}{\partial R} \phi \quad (3.39)$$

Since we have an analytical result for  $\rho(R)$  and  $\sigma^2(R)$  we can evaluate the leftmost term first:

$$\frac{\partial}{\partial R} (\rho\sigma^2) = \frac{1}{8} A^2 G \pi S^{2(\alpha-2)} \left[ 2(b+R) \left( 1 + \alpha + \frac{b}{R} \right) - \frac{bS^2}{R^2(\alpha-1)} \right] = \mathbb{X} \quad (3.40)$$

Now we rearrange to find  $\langle v_\theta^2 \rangle$  and solve the other differentials:

$$\langle v_\theta^2 \rangle = \frac{R\mathbb{X}}{\rho} + R \frac{\partial}{\partial R} \phi + \sigma^2 = \frac{AR S^\alpha (1 + \alpha)}{2(b+R+R\alpha)(1-\alpha)} \quad (3.41)$$

This gives us all three velocity dispersion components.

### 3.6.3 A simple model

Now let's have a look at a simpler model that we can solve fully for the MOND case. This model is closely related to the more general example we have just examined, but is simple enough to produce smaller results for MONDian calculations. The simple model is the special case where:

$$\phi = \frac{A}{2} \log S^2 \quad (3.42)$$

This potential is not significantly different from the general model, is defined using the same terms, and is shown in Fig. 3.3.

So we would like to solve the Poisson equation again to find density. This time we make it a little easier by using the trick that:

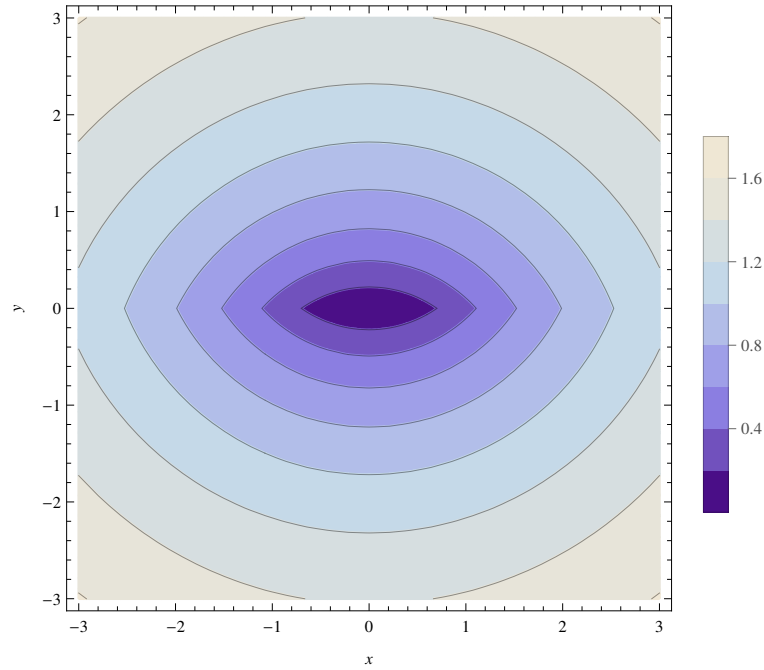


**Figure 3.3:** Example iso-potential contours of the potential described by Eq. 3.42 at a cross-section through  $z=0$ . The system is defined by  $A=b=1$ .

$$\frac{d}{dx} \log(f(x)) = \frac{d \log(f(x))}{df(x)} \frac{df(x)}{dx} = \frac{1}{f(x)} \frac{df(x)}{dx} \quad (3.43)$$

Now we solve the Poisson equation. The Newtonian solution is simplest as per usual:

$$4\pi G \rho_N = \frac{A(R+b)}{RS^2} \quad (3.44)$$

However, we are going to find a MOND solution to work with. We are going to use  $\mu = \frac{|\nabla\phi(r)|}{a_0}$  which, as stated before, is not the most powerful choice. However, it does describe the MOND behaviour of the system while also being compact enough to express the results easily.

$$4\pi G \rho_{Deep} = \frac{A^2 b}{a_0 R S^3} \quad (3.45)$$

This density distribution is also very similar to previous models. Fig. 3.4 shows the density profiles of these models.

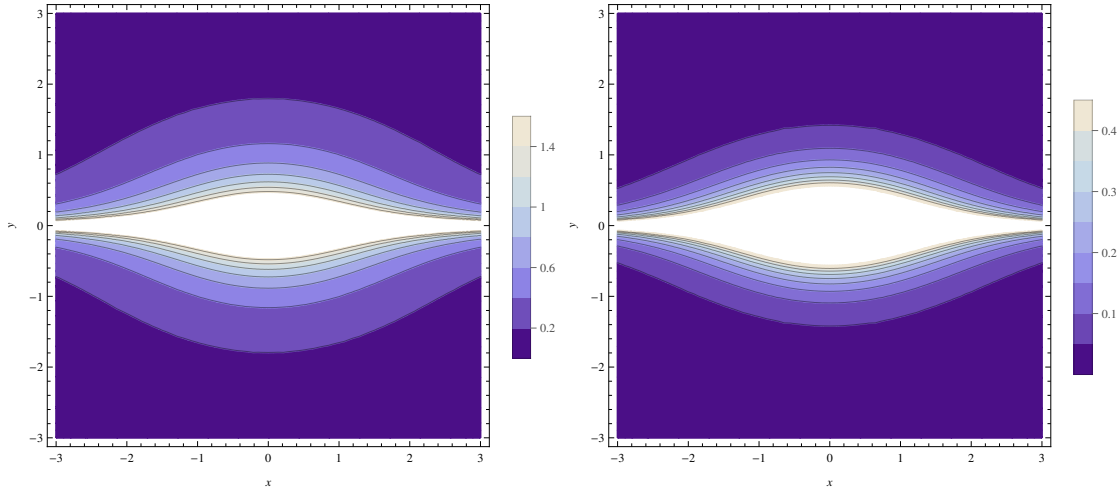


**Figure 3.4:** Iso-density contours of the Newtonian (left) and MONDian (right) solutions to the potential of Eq. 3.42. The system is defined by  $A=b=1$ . We additionally define  $a_0$  to be of order unity such that the MOND density is noticeably different to the Newtonian one. Note that the contours for the MONDian case are considerably smaller as the model has a significantly lower central density.

Now we begin to find the dispersions as before. It is also interesting to note that we can use the trick from Eq. 3.43 to simplify Eq. 3.27:

$$\frac{1}{\rho} \frac{\partial}{\partial x} (\rho \langle v_x^2 \rangle) = \langle v_x^2 \rangle \frac{\partial}{\partial x} (\log(\rho)) \quad (3.46)$$

So, we can find the first component in exactly the same way as we did previously:

$$\frac{\partial}{\partial x} (\rho \langle v_x^2 \rangle) = \frac{\rho Ax}{S^2} \quad (3.47)$$

This can be solved by integration along the symmetry axis thus:

$$\rho \langle v_x^2 \rangle = A \int \frac{\rho x}{S^2} dx = \frac{A^3 b}{12\pi G a_0 R S^3} \quad (3.48)$$

This gives us our first dispersion component:

$$\langle v_x^2 \rangle = \frac{A}{3} \quad (3.49)$$

Importantly, it should be noted that this is a constant. This means that the dispersion is independent of the shape of the potential which implies that it is also independent of the  $\mu$  function. In short, this result is the same in Newtonian systems which is why this system is useful for this demonstration.

We can use the same assumptions of symmetry for  $\langle v_R^2 \rangle$  which only leaves  $\langle v_\theta^2 \rangle$ . Returning to Eq. 3.27 we say:

$$\frac{A}{3} \frac{\partial \rho}{\partial R} + \frac{A\rho}{3R} - \frac{\rho \langle v_\theta^2 \rangle}{R} = -\rho \frac{\partial \phi}{\partial R} \quad (3.50)$$

With our simple expression for the other dispersion we can rearrange this to:

$$\langle v_\theta^2 \rangle = R \frac{\partial \phi}{\partial R} + \frac{A}{3} \left[ 1 + \frac{R}{\rho} \frac{\partial \rho}{\partial R} \right] \quad (3.51)$$

First let's look at the derivative term on the far left:

$$\frac{\partial \rho}{\partial R} = \frac{-A^2 b(b^2 + 5bR + 4R^2 + x^2)}{4G\pi a_0 R^2 S^5} \quad (3.52)$$

We also calculate  $\frac{\partial \phi}{\partial R}$ :

$$\frac{\partial \phi}{\partial R} = \frac{A(b+R)}{(x^2 + (b+R)^2)} \quad (3.53)$$

When these are substituted in it transpires that all the factors cancel out to yield the final dispersion:

$$\langle v_\theta^2 \rangle = 0 \quad (3.54)$$

We can phrase our potential in a more convenient manner and give  $\frac{A}{2}$  a more helpful and physically relevant representation by setting  $A \rightarrow v_\infty^2$  where this is the square of the velocity required to escape the system to infinity.

So, this brings us to the end of our demonstration. We have used a general potential and proved that MOND can produce perfectly good analytic potential density pairs as well

as solve for analytic velocity dispersions. This is important because, outside of spherically symmetric models and razor-thin disks (Brada & Milgrom, 1995), it can be difficult to find MONDian equivalents of Newtonian potential-density pairs. The main obstacle to the models presented here is the size of some of the results which can make them unwieldy and obfuscate the underlying physics.

Regardless, in order to have any theory that is general enough to be worth the effort it must be able to replicate the results of general relativity which is something that this approach cannot do without further modification.

### 3.7 Relativistic approaches

As we have seen, constructing a theory of gravity that fixes the problems we've discussed while still remaining usable is a significant challenge. It is, however, a challenge that has been taken up by many and a large population of relativistic gravity theories now exist that have shown promise in eliminating the need for dark matter/energy.

The first relativistic theory came from Bekenstein (2004) after considerable work on a relativistic version of the AQUAL theory he had developed to fix the problems in MOND (Bekenstein & Magueijo, 2006). Previous attempts at such a theory had been made, but had so far met with failure in the face of superluminal wave propagation and an absence of gravitational lensing effects.

Bekenstein's attempt, termed Tensor-Vector-Scalar Gravity or 'TeVeS', was a significant theoretical success on multiple counts as it could reproduce the results of MOND in the non-relativistic limit as well as the results from strong lensing observations (Bekenstein, 2009; Chiu et al., 2011) and cosmological structure formation (Dodelson & Liguori, 2006). The name comes from the components that build the theory – the order is important as a different theory, scalar-tensor-vector gravity, is easily confused with TeVeS – namely a tensor metric, a scalar field, and a time-like 4-vector field.

Another relativistic MOND theory is conformal gravity. This theory was created with the main goal of fixing the dark energy problem as well as attempting to bridge the gap between quantum mechanics and gravity (Mannheim, 2010). Conformal gravity is based on the idea that gravity possesses an extra invariance with respect to isotropic stretching of the metric which restricts the choice of action to one based on a different tensor to the

standard Einstein tensor (Mannheim & Kazanas, 1989).

This has the rather interesting property of preempting the arbitrary addition of a cosmological constant term. In conformal gravity the term arises naturally after conformal symmetry is broken which also gives rise to particle masses in a process analogous to the Higgs symmetry breaking (Mannheim, 2006). Given that it was designed only to address the dark energy problem it is also encouraging that the theory can decently reproduce galactic rotation curves (Mannheim & O'Brien, 2012) and offer a possible path towards a theory of quantum gravity by containing the Higgs mechanism explicitly (Mannheim, 2012).

Conformal gravity's lofty goal of describing a workable theory of quantum gravity is one it finds a measure of success at. For example, it was long suspected that any theory of gravity that had a Poisson equation of higher order than Newtonian gravity would generate 'ghosts'. Ghosts are states in quantum field theories which possess negative kinetic energies and thus violate unitarity – the principle that the probability of all allowable states will always sum to unity – and/or causality. As such, their presence is regarded as indicative of the failure of the theory and its subsequent breakdown in the quantum limit (Robert & Smilga, 2008; Gershtein et al., 2009).

Conformal gravity makes use of a fourth-order Poisson equation and would thus be expected to generate ghosts. One of the successes of the theory was the proof that, while it does produce these ghost states, they carry no energy and do not have any physical meaning beyond an abstract mathematical artefact (Mannheim, 2006, 2008). This showed that to regard theories of gravity with higher order Poisson equations as intrinsically flawed was an over-generalisation.

### **3.8 Working in conformal gravity**

To look at conformal gravity in more detail let us examine the predictions of conformal gravity at the scale of galaxy clusters, an area where the theory has so far failed to be particularly successful. The following is based on Horne (2006) and was a brief, collaborative effort to see if the results could be improved. Specifically, Horne (2006) finds that conformal gravity overpredicts the observed gravitational potential in galaxy clusters following an analysis of the cluster Abell 2029.

In the non-relativistic limit we need to solve the conformal version of Poisson's equation which, as was mentioned earlier, is different from Newtonian gravity as the use of the Weyl tensor increases the equations to fourth order. It is worth comment that it is still possible to find solutions that reduce to the Newtonian limit without having to explicitly recreate a second-order system. In practice this means that conformal gravity is distinct from Newtonian dynamics and its subsequent dark sector problems but retains the familiar, local scale behaviour. In the non-relativistic limit the equations of conformal gravity are (Mannheim, 2008, 2012):

$$\nabla^4\phi = 4\pi G\rho \text{ where } \frac{\phi}{c^2} = \frac{-\beta}{r} + \frac{\gamma r}{2} - \frac{\kappa r^2}{2} \quad (3.55)$$

where the extra terms on the right hand side produce behaviour associated with external sources. The standard Newtonian potential is described by  $\beta$ , the 'dark matter' perturbation is accounted for in the local linear  $\gamma$  term while further modifications come from inhomogeneities in the cosmological mass background and are encapsulated in non-local quadratic  $\kappa$  term.

In the initial analysis of Horne (2006) the quadratic cosmological term was felt to be of negligible importance and was dropped from the calculation. However, in this analysis the quadratic term was retained to see if it could alleviate the error in the results. We thus find a mass profile different to that of Horne (2006).

In this analysis we use X-ray temperature and density observations of the cluster Abell 2029 (Lewis et al., 2003) to compare the calculated mass of the cluster with the mass predicted by conformal gravity under the assumption of hydrostatic equilibrium:

$$\frac{dP}{dR} = -\rho \frac{d\Phi}{dR} \quad (3.56)$$

If we re-parameterise Eq. 3.55 in more familiar terms of mass and radius we arrive at the following expression for the mass profile:

$$M(R) = \frac{M_N - M_0 \left(\frac{R}{R_0}\right)^2 - \Delta M}{1 + \left(\frac{R}{R_0}\right)^2 - 2\left(\frac{R}{R_1}\right)^3} \quad (3.57)$$

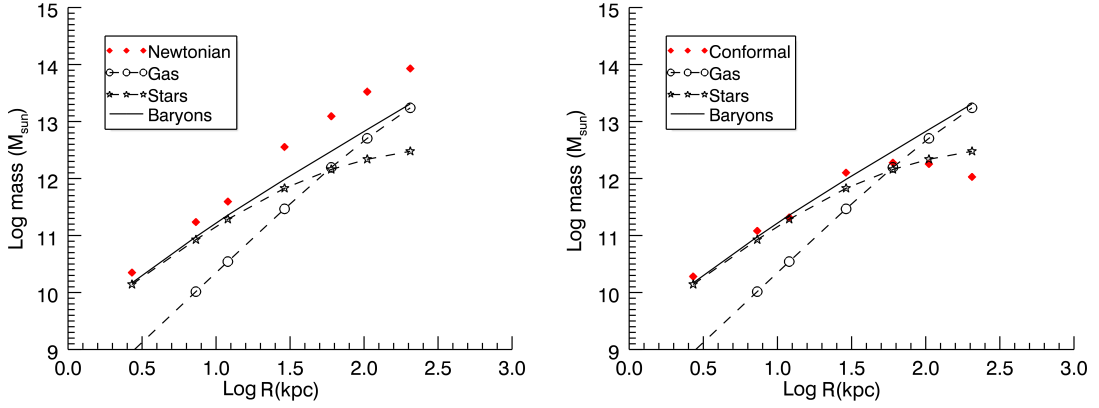


**Figure 3.5:** Comparison of the problems faced by Newtonian and Conformal prediction of the mass profile of Abell 2029. Newtonian mechanics overpredicts the baryonic mass profile while the conformal gravity under-predicts it. Note that the conformal prediction would agree well with the mass of the stellar component were it not for the decrease in the mass profile at large radii.

where  $M_N$  is the Newtonian mass profile and  $M_0 = 5.6 \times 10^{10} M_\odot$ ,  $R_0 \sim 24$  kpc, and  $R_1 \sim 18$  Mpc give the scales of the mass, local linear modification, and cosmological term respectively (Horne, 2006; Mannheim, 2008). The  $\Delta M$  term is a correction term that stems from a complication compared to the Newtonian case where spherical shells of matter internal to a radius,  $r$ , have slightly weaker potentials and external shells slightly enhance the inward gravitational pull:

$$\frac{\Delta g(R)}{g_0} = \frac{2}{3} \int_{r>R} \frac{R}{r} \frac{dM}{M_0} - \frac{1}{3} \int_{r<R} \left(\frac{r}{R}\right)^2 \frac{dM}{M_0} \quad (3.58)$$

As should be apparent from that description, the mass profile thus depends circularly on itself and an iterative process is used to obtain a self-consistent solution. When we apply this process we find that conformal gravity overpredicts the gravitational field strength in the cluster and consequently under-predicts the cluster's mass.

As we can see in Fig. 3.5, while Newtonian dynamics leads to the dark matter problem, the conformal analysis predicts too little mass and also, somewhat worryingly, even suggests the enclosed mass should decrease in the outer edges of the system. This was the problem that lead to this re-analysis and the fact it remains suggests the impact of adding the quadratic term is negligible. This is a significant problem for the theory but there may

be a solution.

One of the founding assumptions is that the system is in hydrodynamic equilibrium. Due to the non-Newtonian impact of matter external to a given radius, this assumption, if violated, could cause the apparent mass profile to become negative. Abell 2029 was chosen for this analysis specifically because it is often regarded as being a very dynamically relaxed object (Sarazin et al., 1998; Lewis et al., 2002, 2003) but there is uncertainty as to whether this is entirely true.

There is debate as to whether Abell 2029 possesses a cooling flow (Molendi, 1999) or not (Lewis et al., 2002). More recently there is also evidence for significant non-equilibrium sub-structure in the cluster which may potentially contain around  $6 \times 10^{12} M_{\odot}$  (Clarke et al., 2004) which, interestingly, is the order of magnitude of mass that is upsetting the conformal analysis.

If it turns out that there are significant bulk flows and inhomogeneities in the cluster then that could explain the poor predictions made by the theory however the issue is currently unresolved for this cluster. The results for other clusters are mixed, with conformal gravity fixing some problems (Mannheim & O'Brien, 2012; Yang et al., 2013) but not others (Diaferio & Ostorero, 2009).

The discussion about the merits of MOND versus dark matter is an ongoing one and it is time to move on. In my opinion, by way of conclusion, I echo the sentiments of some authors who feel that the opposing successes and failures of the two approaches mean that a marriage of the two will be required to completely explain the universe we observe (Feix et al., 2008; Bekenstein, 2009; Bruneton et al., 2009).

# 4

## Numerical simulation

*“We can lick gravity, but sometimes the paperwork is overwhelming.”*

— *Wernher von Braun*

As we have seen in previous sections, attempting to model the evolution of specific systems in a purely analytical context is always non-trivial and often impossible. In order to overcome the limitations of the analytical approach, large systems are often modeled by starting with some initial condition and then evaluating every inter-particle interaction to see how the system will change over a small time interval. This process is repeated until the simulation has evolved enough for results to be taken from it. This is often computationally expensive but allows for the solution of problems much too complex to be modeled any other way.

The field of modern N-body simulation is a comparatively young one, but it can trace its heritage to the turn of the 1700s. Around this time, Isaac Newton had created an outstandingly powerful and modern theory of gravity that allowed astronomy to become

more than just cataloguing the motions of celestial objects. With the development of the laws of gravity and motion, astronomers could now predict the motions of stars and planets like never before however, almost immediately, there was a problem.

The so-called ‘three body problem’, and its more generalised counterpart the ‘N-body problem’, meant that Newton’s equations could not produce the equations of motion for more than two objects. Some special solutions are known and there are ways, albeit unwieldy ones, to move forward with such a problem analytically but progress only really started to be made with the advent of the computer.

With the aid of a computer, the equations of motion could be solved by discretising the time-evolution of the system. A computer could crunch the numbers fast enough to move from particle to particle, working out the forces exerted on them as it went. It could then use the resulting accelerations to advance a small amount of time before doing the whole process again. However, even with the aid of modern hardware, solving the N-body problem in this way is immensely time-consuming.

If one performs the most simplistic type of N-body simulation *i.e.* looks at each particle and computes the sum of all the force vectors from every other particle, then the problem scales as  $O(N^2)$  which is prohibitively large for even a modest simulation. Although modern codes have reduced the scale of the problem to only  $O(N \text{Log}(N))$  and modern hardware has increased processing speeds enormously, the simulations remain slow and laborious.

What follows is a short overview of the primary building blocks that make up typical N-body codes but without too in-depth a discussion about the codes themselves. This will become relevant in subsequent chapters as we examine a variety of results derived from these simulations.

## 4.1 Generating initial conditions

The first step in any numerical simulation is to form an initial system of particles that models the system of interest. We wish to take an analytical expression for our system – such as a density or potential profile or just the DF – and turn that smooth function into a discrete list of positions and velocities. This is a delicate procedure and one that must be done carefully. If the method leaves a portion of phase-space unfilled, creates artificial

substructure, or does not construct orbits correctly then the system will not be stable and, more seriously, will not represent the behaviour of the intended system.

Now, any algorithm that converts a smooth function to a discrete one will be lossy by definition and that incurs a degree of error associated with the loss of resolution. Accordingly, a variety of methods have been developed to minimise the impact of this and generate high quality systems. We will now spend a moment to look at three different approaches that have been developed.

The first and most simple method is to simply use the Jeans equations. Given initial assumptions about the density and anisotropy profiles the Jeans equations will describe the corresponding velocity dispersion. If the velocities are assumed to be Gaussian then the resulting structure will be at least stable enough that it will settle to equilibrium after some evolution in an N-body simulator (Hernquist, 1993). This assumption is not quite enough of a limitation to make the method useless but there are considerably more powerful tools available.

Next there is a simple form of Monte Carlo method. One can simply take the probability distributions of angular momentum and energy and run a Monte Carlo method. This generates a list of energies and momenta which are picked at random according to the probability weighting specified in the DF. This method is pleasantly simple, but must be monitored to ensure that particles are set up so that they are evenly distributed in real-space and are on stable orbits. It is these latter two points that are the sticking point with such methods as they are non-trivial tasks.

Finally, we look at an idea called the Schwarzschild method (Schwarzschild, 1979) which is more involved than the others. It takes a desired analytical density profile and uses a numerical solver to produce a discretised potential grid. The potential is then seeded with orbits that sample a large volume of the system's phase-space. The amount of time that a particle on a given orbit spends in a cell is then compared with how much mass should be expected in that volume. This is used to calculate a weight for that orbit. The final stage is to sample these orbits based on their relative weights to populate the numerical model. This method guarantees that all orbits will be valid and the mass distribution will be the one that was desired (Wu et al., 2009).

After we have generated initial conditions we need a simulator to evolve them. There

are a huge variety of codes available which are designed to be better at solving specific kinds of problems. Since the purpose of this chapter is just to provide some background for the chapters to come after we will only look at two codes that are good for explaining the basics.

## 4.2 GADGET-2: a Newtonian code

One of the more well-known simulation codes is GADGET-2, a massively parallel code which has been widely used for cosmological modeling (Springel, 2005). GADGET-2 is a useful code to examine as a brief overview since it combines a large variety of techniques to achieve its high degree of efficiency and flexibility. It also contains a variety of code modules for modeling star formation and feedback, radiative transfer, and so on but we will not include these in our discussion here.

I will, however, briefly mention the general methodology behind the modelling of short scale, hydrodynamical portions of a simulation which is carried out by GADGET-2's smoothed particle hydrodynamics (SPH) module. SPH is not used in the work detailed in this thesis, but it is still interesting and worth a moment to explain.

SPH, as the name suggests, models the evolution of a smooth density field by tracking a population of discrete particles. The trick is that the particles can recover the field by being smoothed over a finite volume by the application of a smoothing kernel. It should be noted that the smoothing is a function of relative position so that the particle's density is highest at the exact position of the particle and decreases with distance. The density in a cell can then be computed by counting the contributions from all nearby particles:

$$\rho_i = \sum_{j=1}^N m_j W(|r_i - r_j|, h_i) \quad (4.1)$$

where  $W(r, h)$  is a kernel which describes how particles are smoothed,  $h$  is the characteristic length of the smoothing,  $\rho_i$  is the total density at a position  $i$ , and  $m_j$  is the mass of the  $j^{\text{th}}$  particle. Subsequent properties of the density distribution can be interpolated from the values of the recovered field at that point. The behaviour of the particles at small scales is inferred from a hydrodynamical treatment that prescribes viscosity and the resulting pressure forces affecting particles with small separations from each other.

### 4.2.1 Tree and TreePM force calculations

In order to model the gravitational interaction between particles it is, naively, necessary to consider each possible pair-wise combination of particles one by one. This is wasteful in almost every circumstance but especially when one considers the relative importance of forces from particles close by compared to those much further away. One method to simplify the problem is to break the volume into blocks based on distance from the particle under consideration. Particles that are close by will be considered individually whereas particles further away will be grouped into one calculation by being approximated as a single particle at the centre of mass of the sub-volume.

The error that this process introduces will increase with the characteristic size of the sub-volumes, with the exact solution being regained if the volumes are so small they contain only one particle. This is the basis of a tree code such as the one employed by GADGET-2.

In the case of GADGET-2 the construction of the tree is carried out as follows. The volume is initially divided into 8 equal sections that are split along the coordinate axes of the system which is why this method is known as an oct-tree. Other trees can be constructed that split the volume into other amounts; however 8 blocks is a natural choice for a three dimensional cartesian space. Each sub-volume is then queried for its contents and examined to see whether, within some pre-defined limit, the current level of resolution is appropriate.

If the accuracy is unacceptable and too many particles are spread across the cell then the sub-volume is itself sectioned into 8. The process continues until every sub-volume is of a sufficiently small scale and contains a small enough number of particles. If a sub-volume is a large distance away then multiple sub-volumes can be evaluated at once by looking at the large sub-volume that contains them. To link this process with a tree structure, every node on the tree leads to 8 branches which refer to the sub-volumes of the higher-tier branch that contains the node. Leaf nodes represent volumes with no further requirements for sectioning.

This process has many desirable features ranging from the natural way in which this kind of tree structure can be processed in computer memory to the ease with which the

accuracy can be increased on the fly by simply introducing another level into the tree hierarchy. The tree is also useful as it naturally encodes information about particle nearest-neighbours which is needed for evaluation of the SPH calculations.

GADGET-2 also features a variant on the standard tree algorithm which mixes the above procedure with a particle mesh method. For short distances, the full tree procedure is applied as we have discussed already. However, beyond a certain cutoff, the algorithm uses a particle mesh to determine the forces produced by groups of particles. Particle mesh methods use a similar approach to SPH as they smooth a set of particles out into a continuous field and then sample that field at whatever points are required for the next calculation.

This hybrid algorithm of a mesh for distant particles but a tree code for nearby particles is known, somewhat clumsily, as a particle-particle-particle-mesh or P<sup>3</sup>M method. For the particle mesh section a smoothing kernel is applied to the particles, just like in the SPH method, and a continuous distribution is produced which is then sampled at each point on the mesh. Next, the Fourier transform of the mesh field is found as, thanks to a trick in Poisson's equation, the density relates to a potential directly through Fourier space as follows:

$$\begin{aligned}\phi(\vec{x}) &= \int e^{i\vec{k}\cdot\vec{x}}\phi'(\vec{k})d\vec{k} \rightarrow \nabla_x^2\phi(\vec{x}) = \int e^{i\vec{k}\cdot\vec{x}}(i\vec{k})^2\phi'(\vec{k})d\vec{k} \\ \rho(\vec{x}) &= \int e^{i\vec{k}\cdot\vec{x}}(i\vec{k})^2\phi'(\vec{k})d\vec{k} \text{ therefore } -\vec{k}\cdot\vec{k}\phi'(\vec{k}) = \rho'(\vec{k})\end{aligned}\quad (4.2)$$

GADGET-2 then takes an inverse transform and work out the potential at each point of interest before using the differences between points to construct forces. After some adjustment for boundary issues and smoothing errors the force from distant regions is known and the computation can proceed. This method offers an increase in speed over pure tree methods but suffers from resolution problems when focusing on very small, dense regions of larger simulations.

### 4.2.2 Time-step determination

The final building block of any N-body code is a way to determine appropriate time-steps for the system. Shorter steps offer higher accuracy but at the cost of additional computational cycles and it is not always easy to tell whether a higher temporal resolution will offer any tangible improvements. GADGET-2 implements an iteration scheme known formally as a ‘symplectic leapfrog scheme’. First of all, describing a code as ‘symplectic’ means that it conserves the phase-space distribution. This is a more powerful conservation requirement than simply conserving energy or momentum as the errors in the orbits do not diverge over time.

Next, the name goes on to describe the order in which the steps in the algorithm are applied. The code treats the change in the position of particles as a different operation to computing the change in momenta. These two operations are generally referred to as the ‘drift’ and ‘kick’ steps of the code and the designation as a ‘leapfrog’ code means that the steps are carried out alternately. This scheme is better than just carrying out a direct Runge-Kutta integration of the entire system as the leapfrog scheme coupled with the symplectic code means that no long-term trends arise in the system.

The actual force calculations are carried out differently depending on whether the forces are long-range or short-range. The drift step is always carried out as it is not very computationally expensive however the kick step is only carried out every single time-step for short-range forces. Long-range forces are weaker and thus induce much smaller accelerations. This means that the long-range forces cause variations over much longer timescales and can be evaluated at less frequent intervals. Due to the fact that short range forces are computed via a tree, it is easy to perform this kind of segregation compared to, say, a pure PM scheme where every particle is used to compute the potential.

It is also interesting to note that schemes which alternate in the order kick-drift-kick suffer considerably less error than drift-kick-drift schemes despite their equal computational cost (Springel, 2005). In short, this is because the acceleration used in the determination of the step duration is found found during the kick step as that is when the forces are applied. In a drift-kick-drift scheme the accelerations are computed partway through the timestep rather than at the point that the step is initiated which leads to a systematic error. This same source of error exists in kick-drift-kick schemes but is smaller because the

timestep is calculated at the same instant that the accelerations are recalculated.

### 4.3 NMODY: A MONDian code

The problems involved in creating an N-body simulation are magnified once the problem is posed in the MONDian paradigm and only a couple of simulation codes exist that can efficiently deal with the equations involved. The dependence of force on local accelerations means that interparticle forces cannot be computed using the simple, linear equations of Newtonian dynamics which makes finding an algorithm that is not computationally expensive rather challenging.

A particular problem is that few aspherical MONDian potential-density pairs have established analytical solutions, such as the case of the razor-thin disk (Ciotti et al., 2006), which makes solving the MOND Poisson equation more challenging than in the Newtonian case. NMODY (Londrillo & Nipoti, 2009) gets around the problem by implementing a perturbation algorithm which deforms a spherical potential to get a suitable approximation to the aspherical MOND solution.

First, a spherical density profile is designed to have radial behaviour as close as possible to the desired profile. The deep-MOND potential of the system is calculated, regardless of whether or not the system is in the MONDian regime, as that allows use of the simpler differential operator:

$$\frac{d\phi_0}{dr} = g_0 = \frac{\sqrt{GM_0(r)a_0}}{r} \quad (4.3)$$

If the Laplacian and MONDian operators are applied to the potential then we retrieve the density distribution which sources that potential in both those theories. For the next step we deal in Newtonian dynamics where the relations between potential-density pairs are well understood. A perturbative, non-spherical density is added to the Newtonian density distribution to create an overall distribution closer to the one under study. The associated Newtonian potential can now be found, as the aspherical perturbation can be expressed as a potential in Newtonian dynamics.

This produces a potential that is comprised of a component equivalent to the *spherical* deep-MOND system with an additional *aspherical* perturbation that has come from

Newtonian dynamics. The final step is to take the new, combined potential and apply the deep-MOND operator to recover the aspherical MOND density distribution alongside its potential.

### 4.3.1 Force calculations and time-steps

NMODY uses a rather unusual iterative scheme alongside a standard particle mesh to derive the forces experienced by particles in MONDian simulations. Firstly, the code examines the density distribution and approximates it as an exact spherical solution, or takes the previous state of the system, as the starting point. The difference between the assumed density distribution and the actual distribution is assessed by assessing the convergence between the acceleration field produced by the density and the density implied by the potential. When the two are, to within some accuracy, producing the same accelerations then that potential is used.

Aside from the above, NMODY is fairly standard in its implementation. For simulations that only require Newtonian physics it applies a basic self-consistent field method and in all instances it uses a standard symplectic leapfrog scheme for the timesteps. The self-consistent field method is worthy of further explanation, however it will become particularly important in two chapters time. To avoid repetition we will delay our discussion until then.

## 4.4 Hardware and next generation codes

So far we have only discussed software which is, admittedly, where most of the development lies. However, there is only so far that a piece of code may be optimised before the gains in efficiency reach a plateau and the only way to increase the power further is through a change in the hardware. Normally addressed naturally as part of the evolution of hardware according to Moore's Law but from time to time there is a paradigm shift in hardware architecture that accelerates the process.

### 4.4.1 GRAPE

One of the first examples of this is the GRAvity PipE (GRAPE) architecture that was developed during the 90s (Ebisuzaki et al., 1990; Ito et al., 1990; Makino & Funato, 1993). GRAPE was the outcome of a very successful attempt to create a kind of hardware that was

specifically designed to perform calculations for interactions that scaled as  $r^{-2}$ . GRAPE is undoubtedly useful, and not only within the realms of astronomical simulation, but suffered from significant drawbacks. The system was capable of refinement and extension and to date there have been six generations of GRAPE hardware produced with later versions including features such as SPH (Steinmetz, 1996). However, evolution of the system was hampered by the fact that all of the fundamental physics is, by definition, hardwired into the system to speed up the pipeline.

The disadvantage of this is quite clear. If one wanted to run a simulation to study MOND then that would potentially require the design of a specialised GRAPE processor. Even inside the realm of Newtonian mechanics, any attempt to upgrade to faster hardware would require purchase of the specialist processor boards rather than general purpose hardware. Additionally, code must be designed specifically for a GRAPE machine which can create problems of portability if a GRAPE board is not available.

The GRAPE series is still ongoing and has gained much recognition from the hardware industry, however there are alternatives available which could overtake it in popularity. First among these is the increased power of graphics processors (GPUs) and their surprising suitability to N-body simulations. There are a couple of GPU architectures that have developed an interface suitable for use as a high performance cluster but this section will focus only on the NVIDIA architecture known as CUDA.

#### 4.4.2 CUDA

GPUs are normally associated with rendering textures and lighting effects and have been specifically designed to excel in those regimes so it takes a little thought to appreciate how this can relate to N-body simulations. To begin with, consider a texture file. A texture is a large array of pixels that is read in quickly from memory and then manipulated in some geometric space. This requires that a large number of pixels must be held and processed simultaneously, but does not require any real computational power besides simple geometric transformations.

Now, a CPU is designed to handle a single request extremely quickly which makes them powerful for operations such as user input or controlling an internet connection but leaves them unable to cope with the sheer volume of simultaneous operations. A GPU,

however, contains a huge number of processors which work in parallel. Each processor is considerably slower than a single CPU but when the texture is broken down into smaller pieces and divided among the processor units of the GPU the increased parallelism means the operation is carried out considerably faster.

While the actual mechanics of rendering images are a bit more involved than that simple example, the point still stands that GPUs are designed to execute a simple command multiple times by using a high bandwidth connection to a large number of individual processors. This can be applied to solving the N-body problem by, in the simplest instance, tasking each processor to evaluate the force on a single particle. Due to the large number of processors involved the kick and drift steps can be completed in a fraction the time it would take even a powerful multi-core CPU.

Using the hardware for this has been made much easier by the development of specialised software libraries that allow for a developer to write code directly for the hardware. CUDA has libraries that extend popular languages such as C and FORTRAN which has allowed development of scientific codes to accelerate.

I do not want to get too deeply into technical specifications, but I will note a few key figures to emphasise the scale of the improvement. A typical consumer level CPU will have around eight cores which can then be connected to other CPUs via an interface such as MPI. A consumer level GPU on the other hand will have hundreds of cores that, in the case of a high-end GPU unit, can reach teraflop processing rates with total chip bandwidths of several TB/s. Overall, a networked series of GPUs can outperform a similar investment in CPU hardware by over an order of magnitude.

The CUDA architecture is not without its drawbacks, however. While NVIDIA have put admirable resources into building GPUs that are built specifically for simulation work, they still use the same underlying architecture as any other CUDA-enabled device which, ultimately, is designed for rendering images. This has several implications. For example, when jobs are divided between processor threads the threads are then run on separate blocks which cannot communicate with each other. There are pools of shared memory, but interaction between threads is limited and attempting to force a level of communication between them comes at a significant cost to speed. For a visual representation of this see Fig. 4.1.

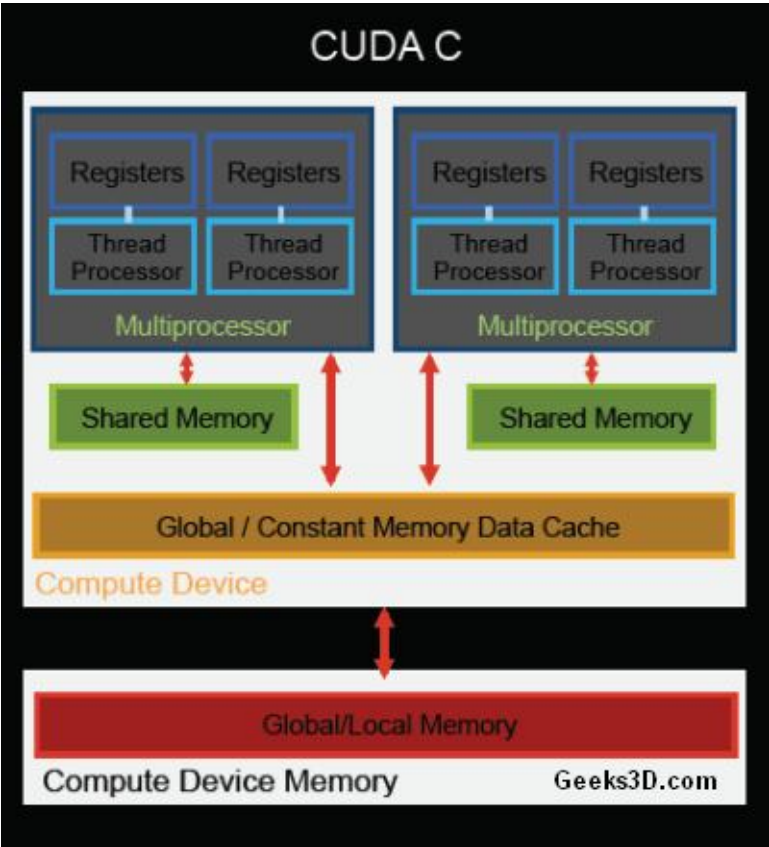


Figure 4.1: A schematic representation of the division of memory between streaming multi-processor blocks on a CUDA GPU. Image credit: [www.geeks3d.com](http://www.geeks3d.com)

Additionally, the processors are not designed for user input or for conditional evaluation and under such circumstances will produce undesirable behaviours such as evaluating all possible outcomes of a conditional statement. It is generally recommended that a host CPU carries out all operations that require conditional evaluation or user input before packing all the data off to the GPU for processing in a way rather reminiscent of GRAPE. Note, however, that this means it is impossible to pass pointers to the GPU as the two devices are not in the same memory space. Also problematic is the fact that the processor kernel that runs on a block of processors must be the same for each.

Overall, the advantages of GPU processing far outweigh the drawbacks if the code is designed properly. In only the last few years a large variety of codes have been created such as NBSymple (Capuzzo-Dolcetta et al., 2011), OCTGRAV (Bédorf & Portegies Zwart, 2012), and GENGA (Grimm & Stadel, 2014), not to mention the ones designed for other libraries. While this is an area of significant personal interest we do not make use of this technology in our work and I will now move on to other topics. All the above information is available in much greater technical detail at NVIDIA's CUDA section of their developer portal listed in online resource [5]. A more detailed look at the astrophysical implications of the technology can be found in the excellent review of Bédorf et al. (2012).

#### 4.4.3 **Quantum processing**

Popular understanding is that the development of quantum computing will lead to a paradigm shift in the speed at which computers function, so it seems appropriate to ask about the potential for N-body. This was a simple enough task when we looked at CUDA but then CUDA is, ultimately, just an extension of existing classical computing methods. When it comes to discussing the benefits of quantum computing the issue is considerably more complex.

The problem with quantum computing technology is that it is not the same as just packing more processors on to a chip or changing the architecture; it is a fundamentally different way of computing a problem. A quantum computer functions by encoding a mathematical problem into the quantum states of a particle, entangling the states with the states of other particles in a way that encodes a question, and then collapsing the states to leave a set of states that form the answer.

A classical computer based on electrical semiconductors possesses memory units that encode binary information into a 'bit' that is either set to 0 or 1. In a quantum computer, however, the memory bits can be in a linear superposition of states allowing them to encode multiple expressions simultaneously until collapsed by the act of reading them out. Quantum bits can have binary expressions encoded into them using any quantum mechanical observable as long as it possess two discrete states, such as the spin of a spin-1/2 particle.

So, in theory at least, this seems to have significant potential for N-body work. One may imagine a computer which can perform all the force calculations simultaneously or can hold the entire Hamiltonian of the system in memory at every point along its evolution. The problems arise when considering the practical limitations of the technique.

The most serious limitation is that there is no general 'quantum coding language' in the way that there is for classical computers. A classical computer is, essentially, a series of logic gates and we know that any other logic gate can be expressed as a linear series of NAND gates. This means that any problem that can be solved with a classical computer is equivalent to an arbitrarily large sequence of basic logic gates. The problem is that there is no simple equivalent of this fundamental building block in a quantum computer.

The operations that are carried out by a quantum computer must be constructed delicately so as to manipulate the superposition without destroying it, so even simple operations like basic arithmetic must be carried out according to very strict rules. As a result of the difficulty of manipulating quantum bits, there are only a limited number of quantum algorithms that exist.

The most famous example of a quantum algorithm is the factorisation of prime numbers (Shor, 1995) and a convenient list of other known algorithms is available at online resource [6]. The key point is that the options are extremely limited and it remains to be seen whether these can be combined to simulate a complicated enough code to run an N-body simulation.

Even if an algorithm could be created then there is a problem with the output. A quantum system only remains in a superposition until it is observed at which point it collapses into one state or the other which is the observed value. The problem is that once this happens, all other states of the system are lost. For example, an algorithm that tried

to use superposed states to encode information about multiple particles would fail as the computer would only return results for one calculation, destroying the information that was not read out.

Even if this could be circumvented then a more serious problem arises. By definition, when the superposition collapses it collapses from a combination of two possible states which means that the probability of either of these two states being ultimately observed will always be non-zero. In other words, while it is possible to encode the ‘answer’ to a mathematical problem into the states it is impossible to guarantee that *that* will be the particular state the system collapses to. To take a rather facetious example, if you asked a quantum calculator to solve ‘two plus two’ then it would only answer ‘four’ *most* of the time.

This is a well-known problem and unfortunately the solution is not ideal. As with any statistical event, the only way to find the ‘correct’ result is to measure the system repeatedly and look at the distribution of the answers it produces. The idea of running entire N-body simulations multiple times just to increase confidence in the result would seem to defeat any gains made by the algorithm itself. Unless some way is found that guarantees this error is comparable to the errors in modern, classical code then this may be the problem that kills the idea of quantum N-body codes.

After all of that, there is one further problem. Even if such an algorithm could be implemented, there are serious problems with the hardware. Quantum computers do not exist in any practical sense. The only devices that could be called such that are around today are experimental tests in research institutes (which require a room full of support equipment for a ten or so bits) or the adiabatic machines that are entering the market. Now, leaving aside the controversies surrounding the functionality of these commercially available adiabatic machines, an adiabatic computer is not *strictly* the same thing as a quantum computer.

In an adiabatic quantum computer the ‘question’ is encoded in the Hamiltonian of a quantum system. This is then lightly perturbed until it ends up in a configuration that can be read out as the ‘answer’. This process is incredibly sensitive as the system comes very close to leaving the ground state as the perturbations add energy and there is a real risk of corrupting the answer or destroying the system altogether if this occurs. While these

machines have potential, they are by no means a magic bullet.

In conclusion, quantum computers are exceptionally powerful, but only for certain types of problems. Only if N-body code is developed which can use only the known species of algorithms, require a small number of bits, and can overcome the read-out error will the field be able to effectively use them in the near future.

For now, we will leave these discussions and move on to a much more specific problem. Over the next chapters we will use this background of numerical codes to help us solve more problems in the phase-space of collisionless systems.

# 5

## Attractors, radial orbits, and statistical side-effects

*“Non-linear equations? Strange attractors? [Ellie shrugs] Dr. Sattler, I refuse to believe that you aren’t familiar with the concept of attraction.”*

*— Dr. Ian Malcolm, Jurassic Park*

As we have discussed in brief before, one of the ongoing problems in the field of galactic dynamics is the non-Keplerian nature of rotation curves in spiral galaxies (Salucci et al., 2007) and, consequently, the inferred presence of massive but undetectable structures enveloping the luminous component of galaxies. According to the prevailing cosmological model, known as  $\Lambda$ CDM, this structure is comprised of weakly-interacting particles which are known as Dark Matter (DM) which we discussed a few chapters previously.

The problematic word here is ‘undetectable’. DM, whatever it is, appears to have no coupling to electromagnetism and thus cannot be observed directly in an astronomical

context. It is possible to detect DM through direct collisions observed in terrestrial particle detectors, but such detections are extremely challenging and the search is ongoing. For our purposes, DM is an undetectable, collisionless form of matter that is found in halos surrounding baryonic structure.

Of particular interest is the density profiles of these halos as without insight into the gravitational potentials they create it is hard to make meaningful predictions of their effects. Cosmological N-body simulations and observed velocity profiles suggested early on that all stable halos should look like isothermal spheres that could be fit by some universal profile (Dubinski & Carlberg, 1991, and references therein). This is not entirely unexpected as the density profiles for stellar bulges are often parameterised using particular model families such as the Zhao (1996) models. The choice of model is determined by distribution of energy and angular momentum amongst the particles (Hernquist & Spiegel, 1992) and of particular importance is how particles exchange this energy and angular momentum. Additional characteristics are determined by mechanisms such as the dynamical friction/tidal disruption of subclumps and the absence or existence of an expanding cosmic background (Syer & White, 1998; Taylor & Navarro, 2001).

The particular profile of choice for DM analyses was later named the ‘NFW profile’ after Navarro et al. (1996) and found to be a two-power model with parameters  $\alpha = 1, \beta = 3$  as follows:

$$\rho(r) = \frac{\rho_0}{\left(\frac{r}{a}\right) \left(1 + \frac{r}{a}\right)^2} \quad (5.1)$$

where  $\rho_0$  and  $a$  are a chosen critical density and the scale radius of the model respectively.

Due to both the simplicity of the model and the apparent universality of the result, NFW profiles have become a very popular model for simulating halo characteristics. Because of this, it is vital that the ubiquity of the NFW profile be properly understood; the fact that it is *not* is perhaps a cause for concern since the universality of the profile has been called into question in the past by X-ray observations (Makino et al., 1998) and the Tully-Fisher relation (McGaugh & De Blok, 1998).

One potential problem is that the original study (Navarro et al., 1996) only selected fully equilibrated halos from the initial, low-resolution simulation for further detailed sim-

ulation. Subsequent investigations into the larger population have shown that while the profile is still a decent fit, even for non-equilibrium structures (Jing, 2000), there is evidence that a less global profiling system may have to be used instead (Host & Hansen, 2011).

Either way, the key point is that simulations of collisionless dynamics are vital for making predictions and understanding the mechanisms that go on inside DM halos. Additionally, any result that highlights an effect which could constrain dynamical behaviour, such as providing an actual reason *why* the NFW profile might describe every dark halo in the universe, is of particular importance.

The next two chapters will focus on recent work by Hansen et al. (2010) (hereafter HJS) where it was suggested that all collisionless systems will tend to move towards distributions drawn from narrow region of phase-space if they are gently perturbed from their current equilibrium and are allowed to find a new one. HJS used a simple algorithm to disturb a set of relaxed systems multiple times and observed, in each, a tendency for each successive equilibrium to converge to a particular region in phase-space.

Any N-body code must have its physical laws for such things programmed into it *a priori*, implying that those laws and their behavioural implications are well understood. This is why the discovery of a major and *unexpected* result like the identification of an attractor in the phase space of N-body systems is so remarkable. This is especially true since the attractor is a single-valued relationship between ostensibly independent parameters of the Jeans equation.

The work contained in the next two chapters was originally published in Barber et al. (2012) and Barber et al. (2014). The work has been restructured to present a better review for this thesis, however *all original results presented in this chapter and the next are drawn from these two published works unless cited otherwise*. In this chapter we will discuss the recreation of the HJS results, describe the codes and algorithms that underpin most of the work, and start to discuss the possible causes of the phenomena.

## 5.1 Attractors in the Jeans' parameter space

The Jeans equations (Jeans, 1915) describe the relationship between a density field,  $\nu(x, t)$ , a potential,  $\Phi(x, t)$  and the arrangement of velocity vectors in the system. Re-

call how we attempted to use them to find a stable system for the work back in chapter 2. In many cases there is not enough information to find a single, unique solution for an unknown component and one must accept a range of permitted solutions instead. For a spherical system with no net velocity, such as the ones used throughout this work, a useful form is the following:

$$v_c^2 = -\sigma_r^2(\gamma + \kappa + 2\beta) \quad (5.2)$$

where  $\sigma_r$  is the radial velocity dispersion,  $\sigma_t$  is the tangential velocity dispersion,  $v_c$  is the circular speed. Terms are defined as defined as follows:

$$v_c^2 = \frac{GM(< r)}{r}; \gamma = \frac{d \log \rho}{d \log r}; \kappa = \frac{d \log \sigma_r^2}{d \log r}; \beta = 1 - \frac{\sigma_t^2}{\sigma_r^2} \quad (5.3)$$

where  $M(< r)$  is the enclosed mass of the system. If only a couple of parameters are known exactly then there are countless configurations for which this equation will hold. It is this multiplicity that makes any convergent result so surprising; that in an almost limitless parameter space only one subset of configurations should be favoured. HJS found a strong link between the quantities  $\beta$  and  $\gamma + \kappa$  to which they fit an empirical relationship:

$$\beta = \frac{-0.15\gamma - 0.85\kappa}{(1 + (-0.15\gamma - 0.85\kappa)^3)^{\frac{1}{3}}} \quad (5.4)$$

which removes a degree of freedom from the system. HJS find that Eq. 5.4 is an ‘attractor’ *i.e.* a solution that systems will converge towards if they are free to move through the parameter space. Consequently, in order to observe evolution towards the attractor we need to perturb an initially equilibrated system in some physical meaningful way and see if it settles into equilibria which are successively closer to one particular solution. The perturbations consist of an alternating cycle of controlled, artificial perturbations acting in addition to the standard collisionless dynamics, referred to as ‘kicks’, with a subsequent period of relaxation to a new equilibrium state, referred to as the ‘flow’.

The attractor itself can be represented as a linear relation by plotting Eq. 5.4 as seen in Fig. 5.1. The data in this plot is taken from the final states of the simulations in HJS and it is this data which will provide us with our attractor curve throughout this work.

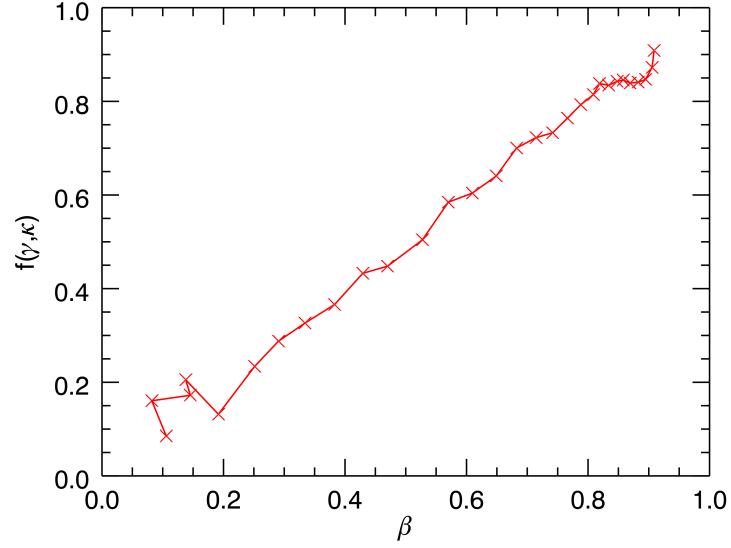


**Figure 5.1:** 1-D form of the attractor in the parameter space plotting HJS's data for  $\beta$  against the  $f(\gamma, \kappa)$  given in equation 5.4.

However, since this space is somewhat unintuitive, we shall usually plot the attractor in the more accessible parameter space of  $\beta$  versus  $\gamma + \kappa$ . In this space the attractor has a more complex 'S-bend' shape which will be seen in subsequent plots.

## 5.2 Initial conditions and numerical code

The process of perturbation and relaxation is carried out using N-body methods designed to replicate those used by HJS. Initial conditions are generated using the method outlined in Gerhard (1991). This approach is based on splitting the DF of the system,  $f(\mathcal{E}, L)$ , into two separate functions: an energy DF,  $f(\mathcal{E})$ , which controls how energy levels are populated and a circularity function,  $h(x) = h\left(\frac{L}{L_0 + L_{\text{circ}}(\mathcal{E})}\right)$ , which controls how circular the orbits of energy  $\mathcal{E}$  are. From these two functions one can directly produce functions for density and velocity dispersion necessary for building a Jeans'-stable system, for example:

$$\rho(r) = \frac{4\pi}{r^2} \int_0^{\psi(r)} d\mathcal{E} f(\mathcal{E}) [L_0 + L_c(\mathcal{E})] \left[ \int_0^{x_0(\mathcal{E})} \frac{x h(x) dx}{(x_0^2(\mathcal{E}, r, L_0) - x^2)^{\frac{1}{2}}} \right] \quad (5.5)$$

with comparable formulae for the velocity dispersions. Accordingly, a desired profile can be analytically generated by the appropriate choice  $h(x)$  and that profile can be randomly

populated by sampling the  $f(\mathcal{E}, L)$  via a Monte Carlo type method. The concepts involved in applying the above should be familiar from the discussions in the earlier chapters. We won't dwell further on the method except to note that, apart from a lamentable lack of analytical solutions, this method is one of the easiest and most flexible in producing models with the desired characteristics.

Our initial systems are Plummer spheres consisting of 750,000 particles with a combined mass of  $5 \times 10^8 M_{\odot}$ . We chose to only investigate one density profile in detail as it allows direct comparison of the effects of different perturbation schemes. Additionally HJS have already studied the impact of changing the initial density profile and found it has no effect.

Plummer spheres were chosen as they are derived from polytropic models and are thus formally unrelated to the NFW profile and are easy to create with varying anisotropies. We also used one special set of initial conditions designed to be, at any radius, more strongly radially anisotropic than the attractor. This system has a power law density gradient of  $r^{-2}$  throughout and a strongly radially anisotropic profile.

We make use of the N-body code NMODY (Ciotti et al., 2006; Londrillo & Nipoti, 2008), a particle mesh code capable of implementing MOND, for our numerical simulations. We have talked through NMODY in chapter 4 so just to refresh, NMODY uses an iterative scheme alongside a standard particle mesh to compute Newtonian forces and implements an extension to these for working in MOND as follows. The code first examines the density distribution and approximates it as an exact spherical solution, or takes the previous state of the system, as the starting point. The difference between the assumed density distribution and the actual distribution is assessed from the convergence between the acceleration field produced by the density and the field implied by the potential. When the two are, to within some user-defined accuracy, producing the same accelerations then that potential is used. The code then uses a standard leapfrog scheme to apply timesteps. For a full description of the code see Ciotti et al. (2006).

The ability to have simulations run in MOND is used to examine whether using a different form of Poisson's equation has any impact on the attractor. If the attractor is a gravitational effect then it would be expected to be inextricably linked to the description of gravity being assumed. With NMODY we can test whether this is true by altering the

equations governing gravity in our simulations and attempting to identify any impact this has on the attractor. Since implementing MOND requires just this kind of basic alteration, we can run simulations in the MOND paradigm to tell us whether or not the attractor depends on the equations of gravity based on whether or not the convergence is different.

We have reviewed the basic changes and consequences of MOND in a previous chapter so we will not do so again here, especially since we are only using MOND as a tool to alter Poisson's equation. We construct systems that run under three assumptions of gravity. We have purely Newtonian gravity with no MOND corrections, 'perturbative' or 'weak' MOND where the accelerations are high and the MONDian modifications are only a low order perturbation, and 'deep' or 'strong' MOND where the bulk of the system is in the low acceleration regime and the MOND effect is significant. In order to maintain the same density profile and total mass between all three scenarios while still operating in the relevant acceleration regimes, the scale radii of the models are bigger for models needing stronger MOND influence: Newtonian simulations use 0.05 kpc, weak MOND also uses 0.05 kpc, and deep MOND uses 1.0 kpc.

### 5.2.1 **Basic perturbation**

After choosing which model to use for our initial conditions (ICs) we define a simple algorithm that can provoke evolution towards the attractor. Our principle algorithm is taken from that used by HJS but with some minor differences. For example, our algorithm uses fixed-mass bins rather than fixed-radius bins and applies different factors to each velocity component rather than the same factor to all three.

The binning in the simulation allows us to define conservation laws for localised groups of particles in the simulations rather than only conserving over the simulation as a whole, softening the impact of the perturbation. By contrast, the binning performed later in the data analysis is needed to construct quantities such as velocity dispersion and anisotropy which have no meaning for single particles. For the simulation bins we choose to define bins as radial shells containing a fixed number of particles as it enables good statistics for the conservation laws in the outer edges of the system where number densities are lower.

We use a basic perturbation algorithm that is known to lead to the attractor in the standard case. Other, more specific schemes are employed to test various components of

the attractor's behaviour later on and they will explained in their respective sections.

- Set up a series of radial bins. We choose to create bins defined to contain 5,000 particles.
- For each particle in each bin we examine each of the three orthogonal velocity vectors and multiply each by a random number drawn from a uniform distribution centered around unity e.g.  $1 - 0.25 < f < 1 + 0.25$ . This is referred to as the 'shock' or 'perturbation' and  $f$  can be called the 'kick scale factor'. As a shorthand  $f$  is expressed as  $\pm n$ , so the previous example would be communicated as  $f = \pm 0.25$  for brevity.
- Make a choice about what quantities to conserve in the system. Here we shall only deal with energy conservation as there is no algorithm that can conserve both energy and angular momentum simultaneously without either failing to converge or introducing biases. An example of how to conserve angular momentum is given at the end of this section.
- To conserve energy, the energy in the bin is reassessed in order to re-scale all the velocity components equally to enforce conservation. Note that, since we are not altering particle positions, only the kinetic components before and after,  $T_{init}$  and  $T_{final}$ , need consideration:

$$v_{i,j,k} = v_{i,j,k} \sqrt{\frac{T_{init}}{T_{final}}} \quad (5.6)$$

- If a particle has been perturbed such that it is no longer bound in the system then it is re-randomised and the conservation algorithm is reapplied.
- Derive a dynamical timescale for the system

$$t_{dyn} = \sqrt{\frac{1}{G\rho}} \text{ where } \rho = \frac{0.95 \times M_{tot}}{\frac{4}{3}\pi r_{95\%}^3} \quad (5.7)$$

where we are using the 95<sup>th</sup> mass percentile as a representative distance for the edge system. For our initial systems this is equivalent to approximately 3 scale radii.

- The system is then left to evolve in an N-body simulator for at least 1 dynamical timescale. This ‘flow’ period allows the system to relax and find a new equilibrium. If we were to apply another shock too soon then the impact of the second shock would be indistinguishable from that of the first.
- The entire ‘shock-flow’ cycle is repeated 30 times.

If we wanted to conserve angular momentum instead then we could, for example, require the  $L_x$ ,  $L_y$  and  $L_z$  components of each bin to be equal before and after. The change in each momentum component from before and after the perturbation can be assessed and each particle given an equal share of that change,  $\delta L[x, y, z]$ , to compensate for. Dealing in Cartesian coordinates, each velocity component affects two momentum components which means that each velocity component has two pieces of information about how it must change to move towards conservation. The subsequent change made to the velocity component is an average of these two values. For example, for  $v_x$ :

$$v_x \rightarrow v_x - \frac{1}{2} \left[ \frac{\delta L_y |z|}{(|x| + |z|) z} + \frac{-\delta L_z |y|}{(|x| + |y|) y} \right] \quad (5.8)$$

with cyclical permutations for the other components. It can be shown that this approach rapidly converges to the correct global value. A qualitative explanation is that, in every circumstance, the two velocity components furthest from their required values will move to improve the two worst angular momentum offsets.

### 5.2.2 Analysis pipeline

Where possible, information about the system is taken directly from the ‘per-particle’ position and velocity file or the diagnostic output from the N-body simulation. To find expressions for local density and velocity dispersion the particles are interpolated over a spherical polar grid via the application of a linear smoothing kernel. The density can be found by looking at the total mass at each grid point and the velocity dispersion can be found the same way, although we weight the particles by their velocities while applying the smoothing kernel. Doing this smoothes the small scale noise that otherwise tends to dominate the dispersion. To find the radial profiles of these quantities we just average over the angular axes. Note that using a spherical polar grid means that our analysis bins are different to the simulation bins.

Gravity	IC $\beta$ profile	Kick scale/Sim. type	Flow time ( $T_{dyn}$ )
Newtonian	Isotropic	$\pm 0.5$	1
Newtonian	Isotropic	$\pm 0.5$	3
Newtonian	Isotropic	$\pm 1.0$	1
Newtonian	Isotropic	$\pm 1.0$	3
Newtonian	Radial	$\pm 0.5$	3
Newtonian	Tangential	$\pm 0.5$	3
Newtonian	Extremely radial	$\pm 0.5$	3
MONDian	Isotropic	$\pm 0.5$	3
MONDian	Radial	$\pm 0.5$	3
MONDian	Tangential	$\pm 0.5$	3
Deep MONDian	Isotropic	$\pm 0.5$	3
Newtonian	Isotropic	$\pm 0.5$ (spherical coord.)	3
Newtonian	Isotropic	Resolution test	3
Newtonian	Isotropic	Bimodal	3
Newtonian	Isotropic	Conserve L and E	1

**Table 5.1:** Overview of all simulations performed for this chapter. Non-standard kick scale factors are explained in the relevant sections.

### 5.3 The basic results

Various simulations are run which test various aspects of the attractor. Table 5.1 summarises, for clarity, what has been run and the order in which it will be discussed. Terms such as ‘bimodal kick’ are explained in detail in their relevant sections.

The first step before we begin any in-depth analyses is to assess whether it is reasonable to make a simplifying assumption about the sphericity of our systems. We would like to compress the full phase-space  $f(r, \theta, \phi, v_r, v_\theta, v_\phi)$  to  $f(r, v_r, v_t)$  according to spherical symmetry as we would like to assume the symmetries of both our IC’s and our perturbation algorithm. This is important as failure to account for lack of sphericity could cause the system to appear more isotropised than before.

This can be demonstrated by a simple 2-D thought experiment involving a flat disc with a population of particles at all radii in circular orbits. If we then take that system and stretch it along one axis by perfectly setting up an injection of radial velocity for every particle at the correct time we will end up with a set of elliptical orbits and a non-circular system. If we now place a circular mask over the system for a binning procedure and look at the orbits of the particles we will find a mix of radial and tangential motion. This will

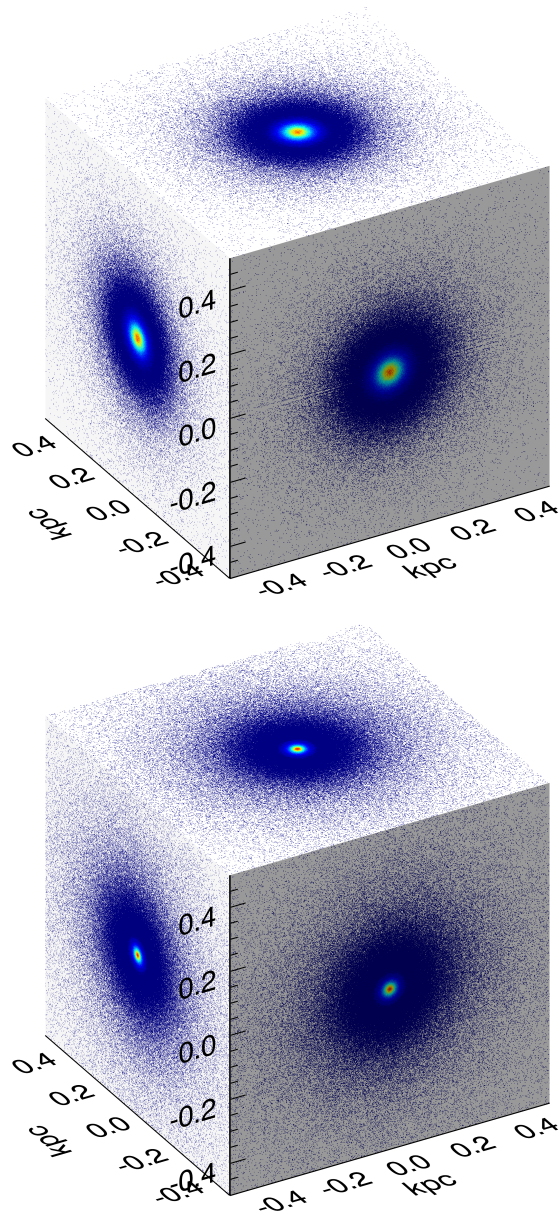


**Figure 5.2:** Model particle densities projected along orthogonal lines of sight into the system for both the initial conditions (top) and an evolved system (bottom). It is interesting to note the increased compaction of the core and the increased density particles at large radii which we will see, and properly quantify, as we continue through the chapter.

now look like a circular system with a confusing degree of anisotropy rather than like a very regular elliptical system.

So, first we must prove that our perturbations maintain the spatial symmetry of the model which we find in Fig. 5.2. In general, our algorithms take systems with axis ra-

tios of, for example, (1.0000, 1.0005, 1.0005) and, after 25 perturbations, return systems with axis ratios of (1.0000, 0.9945, 1.0167). These axis ratios are computed from measurements of the radii along each cartesian axis such that the density profile along the axis could produce half the system's total mass. Also note that the ratios are normalised against the x-axis.

In very rare instances we observe the development of triaxiality. This tends only to happen in our very dispersed, low density systems where the perturbation can cause rapid collapse. For example, the deep MOND simulations undergo a collapse and in only 5 perturbations the axis ratios change from (1.0000, 0.9991, 0.9992) to (1.0000, 0.8681, 1.3851). Overall our systems retain a high degree of spherical symmetry and in the rare cases where they do not we find that triaxiality is not the most pressing concern.

Next we check that it is reasonable to speak only of radial and tangential velocity. Since the vast majority of systems retain spherical symmetry there is no problem with defining  $v_r$  unambiguously leaving only the question of how to treat  $v_t$ . We only make extensive use of  $v_\theta$  and  $v_\phi$  to calculate the anisotropy where we only require them for the combined dispersion  $\sigma_t^2$  anyway.

These arguments show that it is perfectly valid to describe the system in terms of the limited parameter space thanks to the symmetries involved. Now we have proved this we can continue to our recreation of the results from HJS.

### 5.3.1 Effect of initial anisotropy profiles

Although Eq. 5.4 cannot be rearranged as a linear relationship between  $\beta$  and  $\gamma + \kappa$ , this is the parameter space in which the data is most easily visually interpreted. Consequently, it is awkward to use the parameter space of Eq. 5.4 to plot the attractor so we instead plot data from an exemplar converged solution from HJS as that is visually cleaner. This is why the attractor solution appears as a series of data points rather than a smooth, continuous function or allowed region. We first look at the simplest of our initial conditions, the isotropic Plummer sphere in Newtonian gravity.

In Fig. 5.3 the evolution of the system can be clearly seen. The initial condition is isotropic and is therefore a vertical sequence of points at  $\beta = 0$  with subsequent shocks apparently converging on a final state. The movement towards the end state is convergent

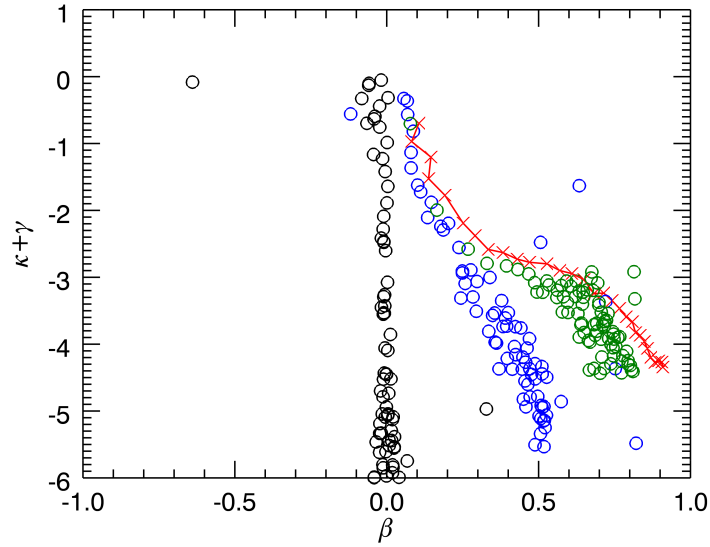


**Figure 5.3:** Evolution of the anisotropy profile of the isotropic Newtonian initial conditions at successive (0–black, 5–blue and 30–green) ‘shock-flow’ cycles with the attractor in red.

as successive shocks disrupt the previous equilibrium less and less until, at a point around 20-30 shock cycles, the system reaches a stable solution. This stable solution is a clustering of the bins around the attractor.

When interpreting plots such as Fig. 5.3 a useful rule of thumb is that higher values of  $\gamma + \kappa$  correspond to the inner regions of the system and more negative ones to the outer edges. This is not an exact relationship due to statistical noise and the opposing gradients of  $\rho(r)$  (increasingly negative) and  $\sigma_r^2(r)$  (increasingly positive), but is still be a useful approximation due to the domination of the  $\gamma$  term. This tells us that the change in anisotropy is more significant at large radii.

Next we test if an initially anisotropic model affects the evolution towards the attractor given that the attractor drives the anisotropy profile. The anisotropy in the initial condition is visible in Fig. 5.4 as a gradient in the initial data points. Once again the convergence is very apparent after 30 cycles. This implies that the emergence of the attractor is robust to the initial anisotropy of the halo although tangential models take longer to converge as the change in anisotropy needed is greater.

Finally we try conditions that are significantly more radially anisotropic than the at-

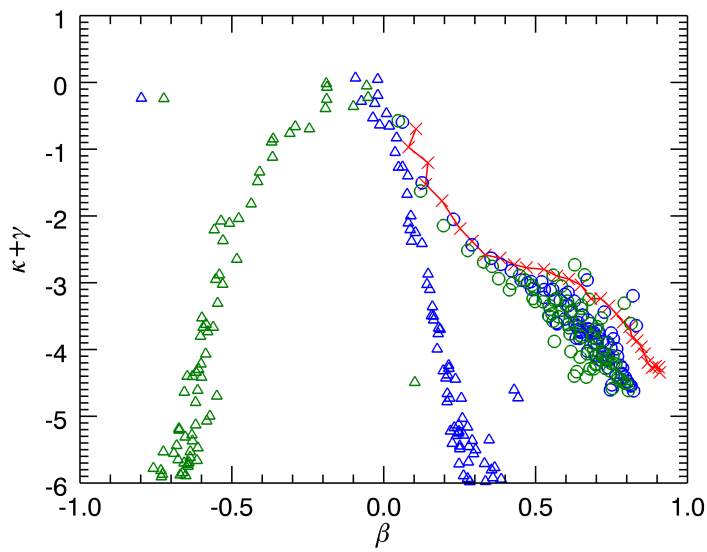


**Figure 5.4:** Initial (triangles) and final (circles) states for radial (blue) and tangential (green) initial conditions after evolution under our perturbation scheme.

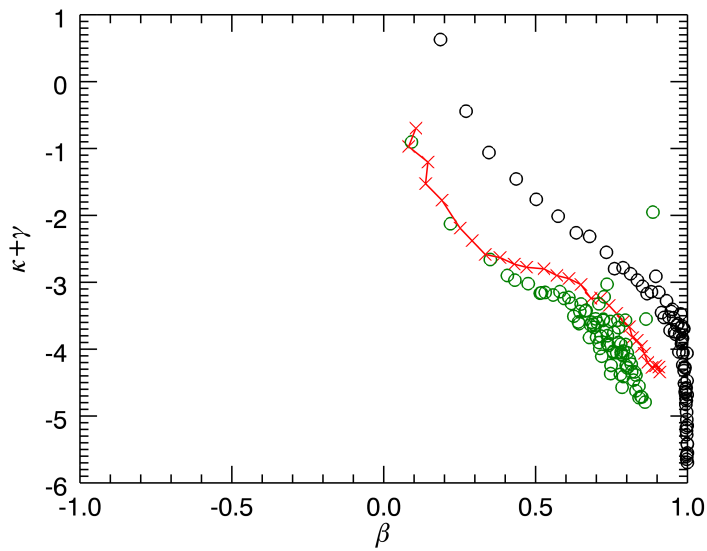


**Figure 5.5:** Initial (black) and final (green) states for a system that is more radially anisotropic than the attractor

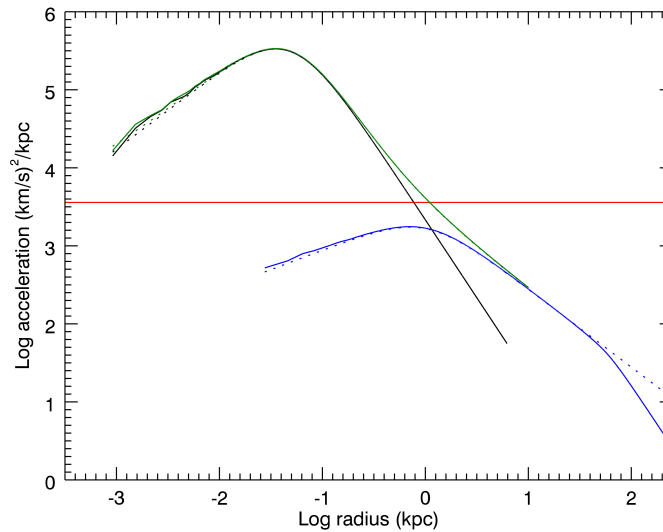


**Figure 5.6:** Initial curves of the numerical acceleration (solid lines) compared to the theoretical values (dotted lines). The models shown are Newtonian (black), ‘perturbative’ MOND (green) and deep MOND (blue). The region below the red line represents low enough acceleration that MOND effects become roughly of order unity. This corresponds to an acceleration of  $a_0 < 3600 \text{ km}^2 \text{ s}^{-2} \text{ kpc}^{-1}$ .

tractor at all radii. This model also converges to the attractor just as the others do, as shown in Fig. 5.5.

### 5.3.2 Effect of gravity theory

If the attractor is a phenomenon strongly tied, as one might reasonably expect, to gravitational laws then changing the form of those laws may have some impact on the evolution of the system. Accordingly, simulations were run where the initial conditions and subsequent evolution of the system were carried out under a different assumed theory of gravity.

We test two variations of MONDian dynamics using the same perturbations as before. The first model is a perturbative one where systems of comparable scale to those seen so far are simply translated to their stable MOND equivalents with MONDian effects only influencing the outer regions. The second is an extended system of the same mass where the entire system is in the MONDian regime. The scales and changes are shown in Fig. 5.6.

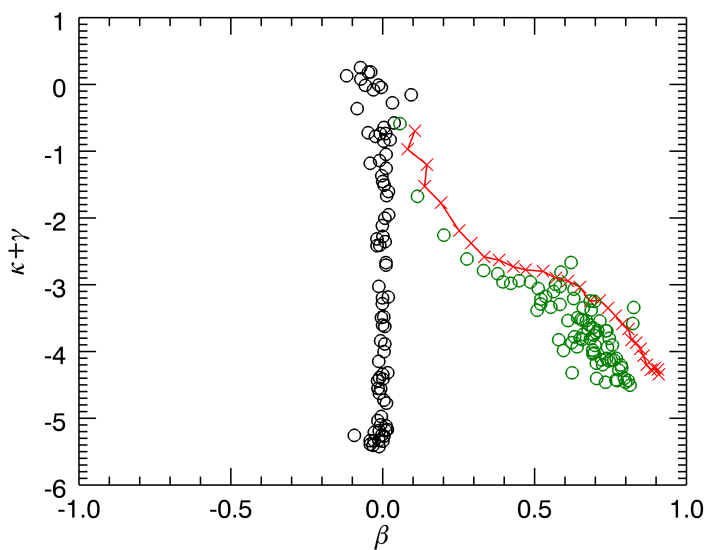


**Figure 5.7:** The evolution of the isotropic perturbative MOND model. As before the initial points are in black and the final points are in green.

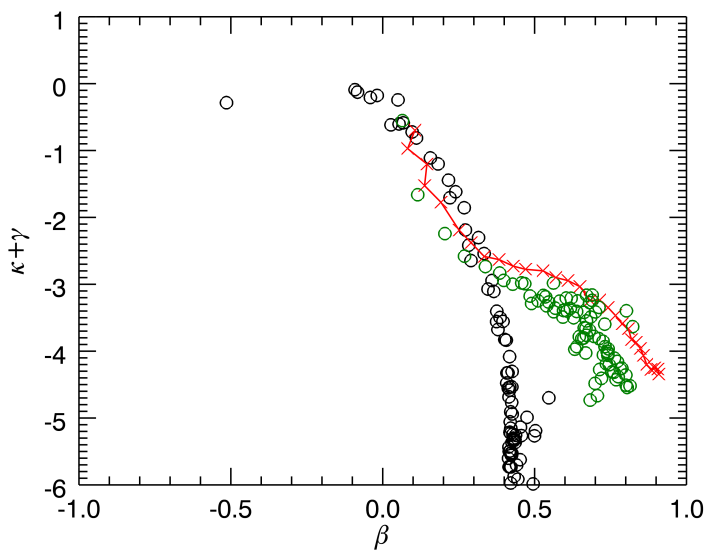


**Figure 5.8:** The evolution of the radially anisotropic perturbative MOND model. As before the initial points are in black and the final points are in green.

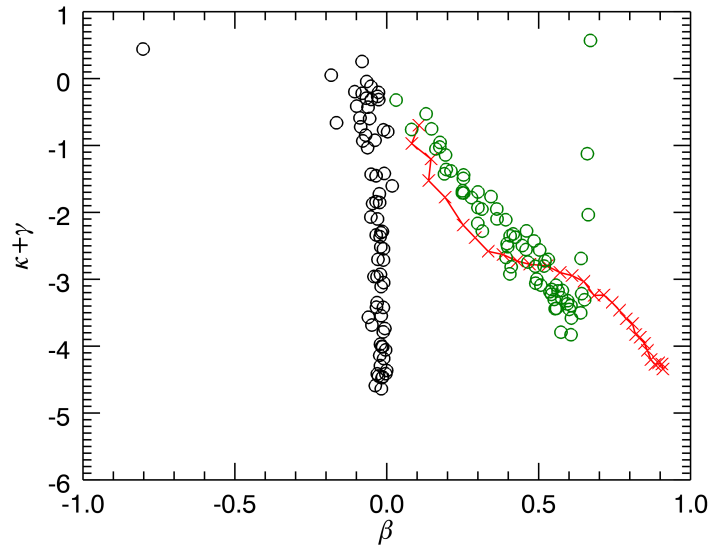


**Figure 5.9:** The evolution of the deep MONDian model. Initial points are black and final points are green.

The change to a MONDian Poisson's equation has no noticeable impact on the evolution of the system as both the isotropic and radially anisotropic models, seen in Figs. 5.7 and 5.8 respectively, converge. The convergent solution is the same as in the previous Newtonian simulations and emerges over the same timescale which is not unexpected since the MOND effect in these systems is only slight.

When we look at the behaviour of the larger, deep MOND system we still see significant movement towards the attractor as shown in Fig. 5.9. This plot is not as clear as previous ones due to both the increased statistical noise from the larger characteristic radii and the collapse of the system leading to mild triaxiality as mentioned previously. The tendency for collapse is interesting in its own right and will be discussed in more detail in the next chapter as it is present to some extent in all systems perturbed in this manner. For now it is enough to see that this system still evolves towards the attractor.

We would not expect that the deep MOND regime would cause any significantly different behaviour from the weak MOND regime due to this tendency of our perturbation method to cause a degree of contraction in the system to which it is applied. In this case the collapse concentrates the mass and so most of the mass in the system exits the deep MOND regime. This contraction is shown in Fig. 5.10.

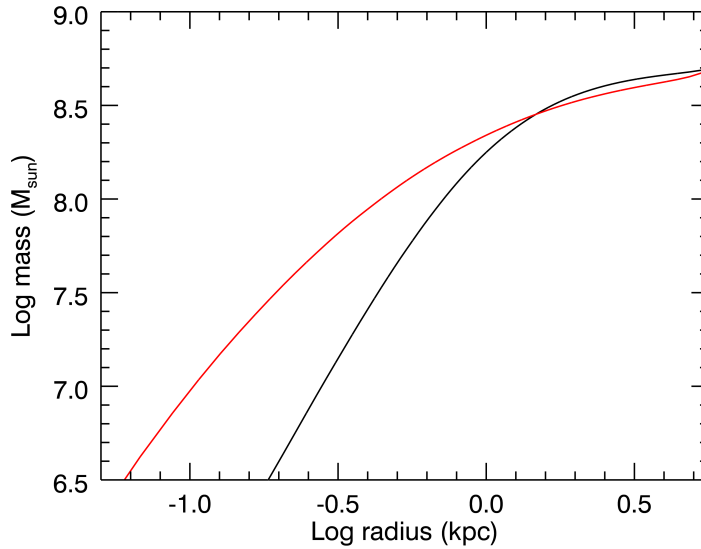


**Figure 5.10:** A section of the enclosed mass profile to demonstrate the collapse of the deep MOND system after only 5 perturbations (red) compared to the initial mass profile (black).

We see that there is remarkable agreement amongst the simulations as they have all converged towards a single solution. This gives us clear evidence for convergence to the same attractor as that found by HJS. This implies that the details of the gravitational interactions between particles are not especially important to the attractor. This makes sense when viewed the same way as the HJS results whereby the flow allows for the phase-mixing of the system. One would not expect small changes to gravitational coupling to have any significant impact on the system's ability to phase-mix and, indeed, this seems to be what we find. Next we attempt to disrupt the convergence by altering the algorithm we have been using.

### 5.3.3 Changing implicit coordinate system

The perturbation algorithm that we use has dealt with velocity vectors in a cartesian coordinate space. However, since we are also interested in whether or not the attractor is related to the perturbation algorithm itself, it is important to check if the attractor is independent of the coordinate system. The Newtonian, isotropic system was re-run but the random scaling of velocity vectors  $v_{[x,y,z]}$  was carried out on  $v_{[r,\theta,\phi]}$  instead. When the velocities are converted back into Cartesian axes the scaling will no longer be uniform or

obey the same limits due to the non-linear and interconnected nature of the transforms used *i.e.*:

$$\dot{r} = \frac{x\dot{x} + y\dot{y} + z\dot{z}}{\sqrt{x^2 + y^2 + z^2}} \iff \dot{x} = r \left( \cos(\theta) \cos(\phi)\dot{\theta} - \sin(\theta) \sin(\phi)\dot{\phi} \right) \quad (5.9)$$

We find that the move from Cartesian to spherical coordinates has no effect on the convergent solution. This is consistent with the findings of HJS where they tested different values for the random factor used to scale the velocities.

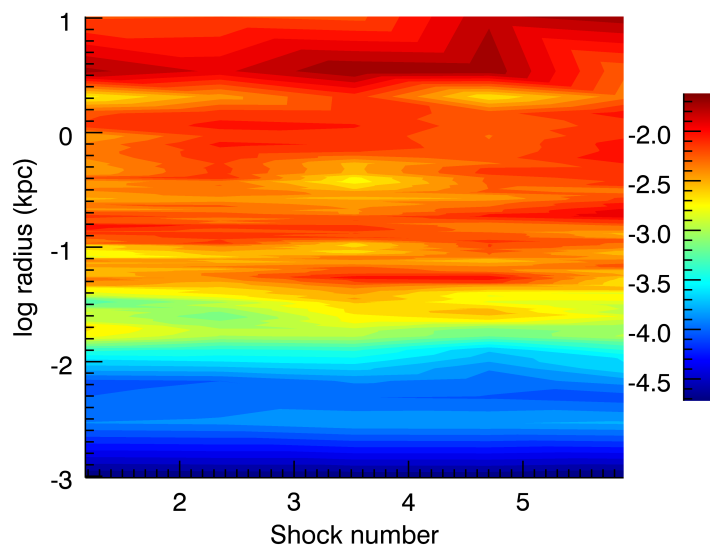
### 5.3.4 Random scale factors and flow time

In order to talk quantitatively about the speed of convergence and to demonstrate that the systems have actually reached a convergent state we need to define the convergence. Since the evolution of the system is most clearly seen in the changing of the anisotropy profile we choose to quantify the convergence by comparing the anisotropy profiles before and after a kick-flow cycle. This is then compared against the changes in anisotropy caused by statistical noise in an unperturbed, equilibrium system.

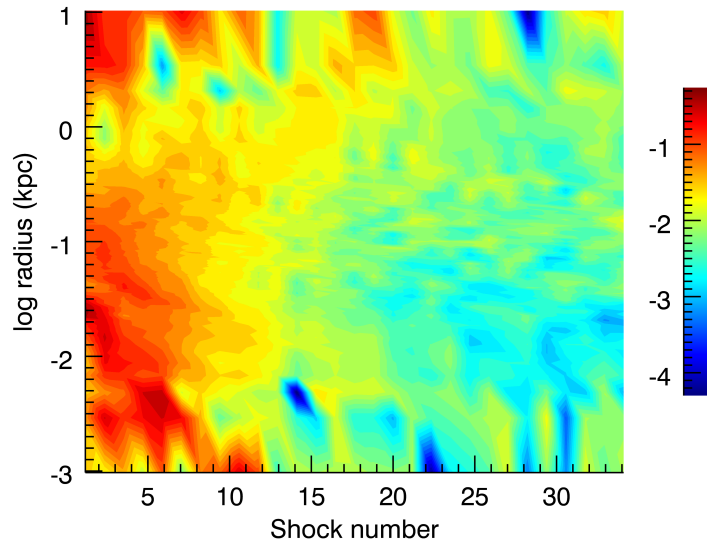
This is visualised in Fig. 5.11 where, at every radius, the change in anisotropy between successive shocks is plotted and then smoothed into contours. Fig. 5.11 is a control plot which shows the changes in the anisotropy of the isotropic Newtonian IC's when no shocks are applied. Note that since the changes in anisotropy are expressed clearest as logarithms the change being evaluated is  $\log |\beta_f - \beta_i|$ .

Fig. 5.11 shows us that the equilibrated central regions are extremely stable with fluctuations in anisotropy of order  $\pm 10^{-4}$ . This increases a little at large radii to approximately  $\pm 10^{-2}$ . Thus we can define convergence in terms of a change in beta that is less than or equal to the change at the same radius in the unperturbed system using Fig. 5.11.

In practice, we do not expect such precise stability in our perturbed systems even when they are on the attractor. Even if the attractor does present a favoured configuration then, as we have discussed, the Jeans' equation still permits a degree of variation in the densities and dispersions that will fit it. Additionally, the analysis which produces these plots uses bins of fixed radius meaning that the small changes in the density profile caused by the perturbation are a source of noise not present in the control system. Consequently,



**Figure 5.11:** The changes in anisotropy in a stable, unperturbed system. Note that since the changes in anisotropy are expressed clearest as logarithms the change being evaluated is  $\log |\beta_f - \beta_i|$ . The ‘shocks’ listed on the x-axis are only marked for comparison with plots where shocks *were* actually applied. Here the ‘shocks’ just mark intervals of  $1 T_{dyn}$ . *Note the difference in scale from Fig. 5.12*



**Figure 5.12:** The logarithmic changes in anisotropy between kicks of over 30 kicks to the Newtonian, isotropic system. *Note the difference in scale from Fig. 5.11*

these plots will principally be used to find when the changes in anisotropy become roughly constant at some radius and when the magnitude of fluctuation is roughly of the same order as the control.

Noting that the colour scales of the two plots are different, we see that after 30 kicks the system shown in Fig. 5.12 is very stably converged. The fluctuations in the outer edges of the system are very close to the control while the central regions are a little more unstable inside of 0.01 kpc, with instants when the system is as stable as the control. It is very clear that the change in anisotropy has dropped by several orders of magnitude between kicks. This indicates that the system has evolved as much as it is going to and similar plots for our other systems demonstrate that they are also fully converged.

As noted previously there is a lot of freedom in designing perturbation algorithms. In particular we have yet to discuss the freedom allowed in the ranges of certain critical parameters such as the range of the scaling factor and the length of time allowed for the flow phase. In order to examine the effect of certain parameter choices on the progression of our simulations we ran four simulations using different combinations of scaling factors and flow times and then stopped them after only a few perturbations. We can then see which simulations have evolved furthest in that time and which are slower. We stop the

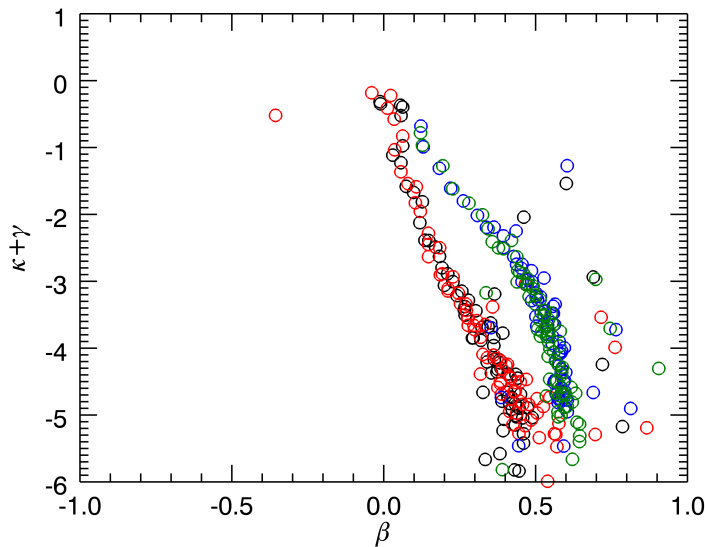


**Figure 5.13:** Attractor plots for four different combinations of algorithm parameters after 4 kicks. The systems use scaling factors of  $0.5 < f < 1.5$  with 1 (black) and 3 (red) dynamical times for the flow and  $0.0 < f < 2.0$  with 1 (blue) and 3 (green) dynamical times.

simulations before they reach the attractor because by the time they are converged all the systems will be lying on top of each other anyway and any differences in their progression to that point would be lost.

Looking at Fig. 5.13 we can see why it is important to thoroughly examine the choice of algorithm as some parameters have a significant impact while others do not. For example, we show here that allowing the system to equilibrate for longer periods of time has almost no effect on the speed of convergence. This is slightly counter to expectations but amply demonstrates the stability of the intermediate solutions, the necessity of repeated perturbations, and the special nature of the final point of convergence. In our scheme we see that the most important factor is the range of the kick scaling factor with larger kicks promoting significantly faster convergence.

## 5.4 Impact of numerical resolution effects

One area of major concern is the possibility of a connection between the attractor and the numerical resolution of our simulations; the suggestion being that our conclusions were heavily influenced by numerical artefacts rather than the physics of the system. Of

specific concern was whether the behaviour being described could be caused by collisional relaxation and would thus be governed by the softening length of the simulation.

NMODY uses a self-consistent field (SCF) method similar to that described in Hernquist & Ostriker (1992) *i.e.* it describes the potential and density by expanding them into a series of terms of some basis function. Ciotti et al. (2006) is mainly concerned with demonstrating accurate recovery of MONDian potential-density pairs via this method and thus does not spend time looking at the impact of resolution explicitly. However, the two methods are sufficiently similar that informative results can still be found by examining the impact of numerical resolution in the Hernquist & Ostriker (1992) method.

This work showed, for a variety of initial density models, that the relative importance of each subsequent term in the basis series decreases exponentially. For Plummer models such as ours the method provides better than 1% accuracy, in terms of orbit conservation, when using around 5 terms in the series. It is noted that cored models, such as a Plummer sphere, can be particularly well described by this kind of expansion method if the basis functions are chosen appropriately.

Having demonstrated the accuracy of the method, Hernquist & Ostriker (1992) examines the emergence of collisional relaxation in the simulation. As there is no explicit softening length used in the method they note that an SCF code should not suffer from limitations on spatial resolution and can, in principle, resolve much steeper density gradients than other methods. Overall, from the conclusion of this paper, we expect that a code such as NMODY would be efficient at suppressing collisional effects as only a handful of basis terms are required to provide ample spatial resolution for the simulation.

With this in mind several supplementary simulations were run to explicitly examine the impact of smoothing lengths and resolution by applying one of two categories; rougher or smoother models, *cf.* Fig. 5.14.

Rougher models lowered the resolution of the model in two ways. Firstly, when the code developed the spherical harmonics that described the potential, twice the number of terms in the series were used making the potential more variable on shorter scales and thus magnifying the effect of short distance interactions. This approach was used rather than simply changing the smoothing length because, as previously discussed, NMODY does not support the direct selection of a smoothing length due to the SCF scheme.

Secondly, the initial conditions were the same isotropic Newtonian model with the same total mass, but now using half the number of particles. This preserved the dynamical timescale of the system while also making the particle distribution noisier. Overall, we would expect the combination of these two effects to emphasise any effects from collisions and, if they are driving the attractor, to lead to the attractor faster.

Smoother simulations used the same reasoning except they halved the number of terms in the harmonics which smooths out perturbations on short length scales. They also had double the number of particles modelling the system which smooths the distribution overall. If artificial numerical collisions were governing the attractor, then the de-emphasis of short scale interactions and the smoother particle distribution should suppress the effect.

Overall, these rough/smooth schemes allow us to control the resolution and susceptibility of the system to collisional effects and short-scale interactions while retaining comparable simulations that, as a practical benefit, require comparable amounts of processing time to yield results.

To demonstrate this, we present Fig. 5.14 which shows the state of three comparable simulations 10 kick-flow cycles *i.e.* 10 perturbing events spaced evenly throughout a total simulation time of 30 dynamical times, into their evolution. This is approximately one third of the time required for the systems to reach the attractor, according to our previous simulations, and demonstrates that the systems are indistinguishable from each other in terms of the parameter space they occupy. Our simulations eventually end up lying in the parameter space of the attractor in a manner indistinguishable from the results from any other converged model. In particular we establish that the behaviour is preserved down to the speed at which the convergence occurs.

The same rougher/smooth dichotomic scheme was also applied to a new perturbation method that performs systematic alterations to the system's velocity anisotropy profile. This new perturbation method will be explained in detail in the next chapter and it is mentioned here only to make clear that it also appears unaffected by alterations to the smoothing.

In summary, the attractor effect is demonstrated to progress the same regardless of the number density of the system or how accurately the simulation models short-scale behaviour. Additionally, the attractor is present in simulations that use different codes

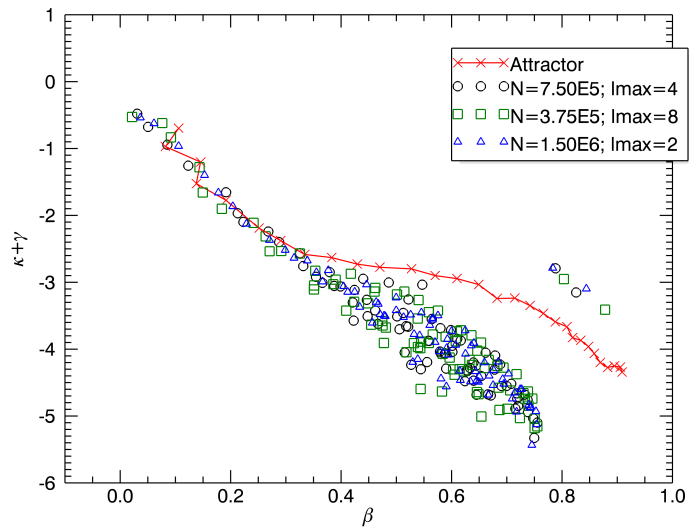


**Figure 5.14:** Attractor plot demonstrating that the importance of two-body interactions is negligible. It shows the state of three simulations approximately one third (in terms of elapsed time) of the way towards convergence on the attractor (red line). All three use a kick with scaling factor  $\pm 0.5$  and  $3T_{dyn}$  flow time per kick. Our benchmark isotropic Newtonian simulation (black circles) overlaps comfortably with both the rougher (green squares) and smoother (blue triangles) bins of the newer simulations demonstrating a very similar rate of convergence. This shows that the evolution of our systems towards the attractor, which is where they eventually rest, is unaffected by the resolution of the simulations and, consequently, by collisional effects.

(Hansen et al. (2010) used GADGET-2 which has a different architecture to NMODY) to solve for the particles motions. Accordingly, it is not thought that the attractor shares any significant causal link to collisional relaxation or any effect deriving from two-body interactions.

## 5.5 Condensing the method — bimodal perturbation

So far we have several clues as to what causes the convergent behaviour. We know that the characteristics of the initial system and the environment have no effect and that altering the constants used in the perturbation changes only the intermediate steps and not the final convergence. Using the fact that, as seen in §5.3.4, changing the amount of time allowed for the flow phase has a minimal impact on the rate of convergence we can suppose that the flow phase only acts to allow the system to find the nearest Jeans'-stable state and does not contribute to the attractor itself beyond some small amount of settling. We might then ask if the attractor is caused primarily by the repeated action of the perturbation scheme and whether the attractor represents the closest Jeans'-stable state to some limiting point for the perturbation scheme.

One potential insight into this comes from the realisation that all of our algorithms are special cases of a broader class of perturbation which always gives rise to the same behaviour for well-understood reasons. First, we will run down the various permutations of the algorithm and show they all accomplish the same thing and can be thought of as being related. After establishing that one particular algorithm can be used to represent all of the other variants tested so far we will show why we would expect this algorithm to lead to some convergent state.

As we have previously discussed, the decision to implement a perturbation that applies *different* factors on each velocity component has the principal effect of slowing down the convergence as the shock is not as strong as that provided by a similar scheme that uses the *same* factor for all three. However, apart from this difference in convergence rate the algorithms have the same effect and the same underlying principle and thus the former perturbation can be thought of as being a special case of the latter.

Now imagine a fairly weak perturbation (of the latter variety) where  $0.75 < f < 1.25$  and consider the effect of applying this perturbation  $n$  times in succession whilst allowing

no opportunity for relaxation in between. We can see that, statistically, a small population will feel a perturbation of  $0.75^n < f < 1.25^n$  which will correspond to a more pronounced perturbation. We then posit a limiting case for these perturbations where  $n$  cycles of any given perturbation will eventually have roughly the impact of a single perturbation where  $\sim 0 < f < \sim 2$ . This corresponds to the strongest perturbation that we have employed so far and the strongest possible symmetric perturbation.

So, all perturbations of the form  $1 - C < f < 1 + C$  can be thought of as reducing to  $0 < f < (1 + C)^n$  over a sufficient number of iterations. Now we apply the same line of thinking and ask what multiple applications of this algorithm reduce to. In this instance, a small population of particles will end up with velocities of almost zero while a small population will experience a significant increase. When we apply this algorithm multiple times we can not significantly change the energy in the population where  $v \approx 0$  as the most that can happen is the particle's already meagre velocity is doubled and at worst it can be set to exactly zero. Statistically we will also add some particles to this population by scaling a few high energy particles by 0. This means that every time we perform the perturbation we increase the size of the low speed population while, in order to obey energy conservation, we must pump more and more energy into a small population of particles which eventually become unbound.

This line of reasoning shows the limiting case for all of these perturbation schemes is that a large population undergoes radial infall as their energy is slowly sapped away and fed into a smaller population of particles on high energy orbits that form an envelope. This is supported by previous evidence showing an increase in central density even as the outer edges of the bound system move further and further out. To test this limit directly we implement an algorithm that forces a bimodal scaling where particles are either immediately put into radial infall by having their speed set to almost zero or are boosted into the high energy envelope. An example of such a perturbation could be that 90% of the particles are induced to radial-infall but the remaining 10% envelope has many times its original energy in order to make up conservation.

The algorithm was designed to either induce radial infall or set the particle traveling at its escape speed in such a way that, in the statistical limit, energy conservation is implied. So that the radial infall is not too perfect and allows for the pre-existing velocity dispersion

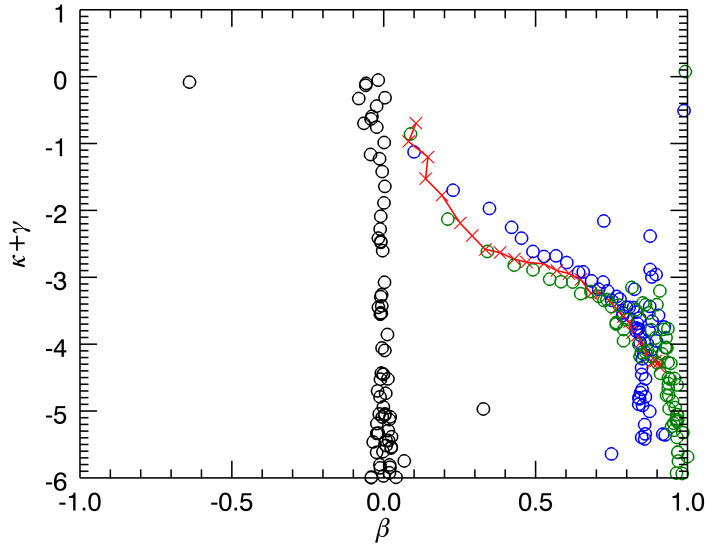


**Figure 5.15:** The immediate and significant impact of using the bimodal algorithm on the initial isotropic system (black), the system after only *one* perturbation (blue) and after two perturbations (green)

to have an effect we set the lower limit to be non-zero, but still small, and label it  $s$ . We choose a value of  $s = 0.01$ .

$$\text{where } f = \frac{1 - \frac{v_{old}^2}{v_{esc}^2}}{1 - s \frac{v_{old}^2}{v_{esc}^2}} \quad (5.10)$$

$$v_{new} = v_{old} \times \begin{cases} \sqrt{\frac{1-f \cdot s}{1-f}} & \text{if } rand_u[0, 1] > f \\ s & \text{if } rand_u[0, 1] < f \end{cases} \quad (5.11)$$

What we see in Fig. 5.15 is striking. After only one perturbation the system is almost exactly on top of the attractor and only one perturbation later the system has completely converged. It is interesting that the system appears to ‘overshoot’ the attractor after the first perturbation and only settle onto it after the second kick. This is possibly because the initial perturbation is so unrealistically violent that it simply takes longer than the allowed  $3 T_{dyn}$  to equilibrate.

This suggests that the prior line of reasoning is valid in so far as all perturbation algorithms that we have dealt with so far are actually special, slower cases of the bimodal

scheme and that the attractor can be generated simply by forcing the system to undergo our radial-infall-plus-ejection scheme and then letting the system become Jeans' stable again.

This gives us a potential explanation for why the initial anisotropy profile and theory of gravity do not affect the attractor under such perturbation schemes. Initial anisotropy does not matter as the perturbation destroys part of that information with every successive perturbation by, in the above limit, putting all the particles on highly radial orbits by either catapulting them out to the edges of the system or by instantaneously removing all kinetic energy. Gravity makes no difference as the attractor is formed by radial infall which is not a behaviour that is heavily dependent on the specifics of the theory of gravity being assumed.

This also explains a particular result from HJS where a perturbation acting only on the radial velocity components will not lead to convergence whereas one that acts only on the tangential components will. In the tangential-only case, we can take the limiting cases where the particle ends up with no angular momentum and ends up on a purely radial orbit or is boosted onto a highly elliptical orbit. This picture is very similar to the infall mechanism and thus the same outcome is to be expected. However, if only the radial components are changed then the angular momentum of the particle cannot be removed. This means we have the same high energy limiting case but now the low energy limiting case is a circular orbit. This leads to a very radial outer envelope, as before, but a distinct tangential anisotropy in the nucleus regions that can be seen as a distinct 'S-bend' shape in the anisotropy curve.

This kind of behaviour emerges in any code with a strong built-in radial bias. The results in Fig. 5.16 come from runs which attempted to conserve both angular momentum and kinetic energy. After conserving angular momentum the only way to conserve energy is to only alter the radial velocity component of each particle so as not to disturb the angular momentum. However, simple iteration towards some unrestricted and fully self-consistent solution can not guarantee consistency and results in a very forced perturbation that places too great a restriction on the range of possible equilibrium solutions.

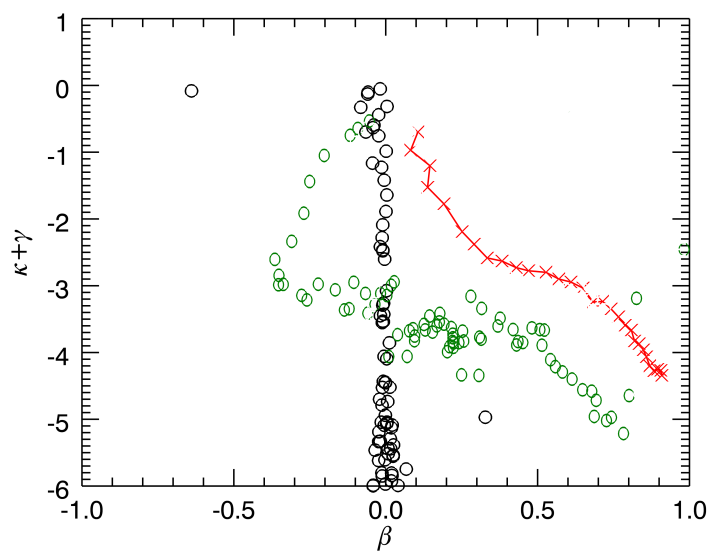


**Figure 5.16:** An attempt at reproducing the results from HJS using an early algorithm that attempted to conserve both energy and angular momentum. As per usual the red points are the attractor, the black are the initial conditions, and the green are after 30 perturbations. The altered shape of the converged solution is due to a strong radial bias in the perturbation algorithm.

## 5.6 Connection to radial orbit instability

In the previous section we have shown that the perturbation schemes being used all appear to reduce the attractor to a matter of placing particles on infalling orbits. One of the dangers of placing a large population of particles on highly radial orbits is that the system becomes susceptible to the radial orbits instability (ROI) which can produce a set of very well constrained behaviours. In fact, these behaviours are so regular and predictable that much work has already been done to determine whether ROI is the explanation for the universality of the NFW profile in dark matter halos (Macmillan & Henriksen, 2006; Bellovary et al., 2008; Lapi & Cavaliere, 2011). As part of that endeavour, several universal profiles and convergent behaviours have been identified.

The following behaviours are not all completely exclusive to ROI but they are all symptomatic of highly radial systems and the kinds of radial infall that our models undergo. However, ROI is still the primary mechanism which relates these effects and as such we shall concentrate on their connection to it.

Before continuing it is important to note that the mechanism we cause is not identical to ROI. These models start off stable and have a wide variety of anisotropies and only become radial as a result of this forced collapse. In this sense, we ignore the initial susceptibility of the system to ROI and would thus expect the effect to emerge more gradually as the system is perturbed. We suggest that this is why our systems do not display the high degree of triaxiality that is normally associated with ROI-unstable systems (Antonov, 1973; Barnes et al., 2009). As we showed in §5.3 our models generally maintain equal axis ratios apart from the systems that are more dispersed. Interestingly the more dispersed system also undergo a more significant amount of collapse so it is also possible that the development of triaxiality in *these* systems is not caused by noise, as previously suggested, but ROI.

### 5.6.1 Universal anisotropy profiles

In many simulations of ROI unstable systems it was observed that the anisotropy profiles of the final systems would tend to cluster around a common profile. This profile was more complex than a pure power-law (Bellovary et al., 2008; Lapi & Cavaliere, 2011) and displayed an isotropic nucleus that rises smoothly to radial anisotropy in the outer

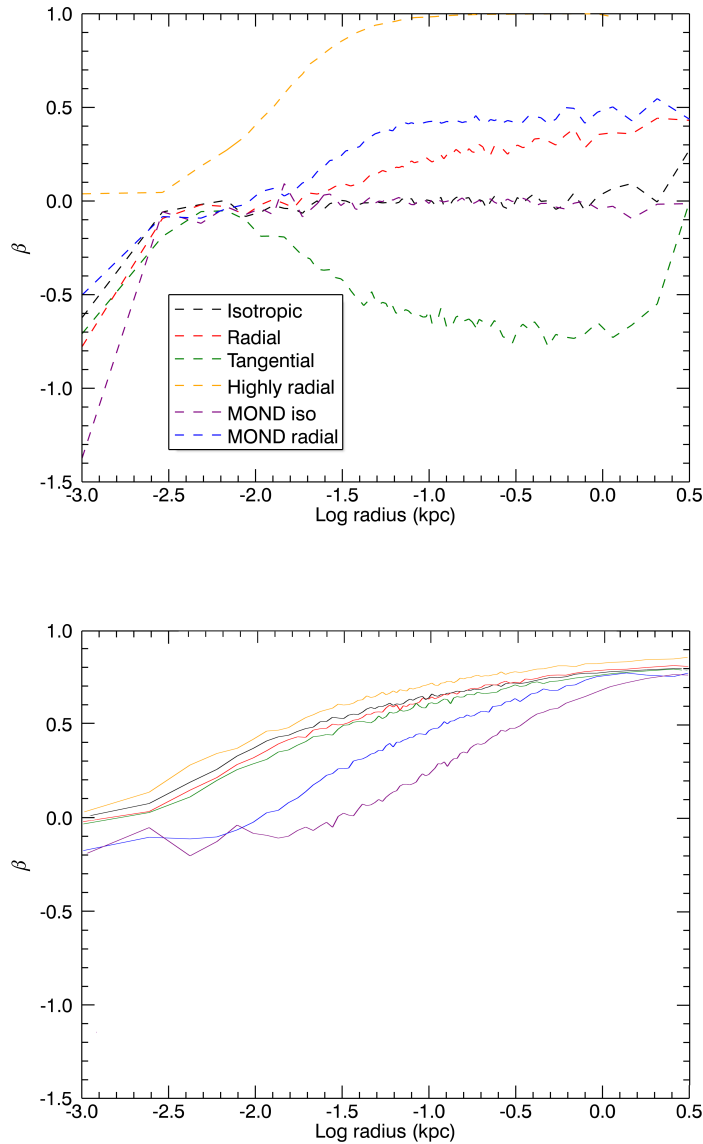


**Figure 5.17:** Evolution of the anisotropy profile in the Newtonian isotropic (black), radial (red), tangential (green) and extremely radial (orange) models as well as the MONDian isotropic (purple) and radial (blue) models from their initial states (dashed/top) to their final states (solid/bottom).

edges in a similar manner to the attractor. There is some tolerance within this, however, as Bellovary et al. (2008) found that the initial anisotropy profile did leave a lingering impression on the final profile.

We also find good convergence among the Newtonian simulations although we note that the MOND simulations stand out somewhat in Fig. 5.17. The very radial initial

conditions also stand apart from the others although this is still consistent with ROI.

### 5.6.2 Convergence of $\rho/\sigma^3$

One important result, although not one exclusive to ROI, was that systems formed by mergers (such as DM halos) display convergence in a quantity that proxies for the phase-space density (Taylor & Navarro, 2001; Dehnen & McLaughlin, 2005). This quantity is  $\rho/\sigma^3$  and it is found that it quite precisely follows a power-law:

$$\frac{\rho}{\sigma_r^3} \propto r^{-1.9} \quad (5.12)$$

As noted in those papers, the peculiar thing about this convergence is that neither  $\rho$  nor  $\sigma_r^3$  are themselves individually convergent to a power-law. However, the significance of this quantity does suggest that there may be some connection between it and our  $\gamma + \kappa$  axis. In Fig. 5.18 we investigate whether our simulations develop the same power-law during convergence.

Fig. 5.18 shows us firstly that all the models start off with very similar phase-space density profiles with the exception of the extremely radial case. However, *all* the Newtonian models evolve towards  $r^{-1.9}$  as per Eq. 5.12 and end up with profiles that are even closer together than when they began. Standing out from this close convergence is, once again, the extremely radial case which ends up with a  $r^{-1.9}$  power-law but a significantly offset from the other system. Also interesting is that this high degree of clustering is largely absent from the MONDian profiles, which retain good agreement with each other but barely evolve from their initial conditions.

This shows that our perturbation, developed from HJS's attempt to simplify the modelling of halo mergers, does seem to display some characteristics of a system that has undergone repeated mergers. Accordingly, we may use this power-law as a possible avenue of investigation into our attractor formula, particularly in light of the notable connections to the next result.

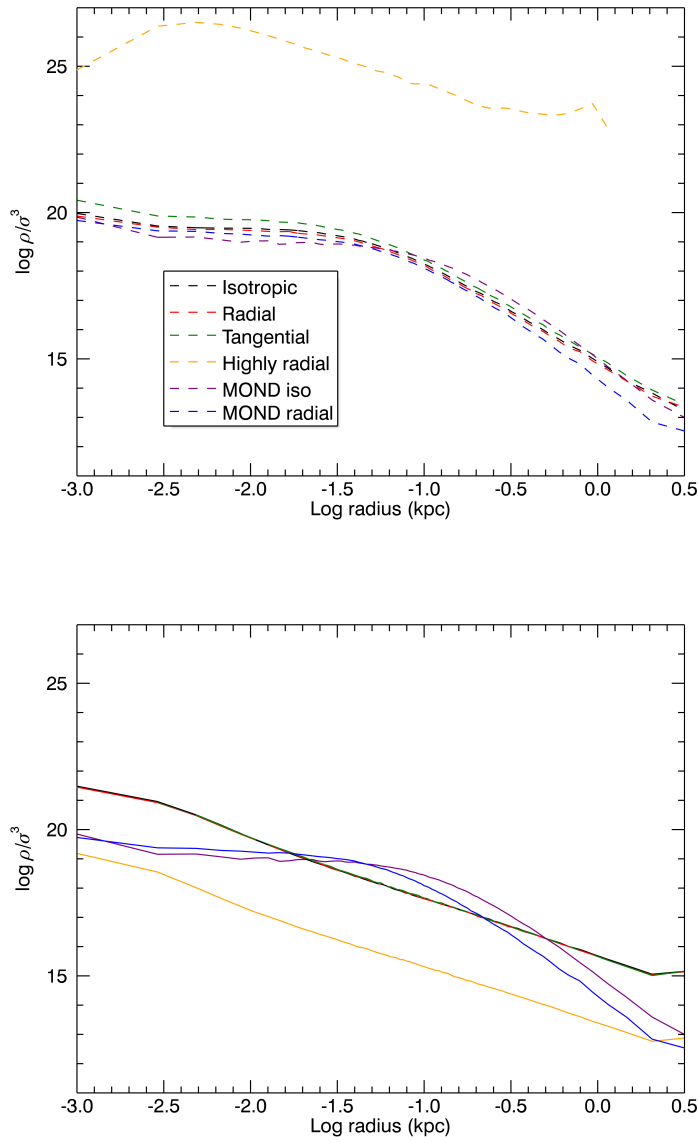


**Figure 5.18:** Evolution of phase-space density in the Newtonian isotropic (black), radial (red), tangential (green) and extremely radial (orange) models as well as the MONDian isotropic (purple) and radial (blue) models from their initial states (dashed/top) to their final states (solid/bottom).

### 5.6.3 $\beta$ - $\gamma$ relation

Seeing that we now have two convergent properties both of which involve velocity dispersions and density, it is not surprising that there are relations directly linking  $\beta$  and  $\gamma$  that also provide convergent results. Many studies have found evidence for a relationship between the two quantities (Huss et al., 1999; Barnes et al., 2005; Hansen & Moore, 2006; Hansen et al., 2006; Macmillan & Henriksen, 2006; Bellovary et al., 2008; Lapi & Cavaliere, 2011) and in particular Hansen & Moore (2006) went as far as positing a specific relationship of  $\beta(r) = -0.15 + 0.2\gamma$ . Although this result is not explicitly connected to ROI, instead being found in every relaxed structure tested, it still applies and several of those papers have used it for such.

This might sound rather familiar when put in the context of the work from chapter 2 on the GDSAI. The difference here is that these results discuss a much more specific relationship between these quantities than just the general inequality provided by the GDSAI. Whether or not the attractor and the GDSAI have any relation to each other is not known and will hopefully be the subject of future investigation.

## 5.7 The story so far

We have conclusively demonstrated that the attractor effect does occur and does so with no regard for the major initial characteristics of the system. The choice of anisotropy, size, theory of gravity, or numerical resolution makes no difference to the final evolved state of our models. In addition to these results, other work with different perturbations has been carried out in papers such as Sparre & Hansen (2012a) and Sparre & Hansen (2012b). They looked in detail at the appearance of the attractor in systems using radially aligned conical bins with more realistic merger scenarios as well as testing for the attractor in embedded sub-halos and systems undergoing cold collapse and violent relaxation.

This work was important particularly because it demonstrated that not all observed structure would actually land on the attractor in a realistic setting. The simulations that tended to lie on the attractor were the ones with more artificial perturbations applied, whereas the structures created by more realistic mergers had a lot more freedom. Overall it was felt that real merger events left a significant imprint on the system which prevented a simple relationship like the attractor being observed. However, even in these cases the

spherically averaged quantities of the systems still followed the attractor in the inner parts. This motivated a need to understand whether the attractor was created by a process based on the dynamics of the system or if it was an artefact of the perturbation scheme.

In particular this raised questions about the various effects that seem to be present alongside the evolution to the attractor. For example, all the systems tested so far have undergone a form of radial collapse which has left the system with a dense, low energy nucleus and a dispersed, high energy envelope. Primarily our interest lies in a possible connection between our perturbations and ROI due to the fact several universal profiles are known to exist for systems that experience ROI. The forms of these profiles are not greatly dissimilar to the attractor and it is important to prove one way or another if the two are related. For example, the anisotropy profile of our perturbed systems could be the common anisotropy profile of a system affected by ROI. Alternatively it could be a real, novel effect which would be of huge benefit to constraining collisionless halo properties through work such as Hansen & Sparre (2012).

Clearly, if the attractor is caused by radial infall then there is a chance to derive the form of the curve from first principles using the various relations from ROI as well as neatly constraining the requirements of evolving towards it. However, that requires a better understanding of what is necessary for a system to move to the attractor.

Unfortunately we have exhausted what we can learn from building systems and perturbations that cause convergence and now we need to identify the key components that the system requires to successfully converge. The next chapter will focus on this by starting with the most important question so far: is radial infall needed to reach the attractor?

# 6

## Necessary and Sufficient Conditions

*“If it isn’t broken, fix it until it is.”*

— US Army [attr.]

The problem with trying to understand why this attractor phenomenon occurs is that there are a lot of things going on in even the most stable of systems. A system that is just quietly sitting there in equilibrium is still obeying a complex interplay of potentials and particle energies that keep it balanced, stable, and rather dull. Trying to pick apart the different effects so as to point to one in particular and state that that one mechanism is critical for the phenomenon is a complicated affair.

It is because of this we need to change our approach. So far we have around ten or so systems and perturbations that can lead us to the phenomenon we call the attractor. This is obviously useful, but only up to a certain point. Now the question is what they all have in common. The answer is, unfortunately, quite a lot.

In order to make any progress we need to build a perturbation that breaks the attractor.

Some headway on that has already been made by looking at the emergence of the attractor under different, more realistic, merger and collapse scenarios (Sparre & Hansen, 2012a,b). While those papers did demonstrate deviations from the attractor along certain preferred axes which are defined by the vectors along which past mergers had taken place, they also still recovered the attractor in spherical averaged quantities.

Overall, those simulations are too complicated for us to easily do what we need to for this chapter. Instead, we will continue to use simple, spherically averaged simulations but we need to kick them in such a way that we change as little as possible from the methods of the previous chapter but what little we do change will prevent the attractor phenomenon from occurring. This will tell us exactly what are the ‘necessary’ conditions and ‘sufficient’ conditions.

This concept is a familiar one when trying to characterise the emergence of an effect and it stems from a fairly simple idea. If you have a complicated machine that performs a task, then sometimes the best way to understand it is to gradually remove pieces of the mechanism and see when it stops working. At the moment the machine grinds to a halt you can look at the piece in your hand and know to some degree of certainty that it is vital to the basic functions of the machine. If you were to place it back then the machine would continue to function as before. We can say that this piece is ‘necessary’ for the functioning of the machine.

Imagine now that you replace that necessary piece, but are still left holding a further piece which should rest on top of it. The machine still works even though you are holding it so clearly it is not necessary, but equally it must be removed in order to get at the necessary piece. A little logic tells us that if the piece you are holding is found in the machine then the necessary parts must also be in place underneath it. This means that the piece is ‘sufficient’. Proving that the sufficient piece is present is enough to demonstrate that the machine will work just fine. It is worth noting in particular that the most fundamentally important pieces will be both necessary *and* sufficient.

This applies equally well to the more abstract problem of the attractor. The purpose of this chapter will be to take the perturbations and the systems apart piece by piece until we find the critical components that we must have in order to converge on it. Understanding this is extremely important if the attractor is ever going to be looked for in real astrophys-

ical structures. Depending on the physics responsible for the attractor, it may either be largely irrelevant for cosmological structure or it may be of fundamental importance to all equilibrated structure. In particular we want to understand if the attractor appears due to physics which happens during successive mergers throughout the history of structure formation. If this is the case, which it turns out to be, then the attractor seems very important for the equilibrated part of all cosmological structures, in agreement with the results of large cosmological simulations (Ludlow et al., 2010).

Of particular note from the previous chapter was the suggestion that radial orbit instability (ROI) and/or radial infall (RI) were sufficient to demonstrate that a perturbation would lead to the attractor. We kick off this chapter by examining the possibility that it is a necessary condition.

We use the same kinds of simulations as we did for the previous chapter. Our models are still Plummer spheres of scale radius 0.05 kpc and contain  $5 \times 10^8 M_{\odot}$  in 750,000 particles. We do not include so many systems with exceptionally unusual initial anisotropies or those designed for use in MOND as that is not needed for this chapter. Accordingly, while we still use the code NMODY (Ciotti et al., 2006) for consistency, we run it only in its Newtonian mode.

## 6.1 Ruling out radial infall by adding energy

A key feature of the previous simulations was a significant amount of RI whereby systems would collapse into more radially anisotropic systems as they were kicked. The fact that all the simulations shared this common mechanism raised the question of whether or not RI is a necessary factor for the attractor. It turns out that, as predicted in the previous chapter, the radial infall is an inevitable consequence of the perturbations used. However, the link between the perturbation and RI is actually in how the system conserved energy.

The perturbation acts by scaling the components of velocity  $v_{x,y,z}$  but then the algorithm later proceeds to conserve energy in the form of  $v_{x,y,z}^2$ . This means that the conservation was asymmetrical when compared to the perturbation. The perturbation's symmetry is easy to prove as  $|(v + \delta v) - v| = |(v - \delta v) - v|$ , but when these terms are examined as energies the symmetry is lost because  $|(v + \delta v)^2 - v^2| > |(v - \delta v)^2 - v^2|$ .

This implies that particles that had their overall velocity increased were contributing

disproportionately more to the kinetic energy of the bin than was being removed by particles which had their velocities decreased by the same amount. This leads to an overall increase in energy. This was compounded because the energy conservation code worked on all particles equally and linearly, so the majority of particles in a bin ended up losing energy to compensate for the small fraction of particles which got large velocity increases. This sudden removal of energy from most of the bin is what results in the compaction of the system and the large number of particles on radial, infalling orbits.

Note that this is the general prescription offered by the bimodal perturbation of the previous chapter. While that perturbation may not have been designed to explain this symmetry problem, the overall effect is still the same. This means that the bimodal perturbation also stands in support of this interpretation of the mechanism and the critical point to address is still the importance of RI. If RI proves to be necessary for the attractor, and the algorithm was artificially inducing such an infall, then the attractor may just be an artefact of the perturbation scheme. ROI could become important due to the growing proportion of radial orbits in the system, eventually causing mild triaxiality (Antonov, 1973) and the development of the universal characteristics discussed in the previous chapter.

We therefore wished to define an algorithm that could rule-out, or confirm, RI as a contributing mechanism. To that end we designed the simple kick outlined above, based on the same algorithm of random numbers as in the previous chapter. The key difference is that the kick is now asymmetrical, only ever adding energy to a bin and never removing it, and no kind of energy conservation is enforced after the kick. The idea is that the system will expand as a result of the added energy and will not place more particles on infalling orbits which prevents the development of a collapsing state and will fail to trigger either RI or ROI.

### **6.1.1 Algorithm for avoiding infall**

The variation of the previous perturbation algorithm is only minor and the major changes are the limits of the scale factor and the lack of a conservation step. For completeness the new algorithm is:

- Set up a series of concentric radial bins defined to contain 5,000 particles each.
- For each particle in each bin we examine each of the three orthogonal velocity vec-

tors and multiply each by a random number  $f$  drawn from a uniform distribution of  $1.0 < f < 2.0$ . The fact that the distribution is *not* centred on unity is what lends the scheme its desired asymmetry, as any given velocity component will be at least as big as it was prior to this scaling.

- Derive a dynamical timescale for the system

$$t_{dyn} = \sqrt{\frac{1}{G\rho}} \text{ where } \rho = \frac{0.95 \times M_{tot}}{\frac{4}{3}\pi r_{95\%}^3} \quad (6.1)$$

where we again use the 95<sup>th</sup> mass percentile as a representative distance for the system. For our initial systems this is equivalent to approximately 3 scale radii.

- The system is then left to evolve in an N-body simulator for 3 dynamical timescales.
- Repeat the cycle as needed.

This kick can only be applied a finite number of times before a significant number of particles become unbound from the system. After a large amount of particles become unbound they will no longer interact with each other and the system will cease to have a meaningful dynamical timescale. We find that for this particular kick this effect starts to dominate around the fifth kick cycle by which point the outermost 50 bins, *i.e.* 250,000 particles or a third of the entire system, have become entirely unbound. At this point the simulation must be manually halted as the divergent behaviour of the dynamical timescale becomes insurmountable as well as increasingly meaningless.

If, after performing this algorithm, the system did not evolve towards the attractor or evolved in a different manner now that infall was being prevented then that would suggest that RI was a necessary factor. Note that we don't require the system to come to rest on top of the attractor as 5 kick-flow cycles is not enough to reach the attractor. We will instead interpret the system as an intermediate stage of convergence and analyse it in that context.

Fig. 6.1 shows a plot of the attractor for this kick. As in the previous chapter the open shapes are bins of 5,000 particles each and the red line is data from Hansen et al. (2010) marking the position of the attractor in the parameter space. The system shows, despite the unrealistic kick, significant evolution towards the same phase-space as the attractor. It

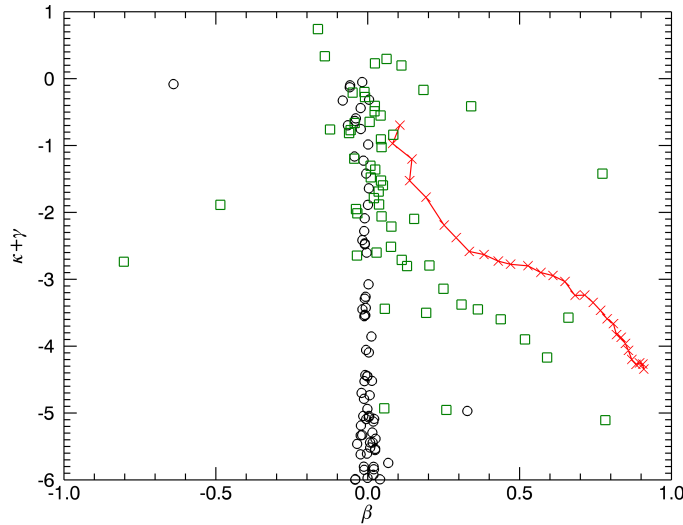


**Figure 6.1:** Plot showing the system’s progress towards the attractor using the energy-adding kick. As in the previous chapter each point represents a mass bin of 5,000 particles and the red line is the position of the attractor. Black circles show bins from the initial conditions whilst green squares are likewise the state *after 5 kicks*.

is not sitting directly on the attractor but this is to be expected. Prior to this the system was showing standard, regular evolution towards the attractor which slowed in proportion to the amount of unbound material. We conclude from this that neither RI nor ROI are driving the convergence as repeated expansions still lead to the attractor.

## 6.2 The requirements for convergence

Having demonstrated that ROI is not the driving force behind the attractor we now consider two possible origins for it; energy exchange and phase mixing in a dynamic potential. We will show that those two effects are both necessary and sufficient conditions for the emergence of the attractor. Since these effects are always present during mergers we can demonstrate the potential importance of the attractor for cosmological collisionless structures (Ludlow et al., 2010).

### 6.2.1 Energy exchange — the anisotropy kick

Energy exchange refers to energy being passed between particles by gravitational interaction. Any dynamical system must exchange energy to evolve, but our perturbations are

not dynamical events. The perturbations act globally and instantaneously leaving dynamical effects such as energy exchange to guide structural reconfigurations during the flow phase. Thus, in order to examine the importance of energy exchange during the flow phase we must design a perturbation that disturbs the system without causing subsequent energy exchange between particles.

The kick that is used here is such a perturbation. The kick acts by rotating velocity vectors which causes a shift in the particle's path through phase-space. Such an algorithm fails to conserve angular momentum, however we cannot avoid the non-conservation of some characteristics if we are to have a perturbation. As discussed previously, there is no algorithm that can meaningfully perturb a system while completely conserving energy and angular momentum at the global level. Fortunately, we are attempting to model mergers and situations where external events perturb the structure of a system, so an increase in angular momentum or energy is not unrealistic.

Anyway, this new perturbation leaves the particles on new, stable orbits since their kinetic and potential energies are unchanged. Thus, the radial regions indicated by the apocentres of the particles barely change while the pericentres move because of the change of angular momentum.

We term this perturbation the 'anisotropy kick'. It alters the system's  $\beta$  profile by rotating each particle's velocity vector by a calculated amount. This process conserves energy but obviously fails to conserve angular momentum and can be seen in representation in Fig. 6.2. The foundation of the method remains the same as from previous examples with the application being carried out in alternating patterns of kick and flow. We will now spend a moment to go through the construction of this algorithm.

This construction of the kick requires a few terms defined in advance. A bin in our system has a population of  $n$  particles that give the bin an anisotropy of  $\beta$  based on their kinetic energy,  $T$ , in the radial,  $T_r$ , and tangential,  $T_t$ , directions.  $T_t$  is made up of  $T_\theta$  and  $T_\phi$  and we specifically define  $T_t = \frac{1}{2}(T_\theta + T_\phi)$ . A quantity associated with an individual particle is denoted with a subscript  $i$ . We are talking about a perturbation, so we speak in terms of an *initial* state,  $\beta_1$ , and a *final* state,  $\beta_2$ . As such, we begin from the definition of anisotropy:

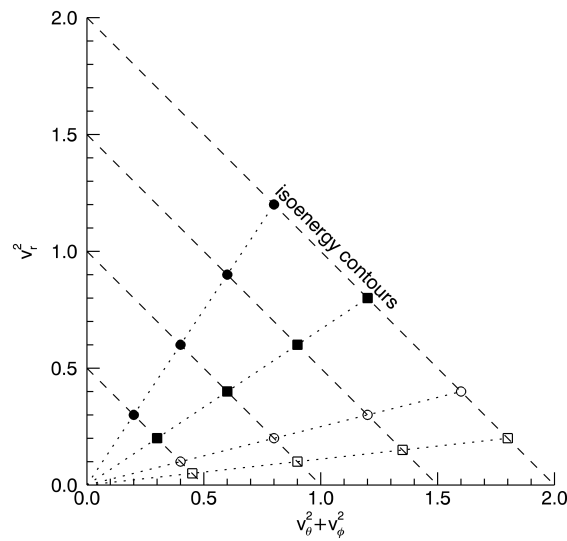


**Figure 6.2:** A visual representation of how the perturbation changes anisotropy. Particles are moved along isoenergy contours (dashed lines) from the open symbols to the closed symbols. This plot shows a kick of  $\alpha = 6$  (see Eq. 6.14) applied to two groups of particles, one with most of their energy in the tangential velocity components (squares) and the other with a more even distribution (circles). The dotted lines are visual guides connecting particles with equal anisotropies but different energies. The distance moved along the isoenergy contours depends on the particle's initial position along them.

$$\beta_1 = 1 - \frac{\sum_{i=1}^n T_{t1i}}{\sum_{i=1}^n T_{r1i}} \quad (6.2)$$

Our perturbation acts to move the anisotropy from  $\beta_1$  to  $\beta_2$ . We express this change as  $x\beta_1 = \beta_2$  so we can then say:

$$x\beta_1 = 1 - \frac{\sum_{i=1}^n T_{t2i}}{\sum_{i=1}^n T_{r2i}} = 1 - \frac{a(x) \sum_{i=1}^n T_{t1i}}{b(x) \sum_{i=1}^n T_{r1i}} \quad (6.3)$$

where  $a$  and  $b$  are just another, more helpful way of representing the impact of  $x$  on the particle energies. Speaking of the particle energies, we require global energy conservation, so we specify that:

$$2a(x) \sum_{i=1}^n T_{t1i} + b(x) \sum_{i=1}^n T_{r1i} = 2 \sum_{i=1}^n T_{t1i} + \sum_{i=1}^n T_{r1i} = \mathcal{E} \quad (6.4)$$

where  $\mathcal{E}$  is the system's overall kinetic energy. We can thus create definitions of  $a$  and  $b$ :

$$a(x) = \frac{\mathcal{E} - b(x) \sum_{i=1}^n T_{r1i}}{2 \sum_{i=1}^n T_{t1i}}; \quad b(x) = \frac{\mathcal{E} - 2a(x) \sum_{i=1}^n T_{t1i}}{\sum_{i=1}^n T_{r1i}} \quad (6.5)$$

We can then apply these expression to each other to obtain solutions that are still explicitly linked by energy conservation but can now be expressed separably:

$$a(x) = \frac{\mathcal{E}}{\sum_{i=1}^n T_{t1i} \left(2 + \frac{1}{1-x\beta_1}\right)}; \quad b(x) = \frac{\mathcal{E}}{\sum_{i=1}^n T_{r1i} (3 - 2x\beta_1)} \quad (6.6)$$

This tells us how the bin as a whole must act, but does not tell us how to achieve this by manipulating individual particles. To find that we must make  $a$  and  $b$  more applicable to each particle.

When we scale the bin's tangential energy  $\sum_{i=1}^n T_{t1i}$  by  $a$  what we are actually doing is multiplying each particle's energy by some number, *quite possibly a different number for*

each of them, and we need a way to determine what that number should be. To that end, we create two more variables,  $d_i$  and  $e_i$ , to express the impact of  $a$  and  $b$  on individual particles.

For convenience we do not write out the dependence of  $d_i$  and  $e_i$  on  $a$  vis.  $d(a)_i$ . This reduces clutter and the final result of the process will not need to refer to  $a$ ,  $b$ , or any of the other scale factors introduced in this process anyway. We can now use these variables to extend our previous results:

$$\sum_{i=1}^n T_{t2i} = a(x) \sum_{i=1}^n T_{t1i} = \sum_{i=1}^n d_i T_{t1i} = \frac{\mathcal{E}}{1 + \frac{1}{1-x\beta_1}} \quad (6.7)$$

$$\sum_{i=1}^n T_{r2i} = b(x) \sum_{i=1}^n T_{r1i} = \sum_{i=1}^n e_i T_{r1i} = \frac{\mathcal{E}}{2 - x\beta_1} \quad (6.8)$$

As well as global energy conservation, we now specify the requirement for energy conservation at the particle level as well. We call the energy of a particle  $E$  and then define it:

$$2d_i T_{t1i} + e_i T_{r1i} = 2T_{t2i} + T_{r2i} = E_i \quad (6.9)$$

At this point it is convenient to start constructing the problem in terms of a single variable that we must solve for,  $\alpha$ :

$$\frac{T_{t2i}}{T_{r2i}} = \frac{d_i T_{t1i}}{e_i T_{r1i}} = \alpha_i \frac{T_{t1i}}{T_{r1i}} \quad (6.10)$$

This allows energy conservation to be rephrased as:

$$\left( 2\alpha_i \frac{T_{t1i}}{T_{r1i}} + 1 \right) e_i T_{r1i} = E_i \quad (6.11)$$

By manipulating energy conservation in this way, we arrive at the definitions:

$$d_i T_{t1i} = \frac{E_i}{2\alpha_i \frac{T_{t1i}}{T_{r1i}} + 1} \alpha_i \frac{T_{t1i}}{T_{r1i}} \quad (6.12)$$

and:

$$e_i T_{r1i} = \frac{E_i}{2\alpha_i \frac{T_{t1i}}{T_{r1i}} + 1} \quad (6.13)$$

By taking these results back to Eqs. 6.7 and 6.8 and then combining them with the starting point of Eq. 6.3, we arrive at our final result:

$$\frac{\sum_{i=1}^n \frac{E_i}{2\alpha_i \frac{T_{t1i}}{T_{r1i}} + 1} \alpha_i \frac{T_{t1i}}{T_{r1i}}}{\sum_{i=1}^n \frac{E_i}{2\alpha_i \frac{T_{t1i}}{T_{r1i}} + 1}} = 1 - x\beta_1 \quad (6.14)$$

There are many solution sets for  $\alpha$  that will yield the result we want and we have no way of choosing between them without stating another condition. The condition we set is that  $\alpha$  has one fixed value for each mass bin, and then we solve the equation for  $\alpha$  by iterating to a self-consistent value.

### 6.2.2 Energy exchange — the anisotropy contours

The resulting system will be slightly radially Jeans unstable, *i.e.* not satisfying the static spherical Jeans equation. After the kick the system will still need to re-establish equilibrium but does so without a prescribed way that the new equilibrium is reached.

We first take an initial system with a radially anisotropic velocity ellipsoid and perturb it towards isotropy. Fig. 6.3 examines the change in the velocity anisotropy of the system as it equilibrates after the kick. We define the ‘change in velocity anisotropy’ simply as  $\frac{\Delta\beta}{\Delta t}$  where  $\Delta t$  is time between outputs of the state of the system *i.e.*  $0.01 T_{dyn}$ . The kick is visible as the large, dark-blue section at the beginning of the time series. After the kick the system relaxes over the course of about a dynamical time. This relaxation is shown by the yellow-green tint across the rest of the plot, showing a general trend for the system to drift back towards a more radial velocity anisotropy. See Fig. 6.4 for an alternative representation of some of the information displayed in Fig. 6.3.

There are two especially prominent features in Fig. 6.3 that require comment as they are not due to physics that interests us. The first is the kick itself, clearly visible as a large, dark area along the left side, and the other is the ‘sawtooth’ pattern of spikes of

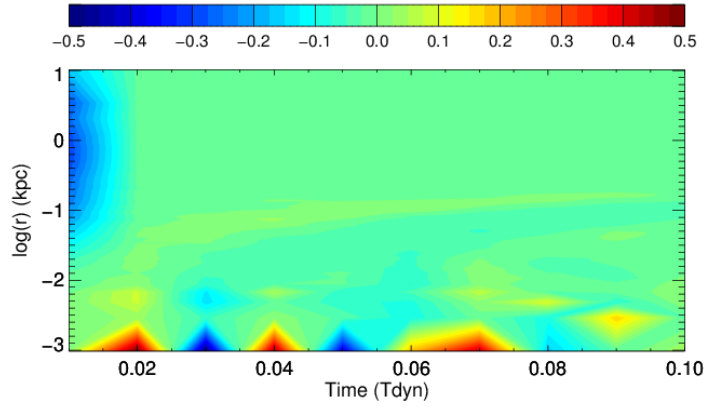


**Figure 6.3:** Contours showing the changes in velocity anisotropy of an initially radially anisotropic system as it recovers from a moderately isotropising kick. We define the change in velocity anisotropy simply as  $\frac{\Delta\beta}{\Delta t}$  where  $\Delta t$  is time between outputs of the state of the system *i.e.*  $0.01 T_{dyn}$ . The change in anisotropy between outputs at a certain radius is represented by the colour of the contours where blue colours indicate an ongoing change towards tangential anisotropy and red colours indicate likewise for radial anisotropy. Green represents no evolution of anisotropy between outputs.

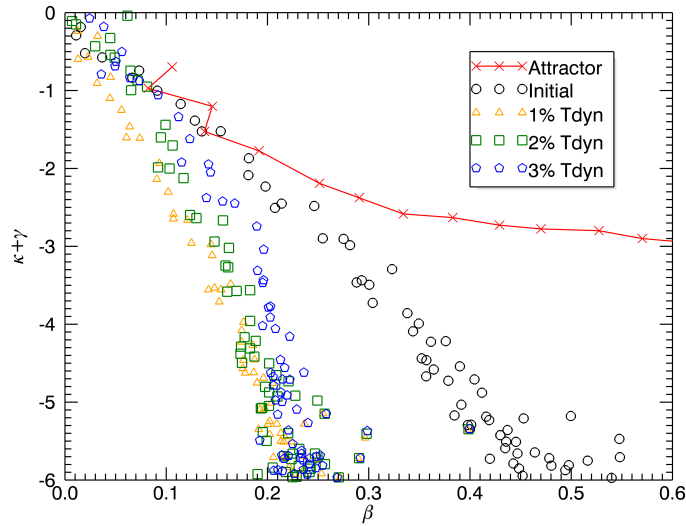


**Figure 6.4:** A more familiar presentation of some of the datasets represented in Fig. 6.3 using the parameter space of the more familiar attractor plots. Note the gentle drift of the data towards radial anisotropy during the first 3% of a dynamical time after the first kick that is shown in Fig. 6.3 by the yellow-green hue of the majority of the contours.

alternating anisotropy change that run along the bottom of the graph. Both of these features overshadow the actual point of interest, the general trend of the plot, and all future plots will be cropped and re-scaled to remove them. We will now take a moment to justify the removal of these features.

Firstly, removing the kick is regrettable but it is of such greater magnitude than anything else in the plot that retaining it diminishes the contrast of the important contours. Additionally the only useful information that it contained was the choice of the applied kick which is known and always indicated.

Secondly, the ‘sawtooth’ pattern that appears at very small radii is caused by an unfortunate combination of two factors. Firstly, the logarithmic scale artificially overemphasises the relative importance of the inner bins by giving them a large area on the plot. This is then compounded by the second issue which is the tendency for the very innermost bins to have an extremely noisy velocity anisotropy as a result of the data analysis. Clipping those few bins cleans the data considerably, removes only a small amount of particles, and does not destroy any useful information.

With this in place we can clearly see the overall impact of the kick. The amount of settling is a negative feedback effect that is a fraction of the size of the perturbation. For example, if the system is initially strongly radial and the kick is strong enough to make the system exactly isotropic then the settling will act to reverse the kick by drifting towards radial states. The drifting is stronger and more pronounced in proportion to the magnitude of the initial kick but will never be enough to undo the kick. This system was run and the results, which support this conclusion, are shown in Fig. 6.5.

The next step is to demonstrate that this negative feedback is not related to the attractor. In Fig. 6.6 we take an initially tangentially anisotropic system and perturb it towards isotropy. What we see is the reverse of Fig. 6.3 as the settling is more tangential and thus there is more light blue.

This demonstrates our hypothesis that when a system is perturbed with the anisotropic kick the subsequent period of relaxation will reverse a small fraction of the isotropy change. This means that while this perturbation does destabilise the system and allow it to find new equilibria, it does not lead towards the attractor.

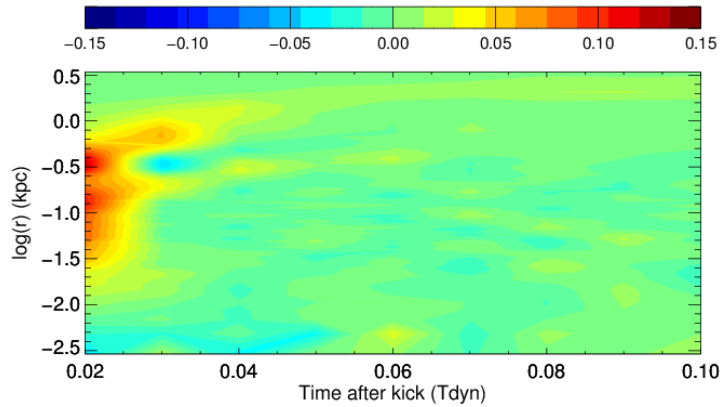


**Figure 6.5:** Contours showing the changes in velocity anisotropy of an initially radially anisotropic system as it recovers from a kick that set it to be exactly isotropic. Notice that the system recovers by settling back towards radial anisotropy like the system in Fig. 6.3, only much more strongly. Also note that, in line with the discussion in the body text and in contrast to Fig. 6.3, the oversaturated noise and kick features have been removed and the colour scale has changed. Thus, *the red spot along the left is not the kick but the resettling of the system after the kick has occurred.*

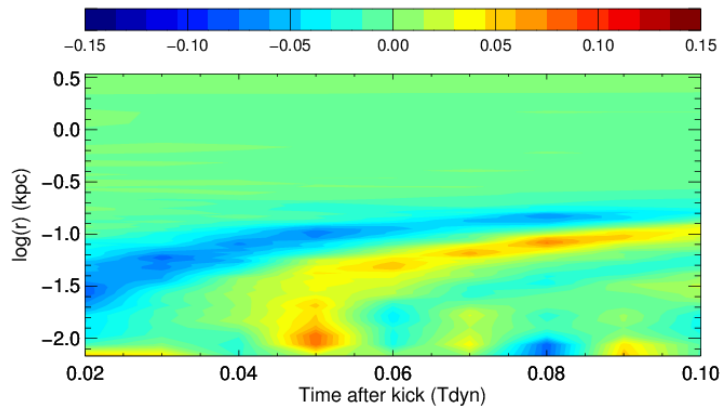


**Figure 6.6:** Contours showing the changes in velocity anisotropy of an initially tangentially anisotropic system as it recovers from an isotropic kick. The green-blue hue of most of the plot, demonstrating motion towards tangential anisotropy, shows that settling is not directed towards the attractor. The two large stripes across the plot are the equivalent of the red spot in Fig. 6.5 and are the settling of the system against the kick. Here the settling is towards a more tangential anisotropy and occurs in a ripple of anisotropy change through the system from the inner regions to the outer. This effect is still minor compared to the kick and the settling overall does still obey the established rule.

In our final test of this we took an initial system with mild radial anisotropy and repeatedly perturbed it so that it passed over the phase-space associated with the attractor. The reasoning is that if the system is still being affected by the attractor then we would expect it to behave differently as it passes over. We performed several iterations of our algorithm and primarily looked for any changes in the magnitude or direction of the evolution during the flow phase.

Analysis of these runs showed no evidence that any perturbation cycles were being drawn to the attractor. The anisotropy evolution contours remain comparatively featureless throughout and show no behaviour different from any of the other simulations.

In summary, it appears that this method of perturbing the system causes the system to undergo mild slight evolution in response to the kick, but this seems restricted to a weak, negative feedback effect that bears no relation or correlation to the attractor. From the absence of the attractor in a perturbation that minimises the impact of energy exchange we conclude that energy exchange is necessary for the phenomenon.

### **6.2.3 Phase mixing in a fixed potential — the massless kick**

By phase mixing we mean how particles disperse through the phase space of the system. This generally reduces the coarse grained phase-space density as the particles fill their orbital tori evenly. The process is kinematic and the dispersion of particles along their orbits even occurs in static potentials (Binney & Tremaine, 2008) which corresponds to the processes that occur during the ‘flow’ periods of our perturbation schemes. We have already discussed how repeated kicks without subsequent periods of settling flow will not lead to the attractor as the evolution occurs over a period of time after the kick. Here we will further emphasise the importance of the dynamics of the flow by considering relaxation in a fixed potential.

This perturbation involves making the particles massless. We take the same Plummer spheres as in our other simulations but then freeze the system’s numerical, not analytical, potential and transform the particles into a population of massless tracers. This means the background potential is no longer coupled to the particle distribution and because the simulation is collisionless, the particles have no way of interacting with each other. After the kick has occurred the particles will not be able to directly influence each others

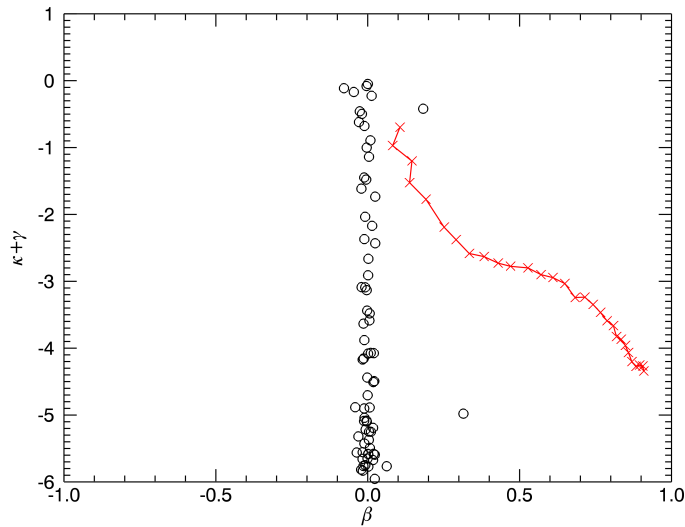


**Figure 6.7:** A plot showing an initially anisotropic system after an application of the ‘massless kick’. Comparison between the system’s initial state and its final state is made difficult as the system has not evolved *at all* as a result of the kick. The black circles are bins of the system after one kick and have been completely unaffected by the kick. The red line is the attractor.

positions in phase space and the only evolution in the system will be due to phase-mixing.

If the attractor is driven only by the kick then removing the dynamical potential should have minimal effect on the system’s convergence to the attractor as simply the act of kicking would cause convergence. Here we test whether a dynamically coupled potential is necessary for the attractor using this ‘massless kick’ approach. The actual perturbation that we perform is the same scaling kick as was used in the majority of systems studied in the previous chapter.

The results are shown in Fig. 6.7 where we see that the system has failed to evolve at all. This shows that the attractor does not arise purely from the kick and that a subsequent period of mixing in a dynamic potential is necessary. This is the case for almost all physically realistic instances of structure formation.

We have identified the two primary mechanisms that are necessary and, between them, sufficient to allow convergence towards the attractor.

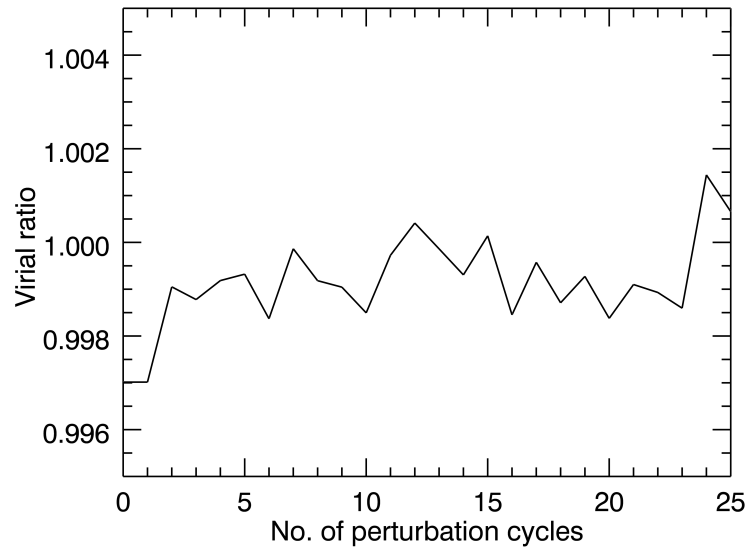


**Figure 6.8:** Virial ratio at the end of every flow phase for the isotropic Newtonian simulations.

### 6.3 Impact of the attractor

Having established the requirements for the attractor and looked in detail at what the attractor ignores, we will now round off this chapter by looking at what happens to a system on its journey towards the attractor.

To begin with it appears that we do not drive the system significantly out of energy equilibrium with our standard perturbations which is what we expect from the symmetries of the perturbation. We can easily examine the virial ratio of the system – a simple ratio of global kinetic and potential energies that should balance if the system is in equilibrium – and we find that, to within a reasonable limit, the system always maintains a balanced virial ratio. We also know that our perturbation conserves energy and does not change the potential so the start of the flow is virialised if the end of the preceding flow phase was virialised. We can show this by calculating the virial ratio at the end of every flow phase for our initially isotropic Newtonian system which we plot in Fig. 6.8.

Although we don't change the total energies of the system, we do change how that energy is distributed between velocity components. However, our perturbation does not explicitly favour any anisotropy as it treats each independent velocity component equally.

An initially isotropic system will still be isotropic after an application of our standard kick. We can prove this rigorously by thinking about how one component of velocity is influenced by our standard kick. For example, the radial velocity is:

$$v_r = \frac{|x|v_x f_1 + |y|v_y f_2 + |z|v_z f_3}{r} \quad (6.15)$$

where  $x$ ,  $y$ , and  $z$  are the cartesian positions and  $v_x$ ,  $v_y$ , and  $v_z$  are cartesian velocities. The radial vector is given by  $r$  and  $f$  is the scaling kick delivered to a particular cartesian velocity component. We know that we are conserving kinetic energy in the system which is the square of the velocities so we can investigate what happens to :

$$\begin{aligned} \sum^N v_r^2 &= \sum^N \left( \frac{|x|v_x f_1 + |y|v_y f_2 + |z|v_z f_2}{r} \right)^2 \\ &= \sum^N x^2 v_x^2 \frac{f_1^2}{r^2} + y^2 v_y^2 \frac{f_2^2}{r^2} + z^2 v_z^2 \frac{f_3^2}{r^2} + \left[ 2|xy|v_x \cdot v_y \frac{f_1 f_2}{r^2} + \dots \right] \end{aligned} \quad (6.16)$$

Since the axes are orthogonal the cross terms all vanish which leaves us with:

$$\sum^N v_r^2 = \sum^N x^2 v_x^2 \frac{f_1^2}{r^2} + y^2 v_y^2 \frac{f_2^2}{r^2} + z^2 v_z^2 \frac{f_3^2}{r^2} \quad (6.17)$$

In a large enough sample of particles the random scale factors that we apply will generally become represented by the expectation value of the distribution of  $f$ . Since  $f$  is drawn from a uniform distribution centred on unity we can state that the expectation value is also unity. This means that, overall, our random perturbations will sum to unity and we will not alter  $\sum v_r^2$ .

The only distribution that we do directly alter is the distribution of the particles in energy-momentum space where the perturbation acts to spread out the distribution with successive shocks. This can be imagined as, in each bin, the particles with the highest and lowest velocities might get scaled to even higher and lower velocities respectively which has the effect of broadening the distribution in that bin.

Fig. 6.9 shows a 2-D histogram of our system in the space of kinetic energy,  $E_{kin}$ , against angular momentum,  $J$ . As the system is perturbed we find, as we discussed, that

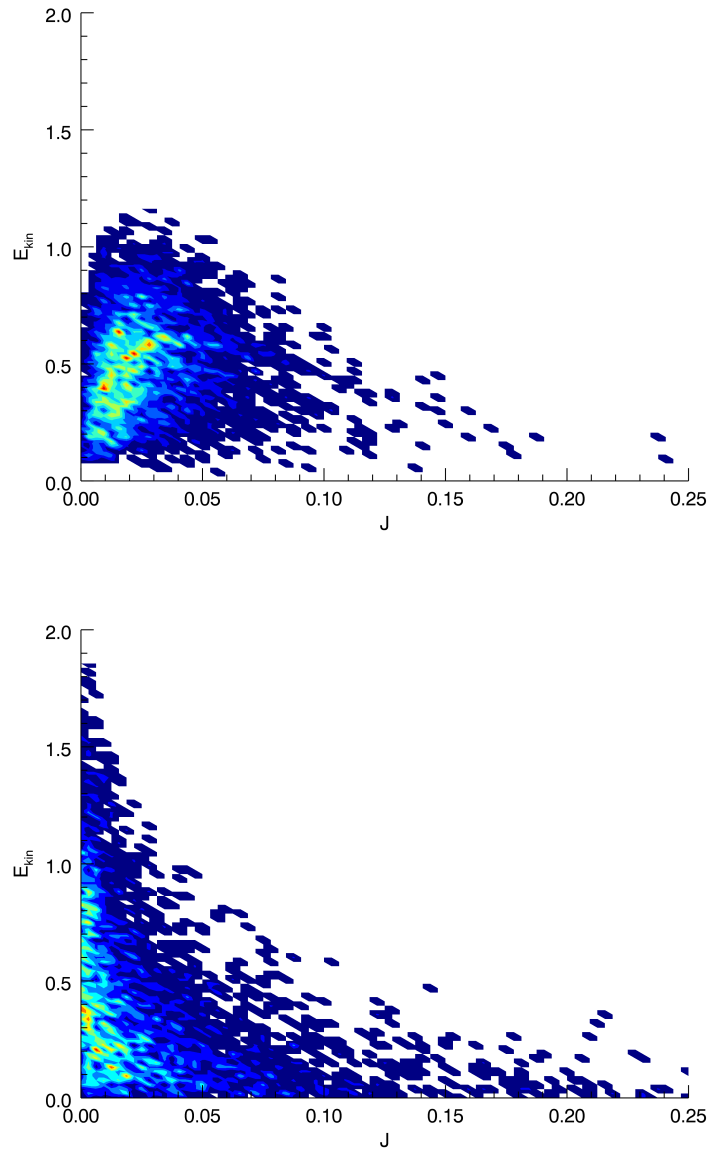


**Figure 6.9:** Evolution of  $E_{kin}$ - $J$  number density contours for the isotropic Newtonian system from the initial conditions (top) to the final state after 30 perturbations (bottom). The initial system's isotropy means that the distribution is more focused around mid-range values. After the perturbations many more particles are found in low- $J$  states and there is a population at  $E_{kin} \approx 0$  which was not found before. The clear edge to the distribution is given by the binding potential and the angular momentum of circular orbits. The hexagonal effect in low density areas is an artifact of the binning process used for the contours in areas of low population.

the kinetic energy distribution spreads out while the distribution of  $J$  becomes slightly compacted towards 0. The latter effect is because of the increase in radial anisotropy implying a decrease in the amount of energy in tangential velocity modes which, in turn, lowers the average angular momentum of the system.

Note the clearly defined excluded area in the upper-right portion of the histogram. The energy is limited by the binding potential as we already specified that the entire system is bound. The allowed angular momenta are bounded by the characteristic angular momentum of a perfectly circular orbit at a particular radius. Since the maximum angular momentum is a function of maximum kinetic energy and the maximum kinetic energy is a smooth function of radius through the potential there is a smooth relationship between the two axes. This forms a smooth limit on the allowed regions of the histogram.

### 6.3.1 Density profiles

As we have discussed previously, one of the characteristic features of our perturbations is the creation of two distinct populations of particles. We find a large density of particles at small energies and radii which have fallen into the centre of the system as well a population of particles that have been pushed to the edges of the system on high energy, highly radial orbits. This ‘nucleus’ population is what fills the previously empty regions around  $E_{kin} \approx 0$  in Fig. 6.9 and increases the density at low angular momentum while the ‘envelope’ particles populate the low angular momentum regions at high kinetic energy. This interpretation can be easily supported by looking directly at the cumulative mass profile of the same system after perturbation which we present in Fig. 6.10.

On the topic of the mass profiles, our interest in the attractor was originally motivated in part by its relation to universal profiles and a possible relationship to the NFW profile. We now examine what happens to the density profiles of our perturbed systems although we have admittedly not seen anything so far to suggest that the attractor is also an attractor in density. We compare the final density profiles of a variety of our models with some examples of standard density profiles. Note that the different form of the MOND Poisson equation causes MOND Plummer spheres to have the same shape but a lower central density so that more material can be present at large radii.

Fig. 6.11 shows that the models have changed noticeably from their initial configura-

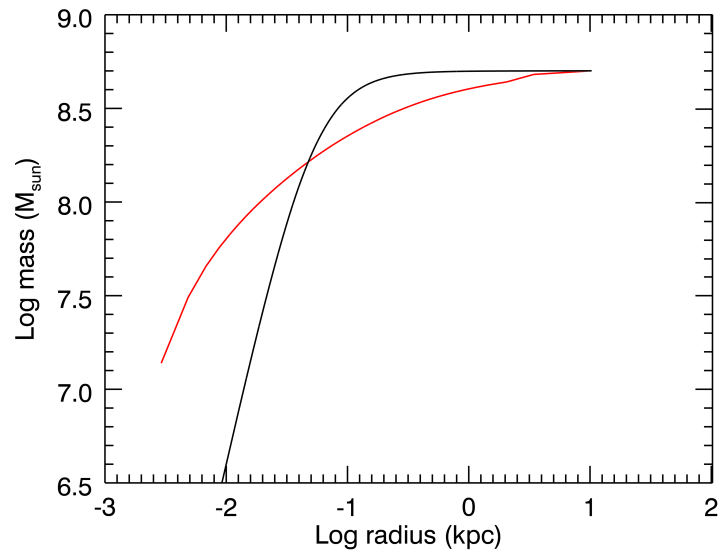


**Figure 6.10:** The development of the nucleus/envelope arrangement caused by the standard perturbation after 30 cycles. The initial cumulative profile (black) has considerably less mass enclosed at small radii than the final profile (red) and has a shallower gradient at larger radii. This effect is related to the preferential selection of radial orbits explained by the bimodal kick.

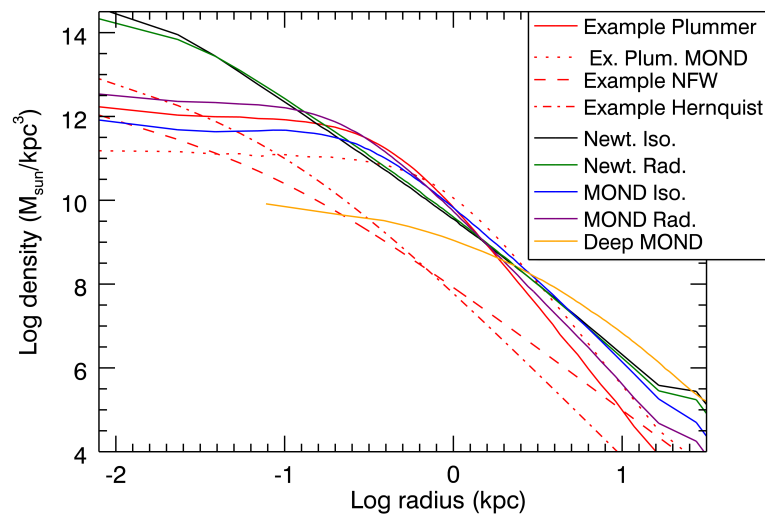


**Figure 6.11:** Final density profiles from a selection of simulations contrasted with an arbitrary NFW profile, arbitrary Hernquist profile and the initial conditions of the Newtonian and weak MOND Plummer profiles.

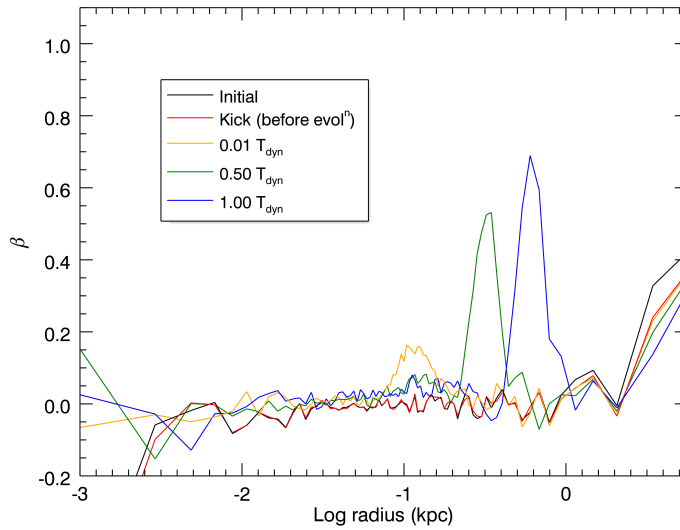


**Figure 6.12:** The anisotropy profile of a standard isotropic system during the initial conditions, after the kick has been applied but before the system has been allowed to relax, and then subsequent profiles as the system relaxes.

tions. We see that the ‘nucleus/envelope’ arrangement is visible here and has the effect of producing an almost Hernquist-like profile. We can also see our other effects such as the steeper central profiles of our Newtonian models compared to the MOND models and the increased core density overall as a result of the radial infall. Overall, however, there does not appear to be any particularly strong agreement or convergence present between our density profiles. While we note several effects that are connected to our standard perturbation, there is no evidence that the attractor extends to a preferred density profile.

### 6.3.2 Anisotropy profiles

Finally we examine the changes of the anisotropy profile during a single flow phase and discuss several features that appear. The most interesting effect is how the changes in anisotropy propagate through the system. They begin in the inner regions and travel outwards as a wave of radial anisotropy as shown in Fig. 6.12. This is fairly easy to understand as an effect of the creation of the envelope population. As the particles are given additional kinetic energy they travel outwards toward the edge of the system which means that there is now a population of particles with a lot of radially-orientated kinetic energy moving to progressively larger radii.

We can clearly see that the perturbation scheme itself does not instantaneously perturb the anisotropy profile to any significant degree. However, we also see that within a very small amount of time we have a pronounced peak over a range of radii which then proceeds to migrate towards the outer regions of the system. The peak originates from the highest density area of the system and is caused by the creation of the envelope population.

It is apparent that the wave of anisotropy is still very well defined, even after  $1 T_{dyn}$ . This seems strange but is because Fig. 6.12 plots the anisotropy as a function of radius, not mass. In actual fact the wave contains a small number of particles and there are very few particles between the wave and the edge of the system. This also means that if the system is left to evolve further then the anisotropy profile will not change significantly as it has already reached the edge of the system. This is evidenced back in Fig. 5.13 where we demonstrated that allowing the system to flow for a further  $2 T_{dyn}$  had no impact on the system's evolution towards the attractor.

So, we have shown that the perturbation does create a population of strongly radial particles but only by influencing the total kinetic energy rather than by directly affecting a net change in anisotropy like our kick from §6.2.1. If the kick was changing the anisotropy directly then we would see a change in the profile immediately after the kick rather than needing  $0.01 T_{dyn}$  of flow time.

In general, the preference for radial velocities – either in the infalling population or the envelope – is due to the statistics of putting a particle on a circular orbit. Imagine a particle on a circular orbit. If we perturb this particle using our scheme then the particle will either gain or lose energy except in the exceptionally unlikely scenario where all velocity components are scaled by unity. Since the particle was on a circular orbit then any perturbation will make the orbit elliptical and increase the fraction of energy in radial velocity.

If we want to return our hypothetical particle onto a circular orbit then we would need to, by random chance alone, not only give the particle the correct amount of total energy so that a circular orbit is possible but also make sure that the energy is placed in the correct velocity components so that the particle has much less radial motion. This is overwhelmingly unlikely compared to the chance of placing it on another elliptical orbit

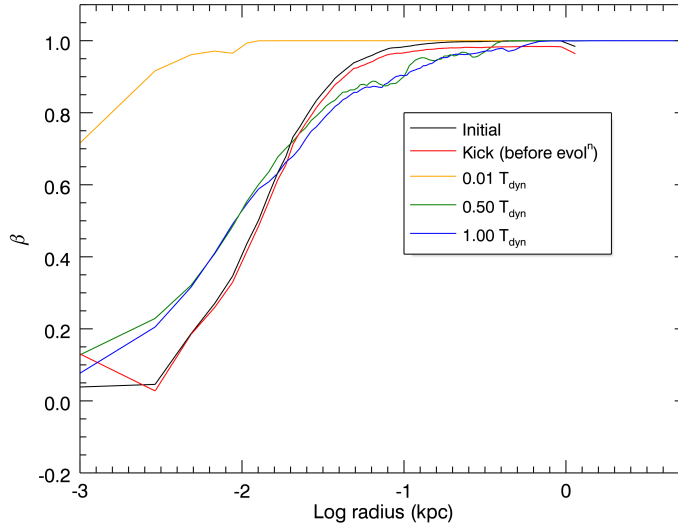


**Figure 6.13:** The anisotropy profile of the very radial IC during the initial conditions, after the kick has been applied but before the system has been allowed to relax, and then subsequent profiles as the system relaxes.

which is why the anisotropy tends to become more radial over time.

We do see different behaviour in systems that are initially more radially anisotropic than the attractor. Fig. 6.13 shows that the perturbation itself still does not change anything but the ‘wave’ of anisotropy visible in Fig. 6.12 is absent. This is because the mechanism here has more in common with radial infall and thus the most significant effect seen in the profile is the inward collapse of the highly radially anisotropic outer edges. The outward ‘wave’ of high energy particles produced by the perturbation is still present, but the lack of an isotropic background for the profile prevents it from standing out against the collapse of the rest of the system. However, the presence of this wave can still be inferred from the increased size of the system after flow.

The outer parts of the initial system quickly collapse radially inwards as the kick, as we know, robs most of the system of energy which explains the extremely radial profile of the system at  $0.01 T_{dyn}$ . As they move inwards they dramatically increase the radial anisotropy of the region they pass through until they eventually settle into more circular orbits at smaller radii after roughly  $1 T_{dyn}$ .

The more isotropic regions in our system behave the same as the system from Fig. 6.12

and thus we have a small increase radial anisotropy in these regions. Overall, we find the nucleus becomes more radial at the expense of the envelope thanks to the inward migration of much of the outer regions. We still see a very radial population at the extreme edge of the system as the highly energetic ‘wave’ population is still present albeit overshadowed by the collapse of the existing radial population.

It is possible that the particular position of the attractor in phase-space represents an equilibrium point between two competing effects. In an isotropic system the kick will tend to push energy into a small population and make it radial. In an extremely radial system the kick will generally preserve the anisotropy of some of the radial material while siphoning energy away from the majority of it. This induces a change towards isotropy compared to the initial state of the system. There is perhaps reason to suspect that the form of the attractor is defined by the a system which represents a mid-point where neither of those effects can dominate.

## 6.4 The path to convergence

We have covered all of the major phenomena associated with the attractor and our examination of it is almost at an end. To close out we will examine how a system will move through the parameter space to arrive at the attractor. Firstly we investigate whether the large scale behaviour of our simulations is mirrored by the behaviour of a single mass bin. For this section we only use the results from our Newtonian simulations as the MOND simulations will potentially introduce some amount of systematic error when comparing masses and radii.

In Fig. 6.14 we overlay the successive positions of the 20<sup>th</sup> bin in each of our Newtonian simulations and note that they all follow the same path towards the attractor. The 20<sup>th</sup> bin was not chosen for any special reason and this plot could have been produced with any of the bins in our data. However, the 20<sup>th</sup> bin was positioned nicely in the middle of the available parameter space and was thus chosen for aesthetic reasons. Generally the poorest agreement is found in the furthest bins as the low densities at large radii lend them a greater uncertainty in the range of radii they will cover and the innermost bins barely evolve from their initial conditions.

Using the information from all the bins we can create a plot that shows how any bin of

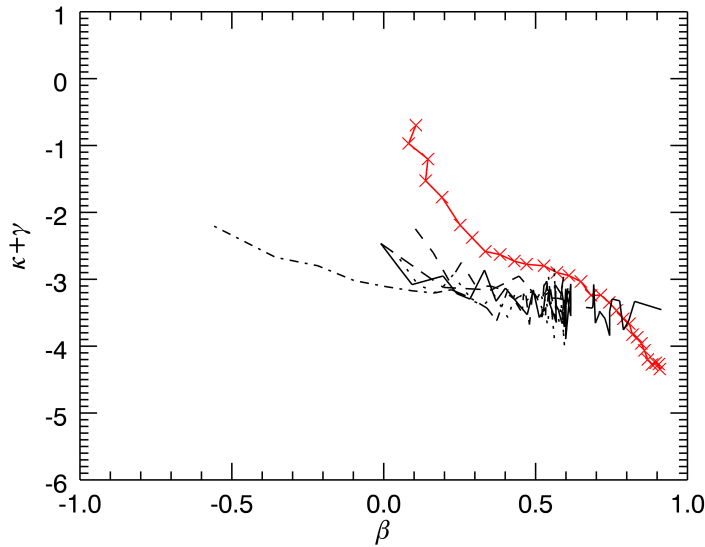


**Figure 6.14:** The position of the 20<sup>th</sup> bin from the 6 Newtonian simulations thus far. Note that all of the bins travel along fairly similar paths as they converge towards the attractor.

material should move if it is perturbed through our parameter space. By combining all the bins and measuring the normalised change in position between kicks we can create a vector at each point that represents how a bin placed at that location will move if perturbed. Dropping a population of test bins into this vector field allows us to measure and plot it.

Fig. 6.15 is the best overall visualisation of the attractor. It neatly summarises the universality of the attractor and provides a predictive framework for the characteristics of partially converged systems. The need for discretised test particles and a lack of systems that tested certain regions of the parameter space creates some blank areas around  $\beta = -0.5, \gamma + \kappa = -5$ . This is an unavoidable compromise between a scarcity of very tangentially anisotropic data points and a very large number of radially anisotropic points.

## 6.5 Summary

Over the course of the last two chapters we have covered a lot of information on this attractor effect. We have found the two primary conditions that the attractor requires to function as well proving that radial infall and radial orbit instability are not the driving mechanisms. Specifically, we demonstrated that energy exchange and phase mixing in a

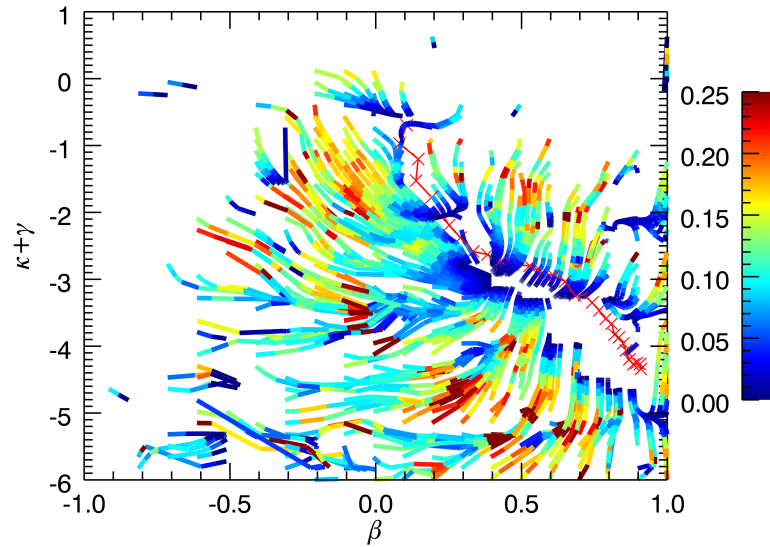


**Figure 6.15:** A representation of the attractor in terms of a vector field. Hotter colours represent larger rates of change of phase-space coordinates between kicks plotted as the total displacement per kick  $\sqrt{\Delta^2\beta + \Delta^2(\kappa + \gamma)}/\Delta t$ .

dynamical potential are necessary conditions for the appearance of the attractor. Since earlier studies have also indicated that those two are sufficient conditions (Sparre & Hansen, 2012a,b), we believe we have established the basic physics underlying the attractor.

As noted in Hansen et al. (2010) it is possible to defy the attractor with specifically biased perturbations. However, since both necessary effects are present during structure formation, in particular through violent relaxation of mergers, we are confident this shows that the attractor is relevant for the fully equilibrated part of cosmological structures. Why the attractor is the exact relation that it is is still an open question as nothing in our results has shown that the attractor solution is special. Indeed, the only special thing about the attractor solution itself is the fact that it appears to be an attractor.

So the story of the attractor ends here for now, as does our look into how to tackle a problem with numerical simulations. In the next, and final chapter, we will bring all our discussions to a close with a final look at how to best communicate our results to the next generations of people who will study them.



# 7

## Epilogue – communication

*“The effort to understand the universe is one of the very few things that lifts human life a little above the level of farce, and gives it some of the grace of tragedy.”*

— *Steven Weinberg*

For this, the final chapter, we will discuss the field of science teaching and communication as it is an area that I have always had a personal interest in. It also feels fitting to end this thesis with a discussion on how best to communicate scientific ideas to others. As this section is based more on personal, subjective experience than previous chapters I feel it is appropriate to use a more informal style than I have been. In fact, informality is exactly what I would like to talk about.

As anyone who has been taught by me will probably attest, I have something of a tendency towards informal ways of describing and explaining concepts. It has been a longstanding concern of mine that this may be in some way harmful, but I could never

reconcile it with my instinct that it was an acceptable, if not preferable, way to convey certain kinds of information. Over the course of this chapter I aim to use tools developed by educational psychology to examine which of these points of view is correct.

For the sake of clarity, I'm going to define my usage of 'formal' against 'informal'. By formal teaching I mean teaching physics as if there is an absolute etiquette describing how this must be done primarily via a preference for technical language over more colloquial terms and by having a reserved, unemotional, often authoritarian demeanor. Informal lecturing would by contrast use more colloquialisms and relate more to familiar words and phrases while coming across as more friendly and relaxed in how the material is delivered.

It is important to stress that this is *not* an argument about mathematical formality or anything associated with the technical content of conveyed information. It is, of course, never recommended to be lax when it comes to mathematics and physical ideas. The point of this chapter is to discuss how best to *package* scientific information so that it is understood and retained by the student. In particular, the biggest problem I have with overly formal teaching methods is the distance I feel it creates between the teacher and the student. In my experience as an undergraduate, the lecturers, even when taking small groups, would project a sense of authority, impersonally hand out facts and figures, and only require that we could say them back correctly.

## 7.1 The power of analogy

Firstly, I am not going to argue that there is any problem with a lecturer projecting a sense of authority *per se* as of course that is important for maintaining basic classroom control. The problems begin when that authority goes beyond a simple awareness of who is teaching who and turns into teaching via argument from authority *i.e.* "The lecturer said something so it must be true because the lecturer said it and for no other reason". Information learnt this way is almost exclusively acquired as surface knowledge and lead to minimal critical analysis performed by the student as they feel unable to question or investigate what has been said. This turns the act of 'doing science' into a mystical art with strange mathematical incantations and arcane rituals with no apparent rhyme or reason besides the fact that doing them 'gets the right answer'.

This issue is well-understood as a problem of how students build their mental models (Redish, 1994) and is known to be exacerbated by factors such as modular curricula (Fry et al., 2009, chapter 9). Of concern to me is that it is also perpetuated by over-formality. One of the best lecturers I ever had was a very personable man. He was chatty, always had a smile, and had plenty of little funny stories to break up the duller sections and maintain audience engagement. He seemed to make an active effort not to stand on ceremony and presented physics as being something very down to earth and practical, even when discussing the more mathematical aspects. Crucially, he did all of this without compromising the integrity of the syllabus he was teaching.

The fact that this style is more engaging is well known (Brown, 1987; Fry et al., 2009, chapter 9) and a happy, interested lecturer with an infectious enthusiasm is clearly a boon to the class, but there seems to be a good reason why that style would also be good for conveying information clearly and effectively. That reason is analogy.

Analogy is a powerful tool and one that is well-motivated for teaching physics (Redish, 1994). According to Vygotsky (1978) the most efficient learning takes place through the addition and modification of prior knowledge in a way that is neither too alien nor too familiar. An appropriately chosen analogy employed to illustrate a point can take a familiar part of the student's everyday experience and force them to re-examine or challenge that experience in such a way that new information can be naturally incorporated.

The connection I find between this and informality is actually quite simple. If a teacher makes the effort to present physics in the most relatable way they can by choosing examples that fit well with the student's prior, informal, everyday life, then the information will be absorbed as something relevant, tangible, and important rather than a list of arbitrary, ritualised facts needed to pass an exam. This is equivalent to the 'personal experience' section of the Kolb cycle of learning that relates knowledge to personal experience. This is much harder to do with a more arm's length and distanced approach that is couched only in technical language that is unfamiliar to the student.

For example, Sobel (2010) is an interesting note. It is a short response to a paper by Art Hobson about how to teach the scientific method. In his letter, Sobel makes much the same point as I am. He argues that teaching something like the scientific method as a series of inscrutable yet compulsory steps can lead to students having no deep understanding of

how or why they are doing things. He concludes that it is much more important to simply teach good practice in a practical and ‘ordinary way’ that people can relate to.

The argument can, of course, be made, that using everyday examples to demonstrate physical processes is not quite the same thing as being informal in teaching them, a point raised by Hobson in response to Sobel’s comments. I would argue that that is not quite the case. Yes, one could choose to teach a course in a very distanced, formalised way and still make reference to everyday examples in passing but I feel that that is missing the point. I prefer to see it the other way around and ask why *should* it be formal in the first place? If all the good analogies and relatable paths to learning come from common experience and we *want* students to understand that then why raise barriers by putting the subject on a pedestal to begin with?

## 7.2 The need for confidence

Part of the desire for formality is related to group size, which is something that I had personal experience of during a previous teaching semester. I was just starting to get to know my group, although some were still rather quiet, and I was struggling to make sure that everyone was getting equal focus time throughout the session. I was subsequently asked, at short notice, to cover someone else’s group during the same time-slot which meant merging the two groups and doubling the amount of students.

The tutorial went fine, the material was dealt with, and the students left apparently content with the lesson but afterwards I noted that I had unconsciously changed how I had been teaching. I had somehow implicitly decided that the group size warranted a greater degree of distancing which meant the tutorial developed too much of a lecture atmosphere for something that is meant to be small and focused.

It seemed like there was some kind of social phase-change that happened once the group size exceeded about ten people and it took some time to realise what it was. It’s a well known effect in both statistics generally and in the field of public speaking specifically that an individual can only personally engage with so many people at once. When faced with a large number of people they stop being individuals and become just ‘100 people’ and you lose the basic engagement. This has passed into popular wisdom in the oft quoted advice of ‘just pick one person at the back and talk to them’ when speaking in public as

doing so provides a social anchor point against the rows and rows of blank faces.

I believe that formality can often, especially in large groups, be a sign of inexperience or of nerves. I say ‘inexperience’ not to be derogatory, but to highlight the simple fact that most HE lecturers do not have any formal teacher training and will mainly be ‘self-taught’ when it comes to how they teach. It takes practice and training to be able to treat a large group like many individuals rather than a formless, potentially judgmental, mass of faces. With the absence of any proper training it is hardly surprising that many lecturers can become rather dispassionate and disconnected.

As for the impact of nerves, I can speak from my own experience. Usually I am easy-going and after I get to know a group I am comfortable poking fun at any errors I make and so on. However, the sudden addition of a few extra people to a group that I was not yet comfortable with had a significant impact on me and, with hindsight, made me rather nervous. I felt that, as a cover teacher, I could not afford to seem like a ‘poor deal’ or like the students were getting an inferior experience compared to their normal teacher. My reflexive response was to become more serious and formal as a form of defense, effectively taking refuge in the social distance this creates and feeling that formality was equivalent to professionalism.

I was not aware I was doing it at the time and, in retrospect, it was rather foolish as I’ve been teaching tutorials for years now, there was no reason for me to suddenly feel insecure. I have also heard plenty of anecdotes from even the most experienced teachers talking about how the idea of standing up in front a lecture hall can be a very nerve-racking experience. Now let me make it perfectly clear that I do not believe that this is the *only* reason that lecturers are formal when teaching. Some feel that it is more professional to maintain distance from the students and I recognise that many lecturers simply choose to present their material a certain way that feels best for them. However, based on my own experiences, I do believe that a lack of training can easily lead to people taking refuge in the idea of being formal when faced with a large group.

In my experience, making an effort to maintain a consistent, relaxed style is worth the effort. When merging groups on subsequent occasions the students seemed a lot happier and the new group seemed to mesh better with the more familiar students. I feel that the effort made to combat depersonalising a class is well worth it though it does take a

certain degree of conscious effort to do. If nothing else, just the act of relaxing can make the experience a more enjoyable for the group.

### **7.3 Informality versus accuracy**

This essay has been rather one-sided as it was prompted largely by my own experiences as both a student and a teacher. I am aware that there are potential problems with being too informal and I am by no means advocating a reduction in standards or the degree of difficulty in the material simply to make it more approachable. As I said at the beginning, the important thing to remember is that however the information is presented it must be presented correctly. It must be made clear that while it is okay to refer to familiar concepts and to have simple ways of explaining an idea, that is a stepping stone towards, not a replacement for, a proper understanding. Again, informality should not become a byword for a lack of effort or professionalism.

I feel justified in my choice of a more informal and relatable style as I have seen plenty to suggest it makes the information easier and more interesting to digest if one is careful. I believe that the literature supports this point of view and more effort should be made to make teachers and lecturers aware of the impact that they can have on a student's understanding of a topic. Ultimately, all the behaviours and ideas that I have covered here are simple and easy to implement.

In a perfect world, HE teachers would have access to a full professional development program that can give them the skills they need to deliver complex material clearly and in a way that will be remembered by the student, however this is perhaps unrealistic. Instead, I believe simply trying a more open, personal approach which treats the subject in a more human way can have a considerable positive impact on the learning process.

Overall I think that, in a way, this is one of the most important areas I have studied. I sincerely hope that I can use what I have learned to become an effective teacher who can get students interested in the nuts and bolts of what science is about. Ultimately, the teaching aspect must be viewed as fundamental to our fields. After all, if you cannot explain and pass on an idea onto the next generation then what good is it to anyone.

## Online resources

- [1] - <http://ads.harvard.edu/>
- [2] - <http://arxiv.org/>
- [3] - <http://http://en.wikibooks.org/wiki/LaTeX/>
- [4] - <http://idlcoyote.com/>
- [5] - <https://developer.nvidia.com/cuda-zone>
- [6] - <http://math.nist.gov/quantum/zoo/>



# Bibliography

- An, J. H., & Evans, N. W. 2006, *ApJ*, 642, 752
- Antonov, V. A. 1973, in *Dynamics of Galaxies and Star Clusters*, ed. T. B. Omarov, 139–143
- Armendariz-Picon, C., Mukhanov, V., & Steinhardt, P. J. 2000, *Phys. Rev. Lett.*, 85, 4438
- Baes, M., & Dejonghe, H. 2002, *Astron. & Astrophys.*, 393, 485
- Banks, T., Dine, M., & Motl, L. 2001, *JHEP*, 2001, 031
- Barber, J. A., & Zhao, H. 2014, *MNRAS* (accepted)
- Barber, J. A., Zhao, H., & Hansen, S. H. 2014, *MNRAS*, 440, 1044
- Barber, J. A., Zhao, H., Wu, X., & Hansen, S. H. 2012, *MNRAS*, 424, 1737
- Barnes, E. I., Lanzel, P. A., & Williams, L. L. R. 2009, *ApJ*, 704, 372
- Barnes, E. I., Williams, L. L. R., Babul, A., & Dalcanton, J. J. 2005, *ApJ*, 634, 775
- Barnes, J., Hut, P., & Goodman, J. 1986, *ApJ*, 300, 112
- Bédorf, J., Gaburov, E., & Portegies Zwart, S. 2012, *J Comp. Phys.*, 231, 2825
- Bédorf, J., & Portegies Zwart, S. 2012, *EU Phys. J. S. T.*, 210, 201
- Begeman, K. G., Broeils, A. H., & Sanders, R. H. 1991, *MNRAS*, 249, 523
- Bekenstein, J., & Magueijo, J. 2006, *Phys. Rev. D*, 73
- Bekenstein, J., & Milgrom, M. 1984, *ApJ*, 286, 7
- Bekenstein, J. D. 2004, *Phys. Rev. D*, 70, 083509
- . 2009, *Nuc. Phys. A*, 827, 555c
- Bellovary, J. M., Dalcanton, J. J., Babul, A., Quinn, T. R., Maas, R. W., Austin, C. G., Williams, L. L. R., & Barnes, E. I. 2008, *ApJ*, 685, 739
- Binney, J., & Tremaine, S. 2008, *Galactic Dynamics*, 2nd edn. (Princeton University Press)
- Bondi, H. 1957, *Rev. Mod. Phys.*, 29, 423
- Brada, R., & Milgrom, M. 1995, *MNRAS*, 276, 453

- Brown, G. 1987, *Phys. Bul.*, 305
- Bruneton, J. P., Liberati, S., Sindoni, L., & Famaey, B. 2009, *JCAP*, 3, 021
- Buyle, P., Hunter, C., & Dejonghe, H. 2007, *MNRAS*, 375, 773
- Cai, Y. F., Saridakis, E. N., Setare, M. R., & Xia, J. Q. 2010, *Phys. Rep.*, 493, 1
- Caldwell, R. R., & Kamionkowski, M. 2009, *An. Rev. Nucl. & Part. Sci.*, 59, 397
- Capozziello, S. 2002, *Int. J. Mod. Phys. D*, 11, 483
- Capozziello, S., Cardone, V. F., & Troisi, A. 2006, *JCAP*, 8, 001
- Capuzzo-Dolcetta, R., Mastrobuono-Battisti, A., & Maschietti, D. 2011, *Arxiv preprint arxiv:1003.3896*, 16, 284
- Carroll, S. M., Duvvuri, V., Trodden, M., & Turner, M. S. 2004, *Phys. Rev. D*, 70, 043528
- Chernin, A. D., Teerikorpi, P., Valtonen, M. J., Dolgachev, V. P., Domozhilova, L. M., & Byrd, G. G. 2009, *A & A*, 507, 1271
- Chiu, M. C., Ko, C. M., Tian, Y., Zhao, H., & Hill, B. 2011, *Phys. Rev. D*, 83, 063523
- Ciotti, L., Londrillo, P., & Nipoti, C. 2006, *ApJ*, 640, 741
- Ciotti, L., & Morganti, L. 2009, *MNRAS*, 393, 179
- . 2010a, *MNRAS*, 401, 1091
- . 2010b, *MNRAS*, 408, 1070
- Ciotti, L., & Morganti, L. 2010c, in *American Institute of Physics Conference Series*, Vol. 1242, *American Institute of Physics Conference Series*, ed. G. Bertin, F. de Luca, G. Lodato, R. Pozzoli, & M. Romé, 300–305
- Ciotti, L., & Pellegrini, S. 1992, *MNRAS*, 255, 561
- Clarke, T. E., Blanton, E. L., & Sarazin, C. L. 2004, *ApJ*, 616, 178
- Clowe, D., Bradač, M., Gonzalez, A. H., Markevitch, M., Randall, S. W., Jones, C., & Zaritsky, D. 2006, *ApJ Letters*, 648, L109
- Copeland, E. J., Sami, M., & Tsujikawa, S. 2006, *Int. J. Mod. Phys. D*, 15, 1753
- Cuddeford, P. 1991, *MNRAS*, 253, 414
- De Bernardis, P., Ade, P. A. R., Bock, J. J., Bond, J. R., Borrill, J., Boscaleri, A., Coble, K., & Fisica, D. 2000, *Nature*, 404, 955
- De Blok, W. J. G., & Bosma, A. 2002, *A & A*, 385, 816
- Dehnen, W. 1993, *MNRAS*, 265, 250

Dehnen, W., & McLaughlin, D. E. 2005, MNRAS, 363, 1057

Dejonghe, H. 1987, MNRAS, 224, 13

Deo, B. B., Jena, P. K., & Maharana, L. 2009, Grav. & Cosmo., 15, 97

DeWitt, B. S. 1967, Phys. Rev., 162, 1195

Diaferio, A., & Ostorero, L. 2009, MNRAS, 393, 215

Dodelson, S., & Liguori, M. 2006, Phys. Rev. Lett., 97, 231

Doremus, J. P., Baumann, G., & Feix, M. R. 1973, A & A, 29, 401

Doremus, J. P., Feix, M. R., & Baumann, G. 1971, Phys. Rev. Lett., 26, 725

Dubinski, J., & Carlberg, R. G. 1991, ApJ, 378, 496

Dutton, A. A., Conroy, C., Van Den Bosch, F. C., Prada, F., & More, S. 2010, MNRAS, 16, 2

Ebisuzaki, T., Ito, T., Makino, J., & Sugimoto, D. 1990, Astron. H., 83, 224

Eddington, A. S. 1916, MNRAS, 76, 572

Efstathiou, G. 1995, MNRAS, 274, L73

Efstathiou, G., Bridle, S. L., Lasenby, A. N., Hobson, M. P., & Ellis, R. S. 1999, MNRAS, 303, L47

Feix, M., Fedeli, C., & Bartelmann, M. 2008, A & A, 480, 313

Flynn, C., Holmberg, J., Portinari, L., Fuchs, B., & Jahreiß, H. 2006, MNRAS, 372, 1149

Fry, H., Ketteridge, S., & Marshall, S. 2009, A Handbook for Teaching and Learning in Higher Education: Enhancing Academic Practice (Taylor & Francis Group)

Gentile, G., Salucci, P., Klein, U., Vergani, D., & Kalberla, P. 2004, MNRAS, 351, 903

Gerhard, O. E. 1991, MNRAS, 250, 812

Gershtein, S. S., Logunov, A. A., & Mestvirishvili, M. A. 2009, Theo. and Math. Phys., 160, 1096

Gillon, D., Cantus, M., Doremus, J. P., & Baumann, G. 1976, A & A, 50, 467

Gnedin, O. Y., Weinberg, D. H., Pizagno, J., Prada, F., & Rix, H. W. 2007, ApJ, 671, 1115

González, J. E., Lacey, C. G., Baugh, C. M., Frenk, C. S., & Benson, A. J. 2009, MNRAS, 397, 1254

Grimm, S. L., & Stadel, J. G. 2014, Arxiv preprint arxiv:1404.2324

Hansen, S. H. 2004, MNRAS, 352, L41

Hansen, S. H., Juncher, D., & Sparre, M. 2010, ApJ, 718, L68

Hansen, S. H., & Moore, B. 2006, *N. Astron.*, 11, 333

Hansen, S. H., Moore, B., Zemp, M., & Stadel, J. 2006, *JCAP*, 14

Hansen, S. H., & Sparre, M. 2012, *ApJ*, 756, 100

Hazewinkel, M. 1994, *Encyclopedia of Mathematics (set)* (Kluwer)

Hénon, M. 1973, *A & A*, 24, 229

Hernquist, L. 1990, *ApJ*, 356, 359

———. 1993, *ApJ Supp.*, 86, 389

Hernquist, L., & Ostriker, J. P. 1992, *ApJ*, 386, 375

Hernquist, L., & Spergel, D. N. 1992, *ApJ Lett.*, 399, L117

Hogan, C. J. 2000, *Rev. Mod. Phys.*, 72, 1149

Horne, K. 2006, *MNRAS*, 369, 1667

Host, O., & Hansen, S. H. 2011, *Arxiv preprint arXiv:0907.1097v2*, 736, 52

Huang, Q. G., & Li, M. 2005, *JCAP*, 2005, 001

Huss, A., Jain, B., & Steinmetz, M. 1999, *ApJ*, 517, 64

Ito, T., Makino, J., Ebisuzaki, T., & Sugimoto, D. 1990, *Comp. Phys. Comm.*, 60, 187

Jaffe, W. 1983, *MNRAS*, 202, 995

Jeans, J. H. 1915, *MNRAS*, 76, 70

Jing, Y. P. 2000, *ApJ*, 535, 30

Kallosh, R., & Linde, A. 2003, *Phys. Rev. D*, 67, 1

Kamionkowski, M. 2007, *Arxiv preprint arXiv:0706.2986*

Kamionkowski, M., Spergel, D. N., & Sugiyama, N. 1994, *Astron. J.*, 426, L57

Kauffmann, G., White, S. D. M., & Guiderdoni, B. 1993, *MNRAS*, 264, 201

Klapdor, H. V., & Grotz, K. 1986, *ApJ Letters*, 301, L39

Komatsu, E. et al. 2009, *ApJ Supp.*, 180, 330

Lane, J. H. 1870, *Amer. J. Sci. Arts*, 50, 57

Lapi, A., & Cavaliere, A. 2011, *ApJ*, 743, 127

Lewis, A. D., Buote, D. A., & Stocke, J. T. 2003, *ApJ*, 586, 135

Lewis, A. D., Stocke, J. T., & Buote, D. A. 2002, *ApJ Letters*, 573, L13

- Lokas, E. L., & Mamon, G. A. 2003, *MNRAS*, 343, 401
- Londrillo, P., & Nipoti, C. 2008, A user guide for N-MODY
- . 2009, *Mem. d. Soc. Astron. Italiana Supp.*, 13, 89
- Lu, H., & Pope, C. N. 2011, *Phys. Rev. Lett.*, 106
- Ludlow, A. D., Navarro, J. F., Springel, V., Vogelsberger, M., Wang, J., White, S. D. M., Jenkins, A., & Frenk, C. S. 2010, *MNRAS*, 406, 137
- Ma, D., & He, P. 2008, *Int. J. Mod. Phys. D*, 17, 1283
- Macmillan, J. D. and Widrow, L. M., & Henriksen, R. N. 2006, *ApJ*, 653, 43
- Makino, J., & Funato, Y. 1993, *Pub. Astron. Soc. J.*, 45, 279
- Makino, N., Sasaki, S., & Suto, Y. 1998, *ApJ*, 497, 555
- Mannheim, P. D. 2006, *Prog. Part. & Nuc. Phys.*, 56, 340
- Mannheim, P. D. 2008, in *Second Crisis in Cosmology Conference*, 0707.2283
- . 2010, *GR & Grav.*, 43, 1
- . 2012, *F. Phys.*, 42, 388
- Mannheim, P. D., & Kazanas, D. 1989, *ApJ*, 342, 635
- Mannheim, P. D., & O'Brien, J. G. 2012, *Phys. Rev. D*, 85, 124020
- Massey, R. et al. 2007, *Nature*, 445, 286
- McGaugh, S. S. 2011, *Phys. Rev. Lett.*, 106, 121303
- McGaugh, S. S., & De Blok, W. J. G. 1998, *ApJ*, 499, 41
- Merritt, D. 1985, *Astron. J.*, 90, 1027
- . 1999, *Pub. Astro. Soci. Pacific*, 111, pp. 129
- Merritt, D., & Aguilar, L. A. 1985, *MNRAS*, 217, 787
- Milgrom, M. 1983, *ApJ*, 270, 365
- . 2009, *Phys. Rev. D*, 80, 123536
- . 2010a, *MNRAS*, 1139, 1129
- . 2010b, *MNRAS*, 403, 886
- Molendi, S. 1999, *Arxiv preprint astro-ph/9910284*, 2
- Moore, B., Quinn, T., Governato, F., Stadel, J., & Lake, G. 1999, *Arxiv preprint astro-ph/9903164*, 310, 1147

Navarro, J. F., Frenk, C. S., & White, S. D. M. 1996, *ApJ*, 255

Osipkov, L. P. 1979, *Pis'ma Astr. Zh.*, 5, 77

Ostriker, J. P., Peebles, P. J. E., & Yahil, A. 1974, *ApJ*, 193, L1

Parker, L. C., Hoekstra, H., Hudson, M. J., van Waerbeke, L., & Mellier, Y. 2007, *ApJ*, 669, 21

Peebles, P. J., & Ratra, B. 2003, *Rev. Mod. Phys.*, 75, 559

Perlmutter, S. et al. 1998, *ApJ*, 517, 21

Perlmutter, S., Turner, M. S., & White, M. 1999, *Phys. Rev. Lett.*, 83, 670

Plummer, H. C. 1911, *MNRAS*, 71, 460

Polyachenko, E. V., Polyachenko, V. L., & Shukhman, I. G. 2013, *MNRAS*, 434, 3208

Redish, E. F. 1994, *Am. J. Phys.*, 62, 796

Riess, A. G. et al. 1998, *Astron. J.*, 116, 1009

Robert, D., & Smilga, A. V. 2008, *J. Math. Phys.*, 49, 042

Romero, J. 2006, *Phys. Rev. D*

Roos, M. 2010, Arxiv preprint arXiv:1001.0316v2

Salucci, P., Lapi, A., Tonini, C., Gentile, G., Yegorova, I., & Klein, U. 2007, *MNRAS*, 378, 41

Sanders, R. H., & McGaugh, S. S. 2002, *An. Rev. A & A*, 40, 263

Sarazin, C. L., Wise, M. W., & Markevitch, M. L. 1998, *ApJ*, 498, 606

Sarkar, S. 2008, *GR & Grav.*, 40, 269

Sato, C. 1980, *Pub. Astron. Soc. J.*, 32, 41

Schwarzschild, M. 1979, *ApJ*, 232, 236

Scoville, N. et al. 2007, *ApJ Supp.*, 172, 150

Shaw, D. J., & Barrow, J. D. 2011, *Phys. Rev. D*, 83, 043518

Shor, P. W. 1995, Arxiv preprint arXiv:quant-ph/9508027

Sobel, M. 2010, *Phys. Teach.*, 48, L1

Sotiriou, T. P., & Faraoni, V. 2010, *Rev. Mod. Phys.*, 82, 451

Sparre, M., & Hansen, S. H. 2012a, *JCAP*, 7, 42

———. 2012b, *JCAP*, 10, 49

- Spekkens, K., Minchin, R., & Momjian, E. 2008, in AIP Conference Proceedings, Vol. 1035 (AIP), 47
- Spergel, D. N., & Steinhardt, P. J. 2000, Phys. Rev. Lett., 84, 3760
- Springel, V. 2005, MNRAS, 364, 1105
- Steinmetz, M. 1996, MNRAS, 278, 1005
- Syer, D., & White, S. D. M. 1998, MNRAS, 293, 337
- Taylor, J. E., & Navarro, J. F. 2001, ApJ, 563, 483
- Van Hese, E., Baes, M., & Dejonghe, H. 2011, ApJ, 726, 80
- Vygotsky, L. 1978, *Mind in Society: The Development of Higher Psychological Processes* (Cambridge, MA: Harvard University Press)
- Wang, B., Liu, H., & Xu, L. 2004, Mod. Phys. Lett. A, 19, 449
- Wang, W. F., & Yang, S. Z. 2008, Phys. Lett. B, 668, 79
- Weinberg, S. 1987, Phys. Rev. Lett., 59, 2607
- . 1989, Rev. Mod. Phys., 61, 1
- Wu, X., Zhao, H., Wang, Y., Llinares, C., & Knebe, A. 2009, MNRAS, 396, 109
- Yang, R., Chen, B., Zhao, H., Li, J., & Liu, Y. 2013, Phys. Lett. B, 727, 43
- Zehavi, I., & Dekel, A. 1999, Nature, 401, 252
- Zhao, H. 1996, MNRAS, 278, 488
- . 2005, Astron. & Astrophys., 444, L25
- Zlosnik, T. G., Ferreira, P. G., & Starkman, G. D. 2007, Phys. Rev. D, 75, 044017
- Zwicky, F. 1933, Helvetica Phys. Acta, 6, 110